Light Scattering in the Clouds on Jupiter

Thesis by

Ulyana Anatolyevna Dyudina

In Partial Fulfillment of the Requirements

for the Degree of

Doctor of Philosophy

California Institute of Technology

Pasadena, California

2002

(Submitted December 27, 2001)

Disclaimer

"-Elle est bien belle, votre planète. Est-ce qu'il y a des océans?

-Je ne puis pas le savoir, dit le géographe.

-Ah! (Le petit prince était déçu.) Et des montagnes?

-Je ne puis pas le savoir, dit le géographe.

-Et des villes et des fleuves et des déserts?

-Je ne puis pas le savoir non plus, dit le géographe.

-Mais vous êtes géographe!

-C'est exact, dit le géographe, mais je ne suis pas explorateur. Je manque absolument d'explorateurs. Ce n'est pas le géographe qui va faire le compte des villes, des fleuves, des montagnes, des mers et des océans. La géographe est trop important pour flâner. Il ne quitte pas son bureau." [1]

"Le Petit Prince," Antoine de Saint-Exupéry

---

[1] "Your planet is very beautiful," he said. "Has it any oceans?"
"I couldn't tell you," said the geographer.
"Ah!" The little prince was disappointed. "Has it any mountains?"
"I couldn't tell you," said the geographer.
"And towns, and rivers, and deserts?"
"I couldn't tell you that, either."
"But you are a geographer!"
"Exactly," the geographer said. "But I am not an explorer. I haven't a single explorer on my planet. It is not the geographer who goes out to count the towns, the rivers, the mountains, the seas, the oceans, and the deserts. The geographer is much too important to go loafing about. He does not leave his desk."

"The Little Prince," Antoine de Saint-Exupery

Acknowledgements

Because the first (and hopefully not the only) readers of these words are among the people to whom I owe most of my thanks, I will start with them, my thesis committee.

I thank my advisor, Andy Ingersoll, for teaching me to be in love with science. His enthusiasm fires up every soul around. That enthusiasm was an incredible help for me because that was a skill missing in the Soviet scientific school, in which the ability to doubt and criticize was respected almost as if it was the most important quality of a real scientist. Not trying to diminish the importance of the doubt, I claim that this is not all needed for science. There should also be some passion, imagination, an ability to be challenged by the scientific problem, fight with it, win and forgive it afterwards. That was the lesson of the live science, for which I thank Andy the most. Of course, there were numerous amazing teaching, writing, and communication skills, and lots and lots of knowledge, which I really hope I picked up at least to some extent, and I am very thankful for that too.

I want to thank Peter Goldreich for showing me the beauty of the science. His Introduction to the Planetary Science course was the best course I've ever taken. It reminded me of the nights in high school when we students were sitting together solving tricky math problems supposedly because it was useful for the incoming university exams, but actually because solving them was fun. I haven't seen this spirit for years and saw it again in this class. I want to thank Peter for his concern about me. I really appreciate that he offered me the rehearsal of my (already failed once) Oral Exam in front of him. I wouldn't ever dare to ask for that myself. Amazingly enough he managed to make me think that I am going to be OK. And of course, I want to thank Peter for being the person knowing everything in the world, well, at

least to the first order.

I want to express my deepest thanks to Yuk Yung, who is a really nice person and always cares about everyone. I probably also owe some apologies to him because I was not talking to him enough. (Although it is me and not him suffering from that, I do feel a little guilty.)

I want to thank Mike Brown for his involvement and support of me, the first student with whom he worked after turning into a professor. Thanks for teaching me IDL. Thanks for explaining every thinkable detail of any question. Thanks for doing your best in dragging me through my Orals. Thanks for protecting your students, even in the unsteady position of a young professor.

Well, now I can get into more chronological order.

I want to thank "interesting times." One piece of Chinese wisdom claims: "God save you from living through interesting times." Apparently Russia is getting these "interesting times" quite frequently. Governments change, revolution replaces revolution. Strangely enough, that was the main reason why I got a good education and am finally graduating from the top university in the field. First, the revolution of 1917 forced (quite brutally, by starvation) my grandparents, most of whom were born in poor peasant families in illiterate countrysides, to the cities. They searched for a job and, therefore, education. Then by settling in the city, they, together with socialism (meaning free education for everyone), provided university-level education for my parents. I followed their path largely by inertia. Then another "interesting" period came that made me apply to American universities, because that was the only chance for me to stay in science. I must say that there are plenty of reasons to remove the quotes from "interesting times": these times are truly interesting. During both revolutions democracy, art, and the overwhelming feeling of freedom were blooming side-by-side with poverty, dirt, and violence.

Now, I am getting to the people dear to my heart, who helped me the most and

made it possible for me to survive such a huge change in leaving my Motherland. These are my parents Lilia Shagockaya and Anatoly Dyudin, and my son Anton. Anton provided motivation. Being a good mother implies being a good example for the child. Without thinking of that, I would not have taken the challenge of moving to a foreign country, to a place where I did not know anyone. My parents were babysitting virtually all the time I stayed at Caltech either by coming to the States or by taking Anton to Russia for summers. I would not have been able to survive grad school without their help.

I thank Anton Leouski, my classmate in Moscow University, who moved to study in the U.S. before me. He made me believe that such an unthinkable plan as trying to get into American universities may actually be real. I thank him for all the help and advice on how to submit the application papers correctly, how to write the statement of purpose, and how to deal with all these huge differences between Russian and American communication styles.

I thank Ilia Binder for helping me survive my first months in the U.S., starting with teaching me to drive and ending with the explanations of math.

I thank Andrei Khodakovski, in whom I could always find a supportive and tolerant friend, and from whom I learned lots of things in mathematics and programming.

I thank those who helped me with my first project, the PCA study of jovian clouds. I thank R.A. West for his help with radiative transfer modeling and advice; Peter Gierasch, Don Banfield, and M.J.S. Belton for fruitful discussions.

In the lightning study, I used the Galileo images processed and explained to me by Ashwin Vasavada and Shawn Ewald. Thanks for that. Dennis Boccippio helped me a great deal with terrestrial lightning data. LIS data were provided by the Global Hydrology Resource Center (GHRC) at the Global Hydrology and Climate Center, Huntsville, Alabama.

I thank Patrick Irwin for being enthusiastic about the method I developed in my

PCA paper and the result of this enthusiasm – our collaborative paper (Irwin and Dyudina, 2001), which is a very logical and fruitful application of the method.

I really appreciate those who had the patience to correct some scientific, numerous stylistic and (to my total shame) lots of grammatic errors in my drafts. Thanks to Adam Showman, Ashwin Vasavada, Sarah Stewart, Frank Mills, James Cho, Jackie Kessler, Maarten Roos-Serote and Nora Oshima.

I thank Kay Campbell, Irma Black and all the other Planetary Science secretaries who were very friendly and helpful in solving the official issues at Caltech.

Special thanks to Mike Black for saving me from numerous computer-related troubles, up to printing my poster after I had to leave for the AGU–2000 conference without the poster.

There were many other people who gave me their help exactly when I needed it. I thank Anton and Olga Ivanov, Max Ljutikov, Galka Lokshina and Andy Greenberg, Mitya and Olga Kossakovski, Oleg and Lilia Bondarenko, Tanya Mjagkova, Olga Kolomenski, Derrick Bass with the rest of the Caltech Ballroom team, Margaret Belska, and many other wonderful people whom I met at Caltech.

Abstract

We construct maps of jovian cloud properties from images taken simultaneously by the Galileo solid state imaging system (SSI) and the near-infrared mapping spectrometer (NIMS) at 26 visible and near infrared wavelengths, ranging from 0.41 to 5.2 μm. Three regions — the Great Red Spot (GRS), a 5-micron Hot Spot, and one of the White Ovals — are studied. We perform a principal component analysis (PCA) on the multispectral images. PCA shows that the pixel-to-pixel variations at the different wavelengths are highly correlated, and that 91% of the variance in the data can be summarized using only three maps. The three maps are combined into one color map, which indicates different 26-wavelength spectra as different colors. Using the representative spectra for each color we compare different areas on the map qualitatively. We find that in the GRS there is a red chromophore which is associated with clouds that block 5-μm emission. At the hot spot and white oval regions there is no chromophore associated with clouds. Most of the bright, optically thick clouds blocking thermal emission are also extended vertically to the upper troposphere. Some of the bright, optically thick clouds blocking thermal emission are deep and do not extend vertically to the upper troposphere. A small convective stormlike cloud to the northwest of the GRS is unusually reflective at long wavelengths (4μm) and might indicate large particles.

We study lightning on Jupiter and the clouds illuminated by the lightning. The Galileo SSI lightning images have a resolution of 25 km/pixel and are able to resolve the diffuse spots of light scattered in the clouds, which have full widths at half maximum in the range 90-160 km. We compare the lightning images with the images produced by our 3D Monte Carlo light scattering model. The model reproduces non-

isotropic non-conservative scattering of the photons in the non-homogeneous opacity distribution. We derive that some of the observed scattering patterns are produced in a 3D cloud rather than in a plane-parallel cloud layer, suggesting deep convection. For the six flashes studied, the clouds above the lightning are optically thick ($\tau > 5$). Lightning is as deep as the bottom of the water cloud. Jovian flashes are more regular and circular than the largest terrestrial flashes observed from space.

Contents

Acknowledgements iv

Abstract viii

1 Introduction 1

2 Interpretation of NIMS and SSI Images on the Jovian Cloud Structure 7

2.1 Introduction 8

2.2 The Data 10

2.3 Data Analysis 15

2.3.1 Application of PCA on the Image Data 15

2.3.2 Limitations of the Method 18

2.4 Results 19

2.4.1 PCA Results 19

2.4.2 PCA for the Different Regions 28

2.4.3 Reconstruction of the NIMS Images Using SSI Maps 28

2.5 Error Analysis 31

2.5.1 Spatial Resolution Effects 31

2.5.2 Observational Noise Effect 33

2.5.3 Noise-Based Normalization 35

2.5.4 Wavelength Uncertainty 37

2.6 Discussion 37

3 Monte Carlo Radiative Transfer Modeling of Lightning Observed in Galileo Images of Jupiter **39**

3.1 Introduction 40

3.2 The Data 41

3.3 Model 48

3.4 Results 50

3.4.1 3D Clouds 50

3.4.2 Lightning Depth 54

3.4.3 Optical Depth of the Clouds 63

3.4.4 Energy of the Lightning 65

3.5 Comparison with Terrestrial Lightning 68

3.6 Discussion 70

A Appendix: Monte Carlo Light Scattering Model **74**

A.1 Scattering 74

A.2 Image Construction 79

A.3 Computer Implementation 83

A.3.1 Algorithm 83

A.3.2 Performance 84

A.4 Advantages and Disadvantages of Monte Carlo Approach 87

A.5 Tests 88

List of Figures

2.1 Combined SSI–NIMS image set for the GRS 12
2.2 Combined SSI–NIMS image set for the hot spot 13
2.3 Combined SSI–NIMS image set for the white oval. 14
2.4 The mean spectra for the GRS, Hot Spot, and White Oval regions . . 16
2.5 Color map of the GRS and the spectra for the representative colors . 20
2.6 First four PCs for the GRS, Hot Spot, and White Oval regions 22
2.7 Maps of the first principal component for the three regions 23
2.8 Maps of the second principal component for the three regions 25
2.9 Comparison of 26-wavelength and 4-wavelength (SSI only) Principal Components 30
2.10 Reconstruction of the 26-wavelength data set using four SSI images . 32
2.11 Signal-to-noise ratio for the GRS 34
2.12 Comparison of principal components produced with different normalizations 36

3.1 Flash 1 unprojected data numbers 44
3.2 The image and brightness falloff plot for Flash 1 46
3.3 The images and brightness falloff plots for flashes 2, 3, 4, 5, and 6 . . 47
3.4 Model results for the plane-parallel cloud compared to Flash 1 data . 51
3.5 Model results for the hemispheric cloud compared to Flash 1 data . . 53
3.6 Model results for the plane-parallel cloud compared to Flash 5 data . 55
3.7 Ratio of cloud layer depth to HWHM of the lightning spot for different cloud models 56

3.8 Henyey-Greenstein functions used in the model 58
3.9 Increase in the apparent HWHM of the lightning spot due to pixel size. 61
3.10 Pressures corresponding to the depth below the cloud tops 64
3.11 Cloud transmission for different models 67
3.12 Terrestrial flashes observed from space 69

A.1 Geometry of the cloud. 75
A.2 Photon scattering geometry 77
A.3 Solid angle beams for different screens 79
A.4 Projection of the photon onto the screen 80
A.5 Error due to the beam size 81
A.6 Scheme of accumulation of the photons into pixels 82
A.7 Scheme of the program. 83
A.8 Sample 100×100 image 85
A.9 Pixel values for the row of pixels across the brightest part of the image in Fig. A.8. 86
A.10 Comparison of our results with Fig. 22 of Chandrasekhar (1960) . . . 89

List of Tables

2.1 Data characteristics 11

2.2 Percentages of variance associated with the principal components in the case of standard and noise-based normalization 35

3.1 Characteristics of the flashes 42

3.2 The depth of the lightning below the cloud tops for different flashes . 62

Chapter 1 Introduction

This work is focused on two subjects: structure of the tropospheric clouds on Jupiter and lightning that happens in some of these clouds. Both subjects are the keys to understanding atmospheric dynamics on Jupiter. Jovian troposphere (from 0.2 to about 20 bar) is an extremely dynamically active layer because most of the sunlight is absorbed within it and most of the heat is radiated from the top of it. The energy flux from the jovian interior is nearly as strong as the incident solar flux (Ingersoll et al., 1976). The energy from both solar and internal fluxes must be delivered to the upper layers convectively, which results in updrafts and clouds at some locations and dry downdrafts at the others. By using location and elevation of the clouds, one can derive the atmospheric motion.

Previously, several approaches were used to derive the cloud distribution.

First, the cloud locations were predicted theoretically based on equilibrium condensation assumption, *i. e.*, that the clouds are condensing from the vapor above the level where the corresponding volatile reaches the dew point (Lewis, 1969a,b; Weidenschilling and Lewis, 1973). Assuming adiabatic atmosphere the cloud bases are determined by the abundances of the volatiles in the deep atmosphere. For the solar abundances three cloud layers are expected to form. NH_3 ice cloud would have the base at 0.7 bars (146 K). NH_4SH cloud would have the base at 2.2 bars (210 K). The water cloud, of which the top part is ice (down to 5.4 bars (273 K)) and the bottom part is an aqueous ammonia solution, would have the base at 5.7 bars (277 K). Lower abundances give lower pressures and vice versa. Although this assumption excludes photochemically-produced clouds, it gives a good first approximation of where to expect the clouds to form if the observations are not sufficient to retrieve the opacity

directly.

Later, more data became available from both groundbased observations and spacecraft (Pioneers 10 and 11 (1973), Voyagers 1 and 2 (1979), Galileo (1995–present), and Cassini (2000–2001)). The new data stimulated development of new techniques to retrieve cloud locations. A comprehensive review of the pre-Galileo research is given by West et al. (1986).

The clouds in the jovian troposphere are directly observable in visible and infrared light. Because of that, one of the most popular techniques is to use visible or near infrared spectra and/or images to solve the inverse radiative transfer problem, *i. e.*, to find the vertical distribution of the clouds consistent with the observations. These studies treated the clouds as plane-parallel layers that vary on large horizontal scales.

One of the most commonly referenced works on this subject is the radiative transfer retrieval by Tomasko et al. (1978). The authors used limb darkening in Pioneer 10 visible images of Jupiter to derive vertical cloud distribution and the scattering phase function of the cloud particles. Until Galileo Probe Nephelometer measurement (Ragent et al., 1998; Sromovsky and Fry, 2001), that was the best retrieval of the scattering phase function of the cloud particles, and was used in many of the subsequent models.

A number of radiative transfer retrievals were done after the review by West et al. (1986), and these studies are to be summarized in the new "Jupiter" book (Bagenal, 2001). The elevations of the clouds below the tropopause (0.26 bars) in these studies remain controversial even for the main cloud deck, and to the larger extent for the deeper (supposedly water) clouds.

Carlson et al. (1994) used a radiative transfer model to simultaneously derive a NH_3 mixing ratio and the cloud distribution from the Voyager IRIS spectra. The clouds' location is restricted mainly by using the equilibrium condensation assumption by Weidenschilling and Lewis (1973) and is based on the mixing ratios derived in the

model. Their results suggest that NH_3 is depleted above 1 bar level and may reach the saturation only at 0.5 bars. By modeling spectral slopes from 5 to 55 μm, they derived that the NH_3 clouds are composed primarily from large particles (sizes of order 100 μm). Highly variable NH_4SH cloud is found at 1.9 bars. Water was found to be undersaturated above 4 bars with a relative humidity of 30%. A cloud (presumably water) of optical depth of 5-15 is found at about 5 bars.

Banfield et al. (1998) used a radiative transfer model to solve for cloud location and opacity using Galileo SSI images in three wavelengths and three viewing geometries for three features (the GRS, a hot spot, and white ovals) that were tracked in the sequence of the images. The location of the spatially-variable cloud was also constrained by looking at small-scale brightness contrast at different wavelengths. Banfield et al. (1998) derived the optically thick (optical depth 3-20) laterally variable clouds above $\sim$ 0.7 bar and no lower clouds, at least in the areas where the lower clouds can be seen behind the $\sim$ 0.7 bar cloud. The one exception is the $\sim$ 4-bar deep cloud near the (presumably convective) small scale optically thick cloud northeast from the GRS. The clouds similar to this one are likely playing an important role in the jovian meteorology as will be discussed later.

Another radiative transfer retrieval by Irwin et al. (1998) is based on about 300-wavelength spectra from Galileo near infrared mapping spectrometer (NIMS) in 0.8–5 microns. Contrary to the conclusions of Banfield et al. (1998), the main variable cloud is found at 1–2 bar level (Irwin et al., 2001; Irwin and Dyudina, 2001).

The only *in situ* cloud measurements from the Galileo probe detected a thin cloud at $\sim$ 1.2 bars and a thin cloud above 0.5 bars (Ragent et al., 1998). This characterizes the dry environment of the probe entry site — a Hot Spot region. Sromovsky and Fry (2001) use another radiative transfer model based on Hubble Space Telescope (HST) visible images. The results show that the HST data can be reproduced by the model which has the clouds of variable opacity at 1.2 bars and above 0.5 bars — at

the elevations where the probe found them.

An alternative to the full radiative transfer retrieval from high resolution Galileo SSI data is a qualitative comparison of the different regions. It is rather hard to derive the exact location of the clouds with only four SSI wavelengths and relatively poor sampling of observational geometries. However, the relative location of the clouds in different regions can be seen rather easily because the SSI wavelengths are chosen such that different filters probe different levels in the atmosphere. The qualitative approach was used by Vasavada et al. (1998), where the Galileo SSI images in three wavelength were combined as different color channels. The resulting image shows different cloud heights as different colors. A more sophisticated method (PCA) for qualitative analysis is proposed in this work. Here the 26-wavelength spectra are analyzed and combined into a three-component color image, where each color corresponds to a specific spectrum. This allows more detailed qualitative comparison of the different regions. In addition, the way PCA is applied to the spatial/spectral data is beneficial when combined with the radiative transfer retrievals (see Irwin and Dyudina (2001)) because PCA filters out noise and reduces computations. This work demonstrates the capabilities of PCA in terms of noise reduction and data compression.

Another approach to the problem of cloud formation is modeling the atmospheric dynamics. Ingersoll (1976) gave a pre-Voyager view of the dynamics of the jovian atmosphere. The main implication in terms of clouds is that clouds indicate upwelling and cloudless areas — downwelling. Accordingly, the bright cloudy longitudinal bands on Jupiter (zones) are upwelling and the dark cloudless bands (belts) are downwelling. However, lightning, a clear indicator of updraft, was detected almost exclusively in the belts (Little et al., 1999). This lead Ingersoll et al. (2000) to propose that the air in the belts is rising at the cloud base level, but is descending at the cloud top level with the extra air mass being removed from belts to zones laterally in the middle

troposphere. Compared to this globally-averaged mass balance, the local meteorology of the belts is very diverse as can be traced by small scale fast moving clouds in the jovian images and movies (Vasavada et al., 1998; Gierasch et al., 2000; Porco and the Cassini ISS team, 2001).

Del Genio and McGrattan (1990) modeled moist convection on Jupiter using modified terrestrial global circulation model. They concluded that very different regimes of convection may occur in different locations. Clouds may develop at different elevations and not only at equilibrium condensation level.

Lightning flashes on Jupiter are associated with small (supposedly cumulus) bright clouds (Borucki and Magalhães, 1992; Little et al., 1999; Gierasch et al., 2000; Porco and the Cassini ISS team, 2001). To produce lightning, the convection must be strong. The energy of lightning suggests that these small bright clouds (storm clouds) may be capable of carrying most of the upward energy flux through the troposphere (Gierasch et al., 2000; Ingersoll et al., 2000).

Storm clouds attracted special attention of the modelers. Different radiative transfer models suggest that they penetrate from the water cloud bases all the way to the tropopause (Banfield et al., 1998; Irwin and Dyudina, 2001). Hueso and Sánches-Lavega (2001) modeled local dynamics in the storm clouds and confirmed such vertical extensions, also predicting fast 60 m/s updrafts. Such high updraft speeds are favorable for lightning.

This work shows a new approach in studying storm clouds with the help of lightning. We use the patterns of light scattered in the clouds from Galileo images and derive the vertical extent of the clouds and the 3D cloud shape. This is done by modeling 3D light scattering by a Monte Carlo simulation. We find that the clouds are unexpectedly high, up to 95 km. This corresponds to the cloud extending from below the expected water cloud base to above the tropopause. That is an argument for even stronger convection than was predicted in the models and therefore for larger

contribution of the storm clouds into the global energy balance on Jupiter.

Chapter 2 contains the PCA study of jovian clouds as published in Dyudina et al. (2001). Chapter 3 outlines the study of lightning as it is submitted to Icarus (Dyudina and Ingersoll, 2001). The Appendix describes the main details of the radiative transfer model used in the lightning study.

Chapter 2 Interpretation of NIMS and SSI Images on the Jovian Cloud Structure

We present maps of jovian cloud properties derived from images taken simultaneously by the Galileo solid state imaging system (SSI) and the near-infrared mapping spectrometer (NIMS) at 26 visible and near-infrared wavelengths, ranging from 0.41 to 5.2 μm. Three regions — the Great Red Spot (GRS), a 5-micron Hot Spot, and one of the White Ovals — were studied. We perform a principal component analysis (PCA) on the multispectral images. The principal components (PCs), also known as empirical orthogonal functions, depend only on wavelength. The first PC is that spectral function which, when multiplied by an optimally chosen number (amplitude factor) at each pixel location and subtracted from the spectrum there, minimizes the variance for the image as a whole. Succeeding PCs minimize the residual variance after the earlier PCs have been subtracted off. We find that the pixel-to-pixel variations at the different wavelengths are highly correlated, such that the first three PCs explain 91% of the variance in the spectra. Further, one can estimate the amplitudes of the first two PCs using only the four SSI wavelengths and still explain 62% of the variance of the entire spectrum. This can be an advantage when trying to classify features that are resolved in the SSI images but not in the NIMS images. The first PC in all three regions shows negative correlation between 5 μm emission and reflected solar light in both atmospheric windows and the methane and ammonia absorption bands. Thus most of the bright, optically thick clouds blocking thermal emission are also extended vertically to the upper troposphere. The first PC at the GRS shows a negative correlation between the violet and all other bands except 5 μm, for which the

correlation is positive. Thus in the GRS there is a red chromophore (absorbing in the violet, reflecting at longer wavelengths) which is associated with clouds that block 5-μm emission. There is no such correlation at the hot spot and white oval regions and therefore no chromophore associated with clouds. The second PC shows a positive correlation between the depth of the methane and ammonia absorption bands and brightness at other visible and near-IR wavelengths; there is also a negative correlation between these quantities and 5-μm emission. Thus some of the bright, optically thick clouds blocking thermal emission are deep and do not extend vertically to the upper troposphere. A color image composed using the first three PCs shows areas of unusual spectra, which appear in distinct colors. An example is the small convective stormlike cloud to the northwest of the GRS. This cloud is highly reflective at long wavelengths (4μm) and might indicate unusually large particles.

2.1 Introduction

One of the principal goals of the Galileo mission to Jupiter is to determine how the clouds are distributed in the jovian atmosphere. Knowledge of the cloud distribution is crucial for understanding atmospheric composition and motion and other processes on Jupiter. Studying clouds is especially important as they are the primary source of information about the dynamics of the jovian atmosphere. The pre-Galileo view of the clouds was based on ground-based spectral studies, polarization properties of the atmosphere (detected by the Pioneer spacecrafts), Voyager visible imaging, the Voyager infrared IRIS experiment and other remote sensing techniques. A detailed review of these studies and the cloud structure derived from these observations can be found in West et al. (1986); see also Sada et al. (1996), Satoh and Kawabata (1994), and Beebe (1997). The Galileo mission brings new constraints to the cloud models. Both Galileo probe *in situ* data (Niemann et al., 1996) and Galileo orbiter

observations (Carlson et al., 1996; Belton et al., 1996) have fueled recent development of new cloud and dynamical models (Banfield et al., 1998; Weir et al., 1997; Baines et al., 1999; Orton et al., 1998; Irwin et al., 1998).

We use Galileo solid state imaging (SSI) (Vasavada et al., 1998) and near-infrared mapping spectrometer (NIMS) data (Weir et al., 1997; Baines et al., 1999) to derive and map properties of the observed clouds at the spatial resolution of the NIMS instrument (190–380 km). We study the regions of the Great Red Spot (GRS), the region to the south of one of the Hot Spots, and one of the White Ovals. To separate and map the strongest variation in the spectra, we perform principal component analysis (PCA) on the image data. Using PCA we summarize 91% of the brightness variance from 26 spatial maps of the GRS (one map per each wavelength) into one false color map. We make a qualitative comparison and interpretation of the spectra representing parts of the GRS using this map. We show that a reconstruction of the images at NIMS wavelengths can be done using SSI images and PCA results.

This study is important because it is the first to combine high spatial resolution (22–36 km/pixel of SSI and 190–380 km/pixel of NIMS) with broad spectral coverage (26 wavelengths from 0.41 to 5.2 μm). As a result, high-resolution cloud structure is derived. The use of PCA allows us to separate parts of the regions having different spectra, reduce the noise, and separate spatial and spectral variation in the data.

We offer qualitative interpretations only. Quantitative interpretations are beyond the scope of this paper. We did some preliminary experiments using a radiative transfer model by R. West (private communications). Although the model results are in rough agreement with our qualitative interpretation, some of the parameter dependences in the model are nonlinear. PCA is a linear least squares analysis. Therefore, it is not possible to find an exact quantitative fit to the linear PCA results. An additional modeling complication is that before modeling spatial variations in the spectra, one needs to model the averaged spectrum. That is best done with a more

complete spectrum, i.e., more wavelengths. Such data do exist, particularly for NIMS (Irwin et al., 1998), but these data have limited spatial coverage. The three regions considered here are the only regions where we have SSI and NIMS data with good spatial coverage. Accordingly, instead of modeling, we concentrate here on the spatial correlations and qualitative comparison of the areas on Jupiter that are well resolved spatially.

The structure of this paper is as follows. In Section 2.2 we describe the observational data. Section 2.3 describes principal component analysis. Section 2.4 contains PCA results and interpretation of them in terms of cloud structure. We analyze errors in Section 2.5. Section 2.6 contains the discussion of our results in terms of atmospheric motion.

2.2 The Data

Two instruments on the Galileo orbiter observed the Great Red Spot, the Hot Spot, and the White Oval, as well as their surroundings, in 1996–1997 on orbits G1, E4, and E6 respectively. The near infrared mapping spectrometer mapped the areas in near-IR wavelengths ranging from 0.733 μm to 5.203 μm. Simultaneously with NIMS, the solid state imager mapped the two regions at four wavelengths (0.410, 0.727, 0.756, and 0.889 μm). For the GRS the time difference between NIMS and SSI images was approximately 15 minutes (see Table 2.1). During this short time the observed clouds did not move more than one NIMS pixel. For the Hot Spot and the White Oval, the time differences were 20 and 12 hours respectively. Individual clouds could have moved by at most 1–2 NIMS pixels; therefore, most features on NIMS and SSI images remain similar. We combined NIMS and SSI data for each region. Then we studied how the combined 26-wavelength spectrum changed from pixel to pixel. One NIMS wavelength (2.435 μm) from the GRS data set was not considered because the image

		Number of wavelengths	Spatial resolution (km/pixel)	NIMS-SSI time separation
GRS	NIMS	23	380-420	15 minutes
	SSI	4	30-36	
Hot Spot	NIMS	25	$\approx$190	20 hours
	SSI	4	23-29	
White Oval	NIMS	25	$\approx$230	12 hours
	SSI	4	22-28	

Table 2.1: Data characteristics

shows no significant signal, and therefore it is of potential interest as an indicator of strong atmospheric absorption but is useless for our brightness distribution analysis. The Hot Spot and White Oval images were analyzed at 26 wavelengths corresponding to the GRS wavelengths, such that the PCA results can be compared for the three data sets. The images of the GRS are shown in Fig. 2.1. Part of the Hot Spot image (Fig. 2.2) at NIMS wavelengths was shadowed by satellite Europa. This area was removed from our data analysis.

Different scattering geometries of NIMS and SSI are important for the Hot Spot and White Oval data (Figs. 2.2 and 2.3). For the Hot Spot the phase angle is 16^o for NIMS and 56^o for SSI. For the White Oval the phase angle is 20^o for NIMS and 48^o for SSI. The White Oval images were taken close to the terminator (with an incident angle of about 60^o for both SSI and NIMS). As a result, at the White Oval, high atmospheric haze obscured the lower clouds in the wavelengths of high gaseous absorption and there is no significant brightness variation in some of the NIMS images (see Fig. 2.3). Because of that effect and because of the cloud motion due to the NIMS – SSI time separation, the results for the Hot Spot and the White Oval are more uncertain than those for the GRS. However, taking into account the uniqueness of these simultaneous observations, the Hot Spot and White Oval data are

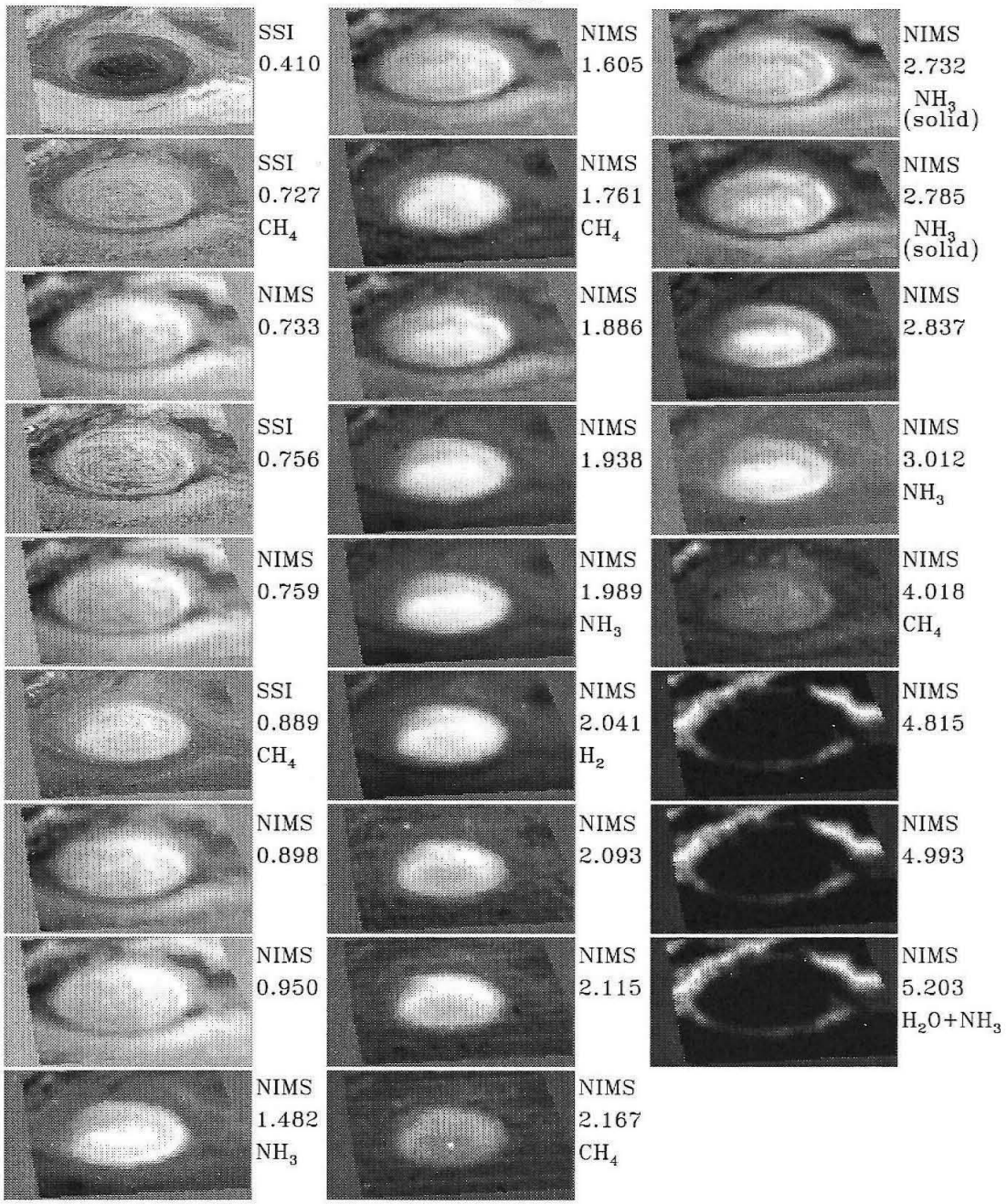

Figure 2.1: Combined SSI–NIMS image set for the GRS. The labels to the right of the image indicate the device that took the image (NIMS or SSI), the wavelength in μm, and the gas or solid having the absorption band at this wavelength. Spectral resolution (bandwidth) is about 0.0125 μm for $\lambda < 1\mu$m and 0.025μm for $\lambda > 1\mu$m. Images at $\lambda < 4.5\mu$m show the sunlight reflected from the clouds and absorbed by the atmospheric gases above the clouds. Images at $\lambda > 4.5\mu$m show thermal emission from the jovian interior.

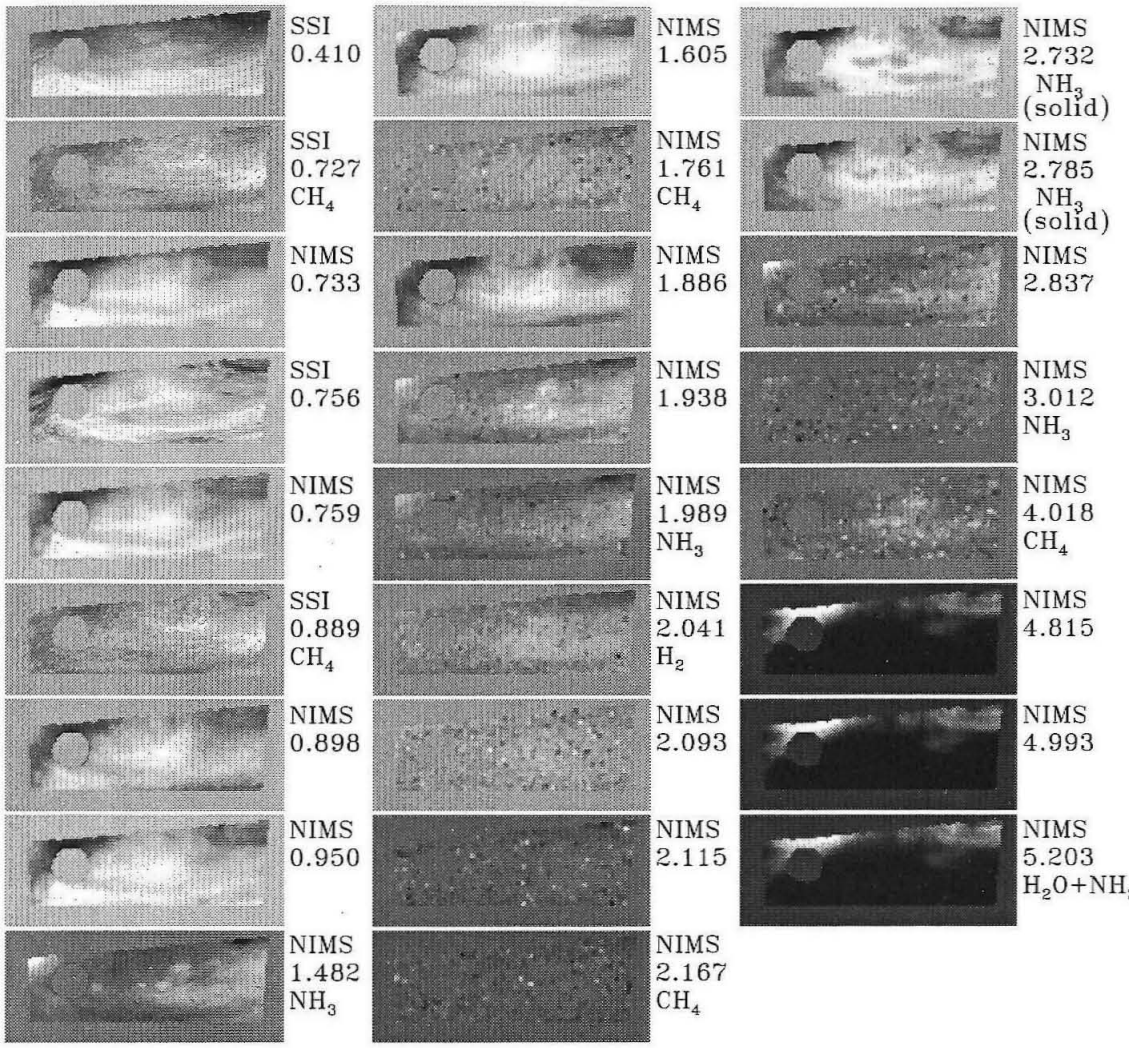

Figure 2.2: Combined SSI–NIMS image set for the hot spot. The circular area on each image is the shadow of Europa.

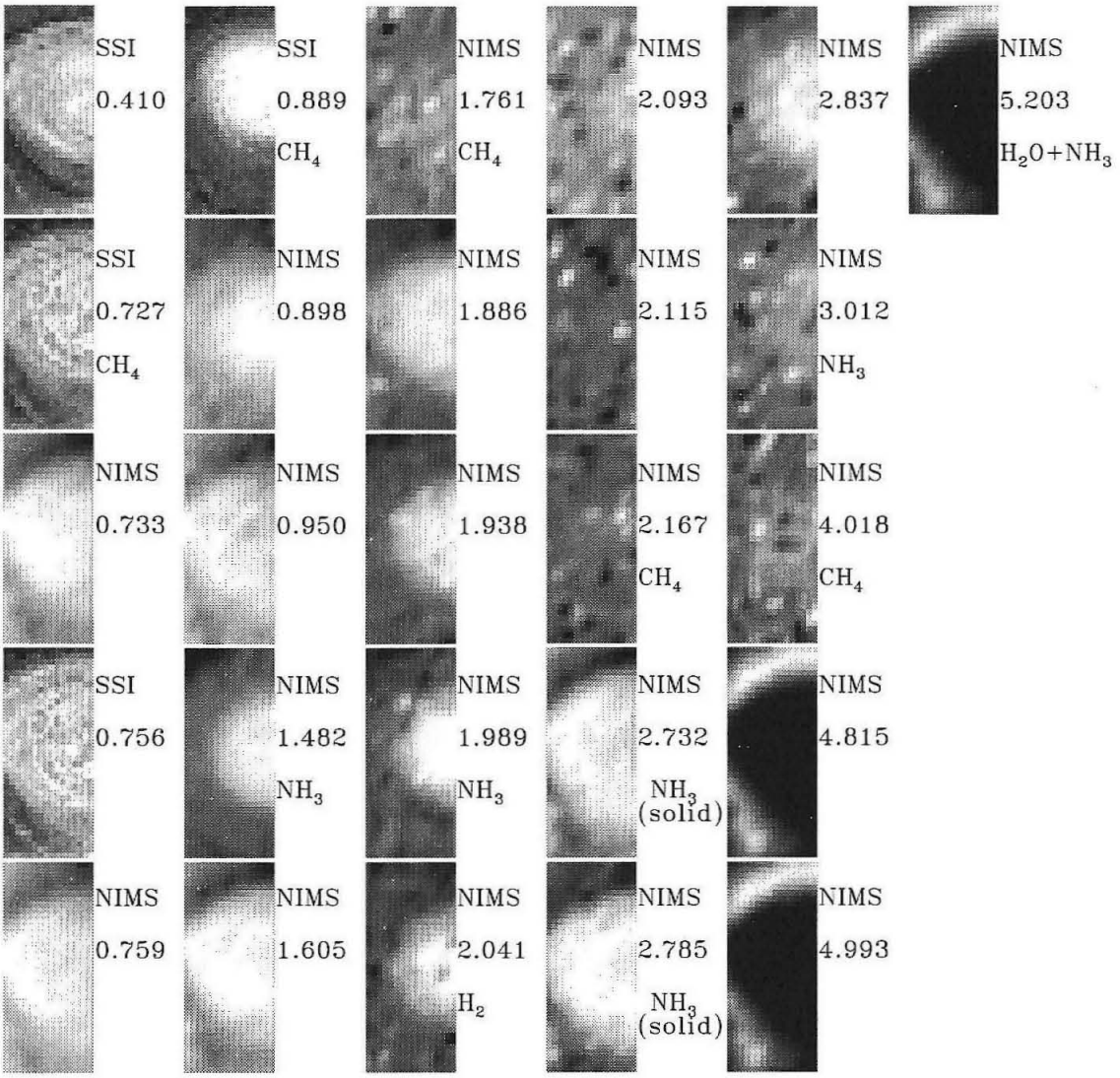

Figure 2.3: Combined SSI–NIMS image set for the white oval.

interesting to compare with the GRS results. The effects of combining images having different spatial resolution, observational noise effects, and wavelength uncertainty are discussed in Sections 2.5.1, 2.5.2, and 2.5.4.

2.3 Data Analysis

2.3.1 Application of PCA on the Image Data

Although PCA is a standard technique (Murtagh and Heck, 1987), each application is different. We summarize our approach below.

Consider repeated measurements (e.g., pixels) of some particular properties (e.g., brightness at different wavelengths) of a physical object. Call the number of measurements n and number of properties m. Now we can think of our data set as n data points in m-dimensional space. For the purpose of this work we consider each pixel on the 26 Galileo images as one measurement of $m = 26$ properties — brightnesses $X^p(\lambda)$ in 26 different wavelengths λ, where the index p denotes pixel. In other words, each pixel is a data point in a 26-dimensional wavelength space. For convenience we index wavelengths by l such that $l = 1, 2, ..., 26$ corresponds to λ=0.410 μm , 0.727 μm ,... ,5.203 μm . Then X_l^p corresponds to $X^p(\lambda)$. We do not pay special attention to the mean spectrum (averaged over all pixels in the image), as our data have a more interesting aspect — spatial variation at high resolution. The mean spectra for the GRS, Hot Spot, and White Oval regions are similar (see Fig. 2.4). Some properties of the mean spectrum will be discussed in Section 2.4.1. We subtract the mean spectrum from each data point to get the deviation from the mean:

$$\Delta X_l^p = X_l^p - \frac{1}{n_{pixels}} \sum_{p=1}^{n_{pixels}} X_l^p \quad .$$

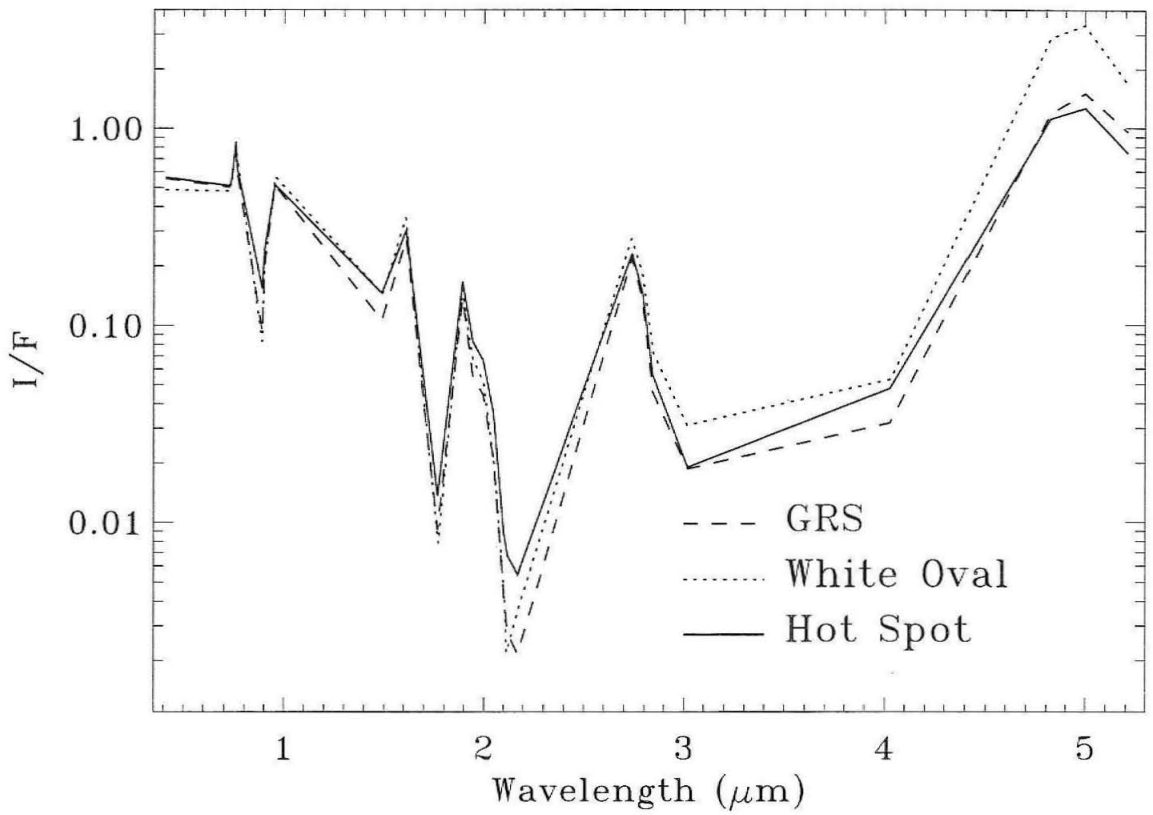

Figure 2.4: The mean spectra for the GRS, Hot Spot, and White Oval regions. The combined 26-wavelength spectrum is normalized by the incident solar light (I/F). To combine NIMS and SSI spectra, we renormalized the NIMS part of the spectrum such that I/F at 0.759 μm (NIMS) coincided with I/F at 0.756 μm (SSI). At $\lambda > 4.5\mu$m thermal emission from Jupiter is stronger than the reflected light (I/F > 1).

To treat measurements in the different wavelengths equally, deviations at each wavelength are normalized by the standard deviation σ_l over the image at this wavelength. We will call this method standard normalization:

$$\delta X_l^p = \frac{\Delta X_l^p}{\sigma_l} \qquad \text{where} \qquad (\sigma_l)^2 = \frac{1}{n_{pixels}} \sum_{p=1}^{n_{pixels}} (\Delta X_l^p)^2 \quad .$$

Another, noise–based normalization will be discussed in Section 2.5.3.

PCA seeks the best approximation of the data set by a few linear functions (PCs) of m wavelengths. The ith principal component can be written as a vector u_l^i (or PC_i), where $l = 1, 2, ..., m$. The vectors are orthogonal and normalized, so that

$$\sum_{l=1}^{m} u_l^i u_l^j = \delta_{i,j} \quad \text{for} \quad \text{any} \quad i, j, \qquad \text{where} \quad \delta_{i,j} = 1 \quad \text{if} \quad i = j, \quad \delta_{i,j} = 0 \quad \text{if} \quad i \neq j \quad .$$

Multiplying the first few principal components by the corresponding amplitudes A_i^p at the pixel p and summing, we can approximate the observed deviation from the mean at this pixel as

$$\delta X_l^p = \sum_{i=1}^{q} A_i^p u_l^i + (R_l^p)_q \quad ,$$

where $(R_l^p)_q$ is a residual brightness in point p at the lth wavelength after approximation by the first q PCs. Note that u_l^i is defined for the image as a whole, whereas the amplitude A_i^p is different for each pixel.

The approximation is evaluated by minimizing the sum of the squares of the residuals

$$\sum_{p=1}^{n_{pixels}} \sum_{l=1}^{m} ((R_l^p)_q)^2 \quad .$$

Principal components can be understood as a set of basis vectors in m-dimensional space chosen so that the maximum pixel-to-pixel variation in the data belongs to the subspace formed by one, two, three, etc., basis vectors. The problem can be solved as an eigenvalue problem for the correlation matrix S of m deviations averaged over all image pixels (see derivation in Murtagh and Heck (1987), chapter 2.2.3):

$$Su = \alpha u, \quad \text{where} \qquad S_{l_2}^{l_1} = \sum_{p=1}^{n_{pixels}} (\delta X_{l_1}^p \delta X_{l_2}^p) \quad .$$

It can be shown that the eigenvalue α gives the fraction of the total variance projected on the m-dimensional vector u (standard deviation along this axis). The m solutions ordered in decreasing order of α's are the principal components. In terms of the new coordinate system, the amplitude A_i^p is a coordinate of the pth data point in the ith dimension – the projection of the data vector δX_l^p onto the new unit vector u_l^i. Amplitudes A_i^p form a map of scalar coefficients according to the image pixels p for each ith principal component u_l^i.

2.3.2 Limitations of the Method

PCA gives useful results only in the case of high correlation (as in our data when the first eigenvalues are much larger than the next ones). In this case data can be meaningfully reduced to a few dimensions. PCA is a purely empirical method, and additional analysis is needed to explain the physics of the observed object.

2.4 Results

2.4.1 PCA Results

Using PCA we found that the pixel-to-pixel variations of brightness in the different wavelengths are highly correlated. This high correlation suggests that only a few independent spectral functions (PCs) are needed to describe most of the brightness variation. Namely, PCA for the GRS shows that 63% of the total variance is produced by the first principal component alone, 23% by the second one, and 4% by the third one. For the Hot Spot region, the corresponding percentages are 45% (PC_1), 17% (PC_2), and 6% (PC_3). For the White Oval the percentages are 61% (PC_1), 12% (PC_2), and 5% (PC_3). The lower percentages for the Hot Spot and White Oval regions are likely due to the data being noisier (see Figs. 2.1, 2.2, and 2.3) and therefore a larger fraction of the variance is an uncorrelated noise.

Before describing the principal components we describe some qualitative features of the spectra (Fig. 2.5b). First, high reflectance (I/F) occurs in the atmospheric windows (insets I–IV in Fig. 2.5b), where the absorption of the atmospheric gases above the clouds is minimal. If the area is brighter than its surroundings in the atmospheric window, it indicates a cloud that is optically thicker than its surroundings at this wavelength. Wavelengths of low reflectance are gaseous absorption bands (insets V–VII in Fig. 2.5b). A considerable fraction of the solar light is absorbed above the clouds at these wavelengths. If two clouds differ in brightness in absorption bands but are equally bright in an atmospheric window, it means the darker cloud is located deeper in the atmosphere. Equivalently, the darker cloud has fewer scatterers at high altitude (less haze). However, the effects of particle size, single scattering albedo, cloud opacity, and cloud elevation are hard to distinguish with our data. As PCA shows, the data have only a few independent modes of variation. Accordingly

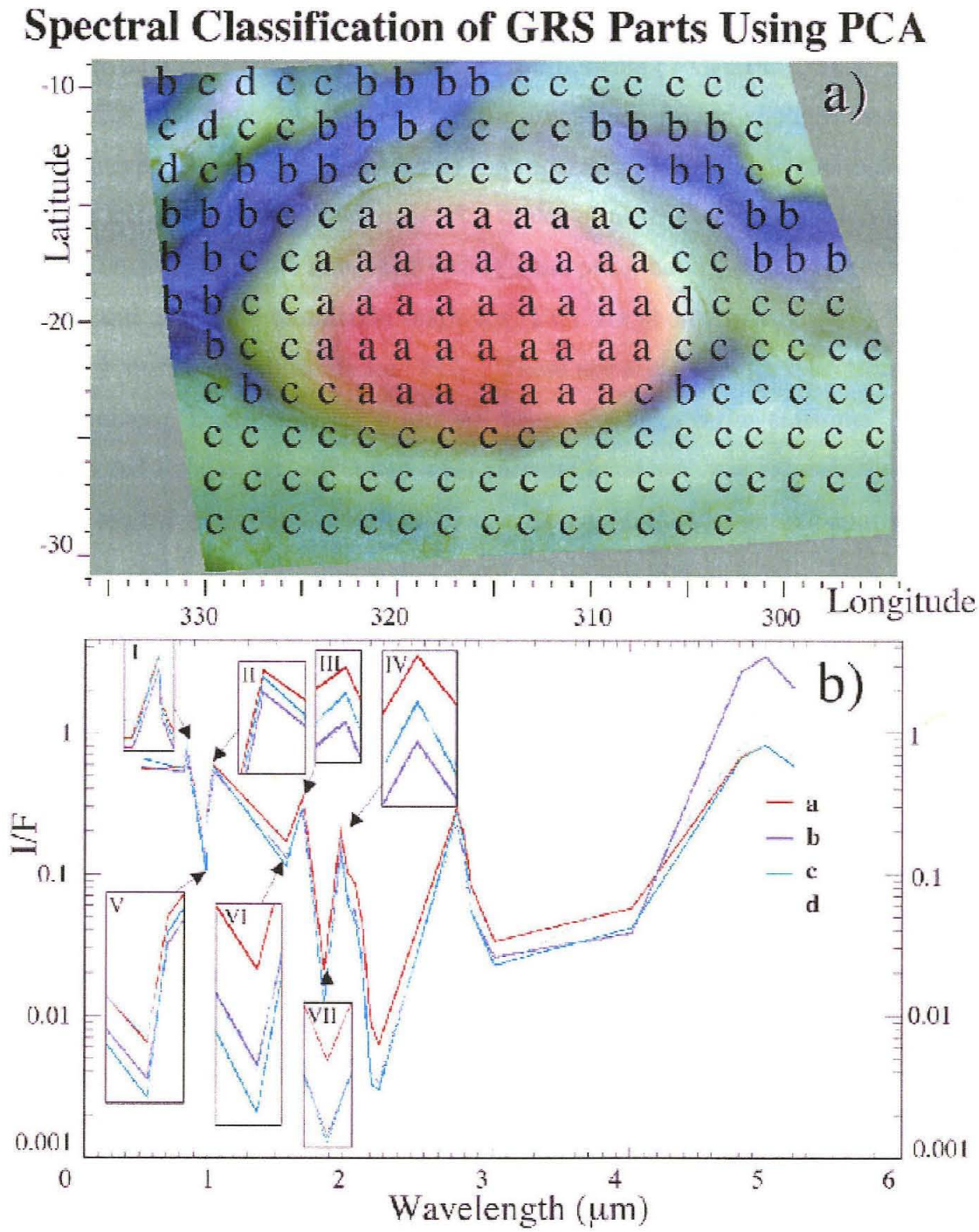

Figure 2.5: (a) False color map of GRS composed from the maps of PC_1, PC_2, and PC_3 as red, green, and blue, respectively. Areas shown in the same color have similar spectra. (b) Spectra for the different parts of the GRS. Each spectrum (a,b,c,d) is an average of several sample spectra taken in the corresponding area of the top map. The zoomed insets show window regions (I–IV) and gaseous absorption bands (V–VII).

we choose cloud elevation and opacity to interpret the data, treating these parameters as the most important ones for the reflected spectrum.

Figure 2.6 shows the first four principal components (PC_1 , PC_2 , PC_3 , and PC_4) for the GRS, Hot Spot, and White Oval regions. The reflected sunlight described by PC_1 (positive PC_1 values at $\lambda < 4.5\mu$m) is anticorrelated with 5-μm thermal emission (negative PC_1 values at $\lambda > 4.5\mu$m). The values of nearly zero correlation mean low signal-to-noise ratio in the images at strong absorption bands, as can be seen in Figs. 2.1, 2.2, and 2.3. The amplitude maps for PC_1 are shown in Fig. 2.7. The light areas show positive coefficients for PC_1 . These are areas of high reflection and low 5-μm emission. Dark areas show low reflection and high 5-μm emission. The fact that reflected light is anticorrelated with thermal emission was extensively noted in previous studies (see West et al. (1986) and Beebe (1997)) by simple comparison of the images taken in wavelengths shortward of 4.5 μm and in 5 μm. That gave rise to the idea that in some areas we see clouds reflecting sunlight and blocking 5-μm emission from the jovian interior. In other less cloudy areas, sunlight gets absorbed deep in the atmosphere and thermal emission escapes to space (see summaries in West et al. (1986) and Beebe (1997)). According to this interpretation, the coefficient in front of PC_1 is a measure of cloudiness. Light areas on the PC_1 map are cloudier than the dark ones. Since PC_1 is positive both inside and outside of the absorption bands, the clouds cannot be confined to low altitudes. The cloud tops must be high.

In the GRS region the reflectance in violet (0.41 μm) is anticorrelated with the reflectance in other wavelengths (0.72–4.5μm), unlike in the Hot Spot and White Oval regions where reflectances in all wavelengths are correlated. This difference in PC_1 demonstrates the color difference between the GRS and other (Hot Spot and White Oval) regions. In the GRS a violet absorber is present where the cloud is optically thick and high (e.g., inside the GRS). In the Hot Spot and White Oval regions, no violet absorber is associated with the cloud features.

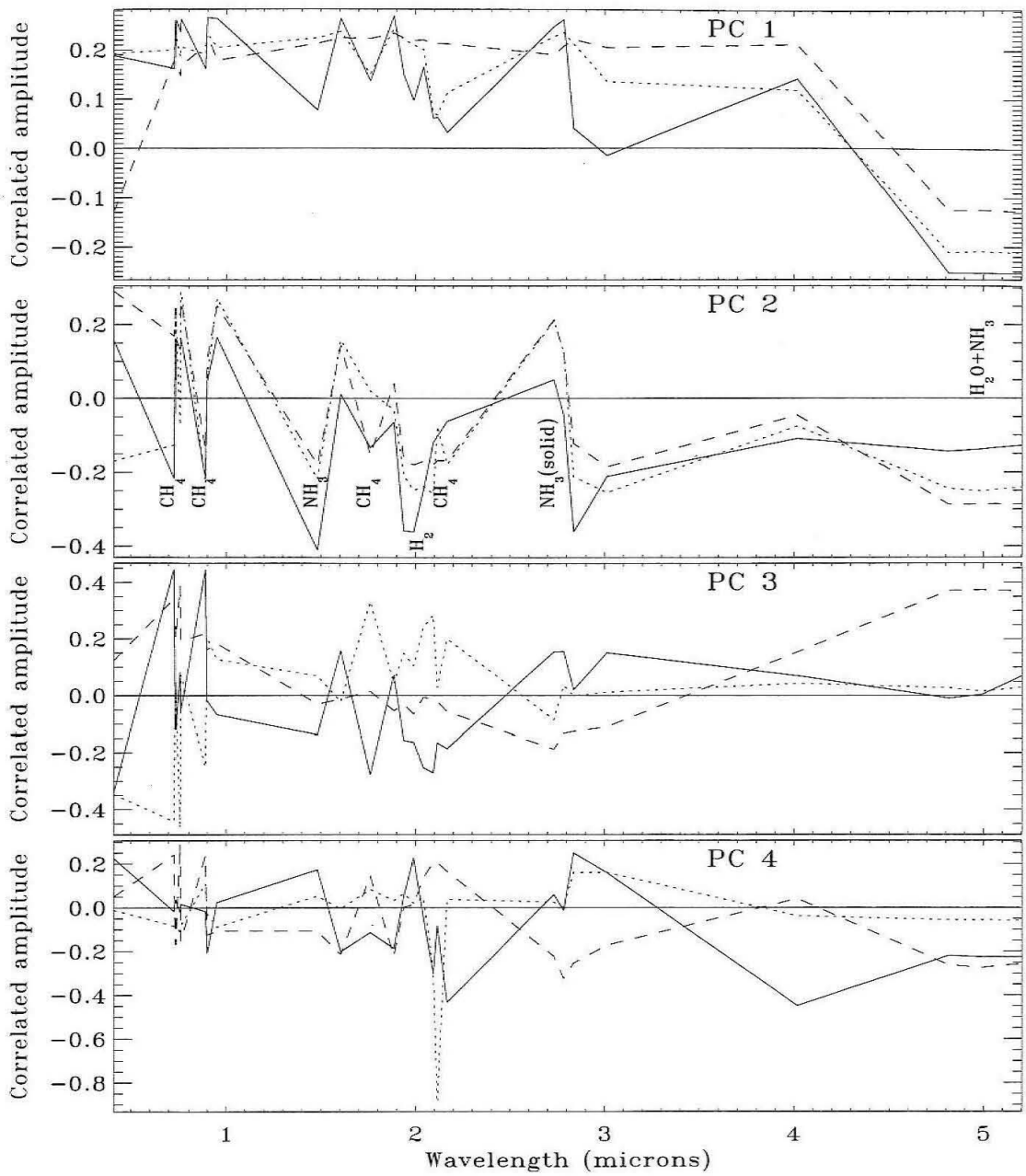

Figure 2.6: First four PCs for the three regions: GRS (dashed line), Hot Spot (solid line), and White Oval (dotted line). The gases absorbing at different wavelengths are indicated on the PC 2 plot. Correlated amplitudes of the same sign mean correlated deviation from the mean spectrum. Values of the opposite sign mean anticorrelation. Nearly zero value often means poor signal-to-noise ratio in the data image (see Figs. 2.1, 2.2, and 2.3). If the signal to noise is good, zero value means no correlation.

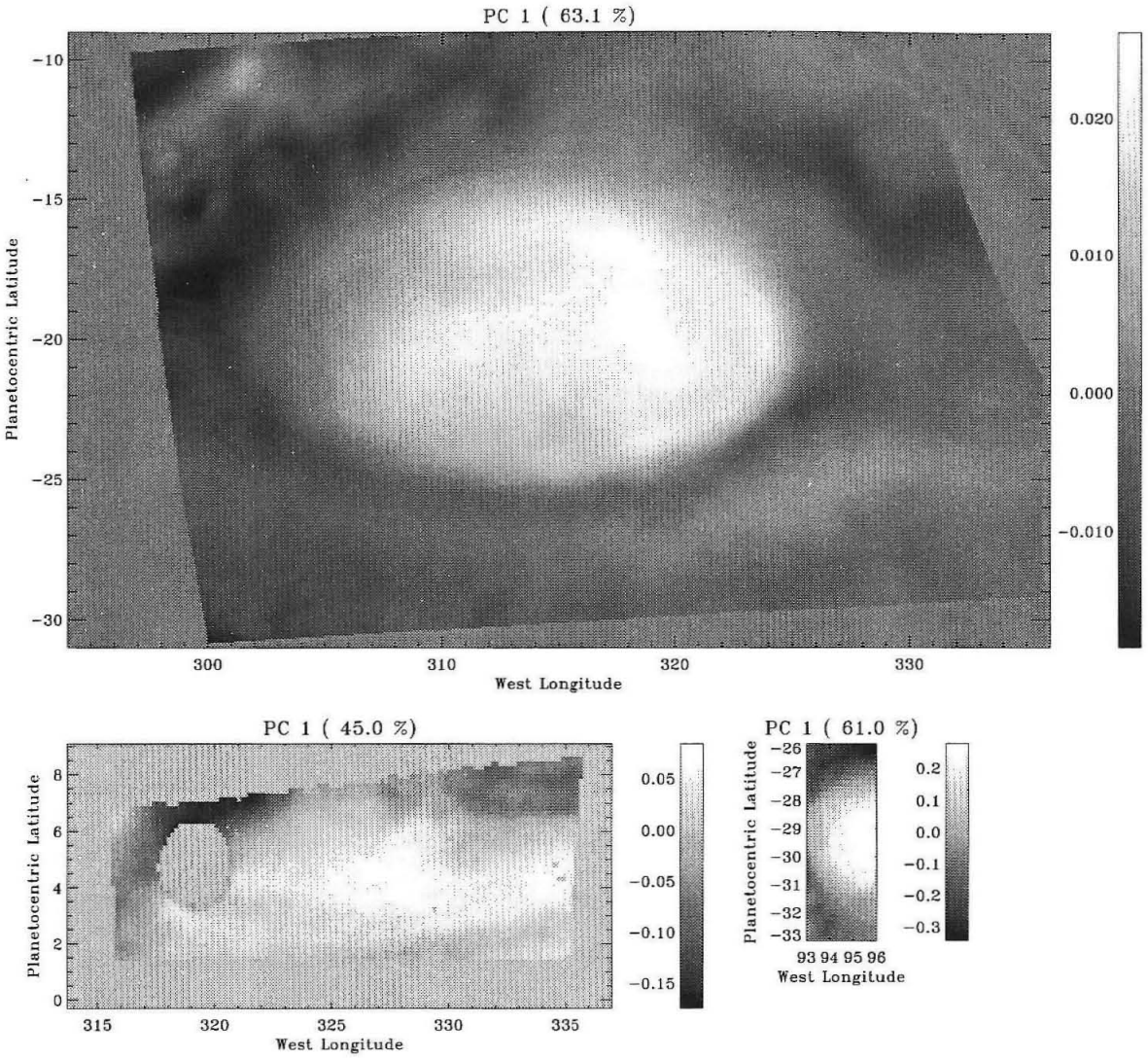

Figure 2.7: The maps of A_1^p (PC_1) for the GRS (upper), hot spot (lower left), and white oval (lower right). Coefficients A_i^p show the amount of deviation from the mean spectrum associated with each PC_i. One degree of latitude or longitude (planetocentric coordinates) is approximately 1200 km. The scale bar at the right of each image shows the values mapped. For example, PC_1 has high positive values inside the GRS (light on the map). It means that the area is bright in the images taken in reflected sunlight and is dark in 4.8—5.2 μm images.

PC_2 (Fig. 2.6) shows a correlation between 5-μm thermal emission and brightness in absorption bands and an anticorrelation between 5-μm thermal emission and brightness in atmospheric windows. The PC_2 map is shown in Fig. 2.8. A positive coefficient A_2^p in front of PC_2 can be interpreted as a low-altitude (dark in absorption bands) cloud (bright in atmospheric windows) blocking thermal emission. The upper tropospheric haze (West et al., 1986) has little effect in the atmospheric windows because it is optically thin, but it has a large effect in the gaseous absorption bands because it scatters light that would otherwise be absorbed. Therefore PC_2 describes an anticorrelation between opacity in the upper tropospheric haze and that of the low cloud, since the brightness in absorption bands is anticorrelated with brightness in atmospheric windows. To block 5-μm emission, the low clouds should be optically thick in these wavelengths and therefore have relatively large cloud particles (on the order of few microns or larger).

We do not interpret higher order PCs. Even though they show important correlations in the data, the corresponding A_i^p are small and therefore the amplitudes of these variations are small. Mathematical orthogonality of PCs does not imply that corresponding cloud properties are independent. Therefore it is hard to interpret the higher order PCs independently from the first ones. Another reason not to interpret the higher order PCs is that detection of them is not so robust as for the first PCs (see Fig. 2.6 and Sections 2.4.2, 2.5.1, and 2.5.2).

Maps for the first three PCs for the GRS are combined into a color map shown in Fig. 2.5a. Since it "explains" 91% of the variance, this color map is a convenient way of looking at the data at all 26 wavelengths. Instead of representing particular wavelengths, each color shows the spatial distribution of the correlated amplitude deviation in 26 wavelengths. It allows one to view, as different colors, spectrally different areas from all 26 maps. Areas shown by different colors in the map (Fig. 2.5a) have substantially different spectra (Fig. 2.5b). Similarly colored areas have

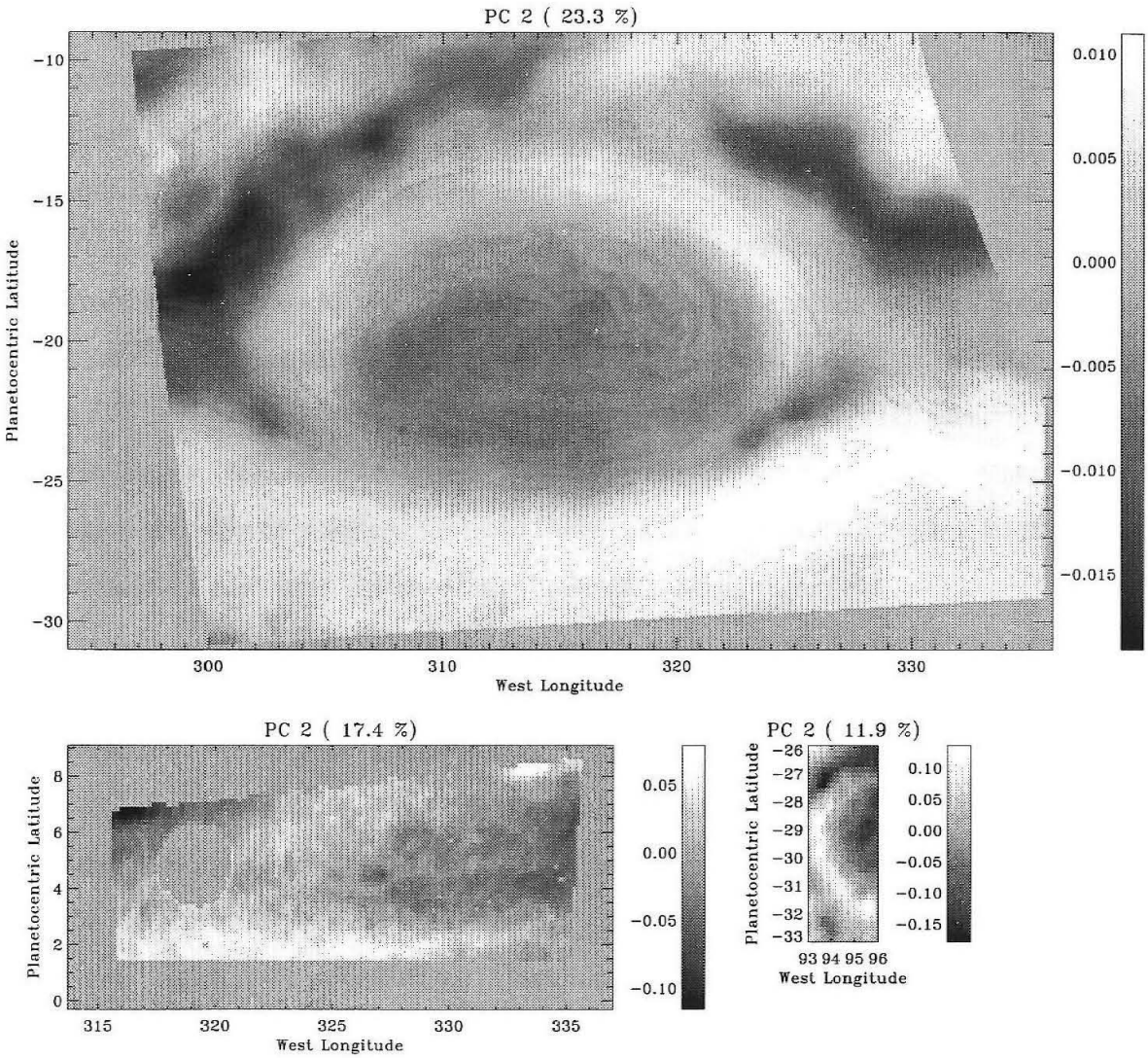

Figure 2.8: The maps of A_2^p (PC_2) for the three regions.

similar spectra.

Descriptions of the particular areas, the corresponding spectra, and their interpretation are given below.

Area a (red in Fig. 2.5) represents the interior of the GRS and is brighter than the average in reflected light (both atmospheric windows and absorption bands) and is darker than the average in 5-μm emission. It is usually interpreted as a thick, high, reflecting cloud containing large particles and blocking 5-μm emission from below. On top of this cloud an optically thick haze provides reflection in absorption bands.

Area b (dark blue in Fig. 2.5) is dark in atmospheric windows (I–IV) and bright at 5 μm. That suggests that the main cloud is optically thin. Surprisingly enough, area b is bright relative to area c in deep absorption bands (V–VII). Deep absorption bands display high-altitude clouds. That supports the idea that above the optically thin clouds in the troposphere (area b) there is a stratospheric and upper tropospheric haze, and it is optically thicker than the haze at area c.

Area c (green in Fig. 2.5) shows an optically thick cloud (it is almost as bright in atmospheric windows as the GRS, and it blocks 5-μm emission). The cloud is located deep relative to the other areas (it is dark in absorption bands).

Area d (light blue in Fig. 2.5) indicates two small-scale bright clouds to the northwest of the GRS. Also, a similarly colored area can be observed at the east edge of the GRS. What makes area d special? As can be clearly seen in Fig. 2.1, area d is the brightest spot in the 4.018-μm image. Figure 2.5b shows the same thing: At 4.018 μm, area d is brighter (higher I/F) than any other area. In most of the other wavelengths area d is not very different from the average (see light blue line d in insets II–VII). This unusual spectrum cannot be explained by the two parameters (cloud opacity and elevation) that we were using above. We can think of five different mechanisms that can explain the unusual spectrum of area d.

One explanation is that area d is the brightest in 4.018 μm because area d is the

highest cloud. In other areas (for example at the center of the GRS) clouds are lower and therefore shadowed by the gas absorption above. If that is true, curve d must be the brightest in all gaseous absorption bands (see insets V–VII in Fig. 2.5). However curve d is not the brightest and therefore this explanation seems unlikely.

The second explanation is that 4.018-μm absorption is due to some gas other than the ones absorbing in other wavelengths. Then the unusually low mixing ratio of this gas above the clouds in area d can make it bright. However, most of the absorption at 4.018 μm is likely to be due to CH_4 gas (see Roos-Serote et al. (1998)). Therefore this explanation also seems unlikely.

The third explanation is that the unusual brightness in area d can be due to the thermal emission instead of reflected sunlight (see Roos-Serote et al. (1998)). The problem is that area d is not bright at 4.8, 4.9, or 5.2 μm , which are the thermal emission wavelengths.

The fourth explanation involves particulate absorption. Assume that the cloud particles in all other areas except area d have a 4.018-μm absorber, but area d does not. Then area d will be a bright spot in the 4.018-μm image. Although this explanation can be true, the absorber has not been identified.

The last explanation is that the particles in the cloud are large. Assuming Mie scattering (see Goody and Yung (1989) or Hansen and Travis (1974)), a 5-μm particle would be about 10 times more efficient in scattering at this wavelength than a 1-μm particle. The cloud in area d with 5-μm particles surrounded by clouds with 1-μm particles would stand out more at the longer wavelength. This size range is consistent with other studies (see Rossow (1978), West et al. (1986)). The large-particle hypothesis is easy to explain dynamically. The precipitation time to fall 1 scale height is ~years for 1-μm particles and is ~weeks for 5-μm particles (see Rossow (1978)). Therefore it is likely that a high population of large particles would not survive in the slow-mixing regions, but they would survive in the fast-mixing

regions — the convective updrafts. Other data (Belton et al., 1996; Banfield et al., 1998) suggest that area d is a convective region.

2.4.2 PCA for the Different Regions

The GRS is an unusual region on Jupiter. PCA reveals properties of the whole region studied but not necessarily properties of the parts of this region. To see if the principal components represent global properties on Jupiter we performed PCA on different areas. First, we used parts of the GRS image. Also, we studied the Hot Spot and White Oval data sets (see comparison in Section 2.4.1). As a general rule, in the GRS, PC_1 remains the same within 20–30% uncertainty if the analyzed area had any contrast in all wavelengths and included the 5-μm emission area. An exception is the anticorrelation of violet reflectance with reflectance in other wavelengths (see Fig. 2.6 for the GRS where PC_1 is negative at $\lambda = 0.41$ μm). This anticorrelation shows up only at the GRS and dark collar around it; it does not show up either in other parts of the GRS region or in other (Hot Spot and White Oval) regions. PC_2 also remained similar (30–40% uncertainty) with the exception of the violet wavelength. This suggests a local distribution of the chromophore over the GRS. Higher order principal components do not show much resemblance and therefore do not represent homogeneously distributed properties that can be found in every part of the studied regions. That was one of the reasons to consider only PC_1 and PC_2 for the interpretation.

2.4.3 Reconstruction of the NIMS Images Using SSI Maps

The high correlation between the NIMS and SSI data suggests that SSI might serve as a proxy for all the NIMS data; in other words we may ask, what fraction of the

variance in SSI–NIMS data can be reconstructed using only SSI images and PCs calculated for 26 wavelengths? This reconstruction is important because the SSI images have better resolution. If correlations at the small scale are similar to the large-scale correlations, our reconstruction does approximate NIMS images with high resolution. Unfortunately, it is not possible to check without having 30 km/pixel (SSI) resolution images at the NIMS wavelengths.

Before the reconstruction, we perform a separate PCA on the SSI data set and get four principal components in four SSI wavelengths PC_i^{SSI}, where $i = 1, 2, 3, 4$ are the order of SSI-only principal components. Then we compare PC_i^{SSI} with the fragments of PC_i taken in SSI wavelengths (see Fig. 2.9). The first two PCs show similar correlations, but the third and fourth look different. This suggests that probably only the first two PCs will be useful for the reconstruction. After our attempt to use three or four PCs instead of only two, the accuracy of the reconstruction became substantially worse. Accordingly, the following discussion will concern the reconstruction by only two PCs, such that $q = 2$.

To reconstruct images in different wavelengths, we use the same idea as for the PCA reconstruction by first q principal components $\mathrm{PC}_i \equiv u_l^i$ (see Section 2.3.1).

$$\delta X_l^p \approx \delta \bar{X}_l^p = \sum_{i=1}^{q} \bar{A}_i^p u_l^i, \qquad \text{where} \qquad l = 1, 2, ..., 26$$

Here δ denotes deviation from the mean brightness. Instead of using the amplitude coefficients A_i^p from the PC maps, we use the coefficients $\bar{A}_i^p$ derived from SSI images as follows. For every pixel p in the four SSI images, we found the best-fit coefficients $\bar{A}_1^p$ and $\bar{A}_2^p$ in front of the fragments of PC_1 and PC_2 by minimizing the least square error,

$$\sum_{l=1,2,4,6} (\delta X_l^p - (\bar{A}_1^p u_l^1 + \bar{A}_2^p u_l^2))^2 \quad ,$$

where $l = 1, 2, 4, 6$, which are the wavelength indices corresponding to the four SSI

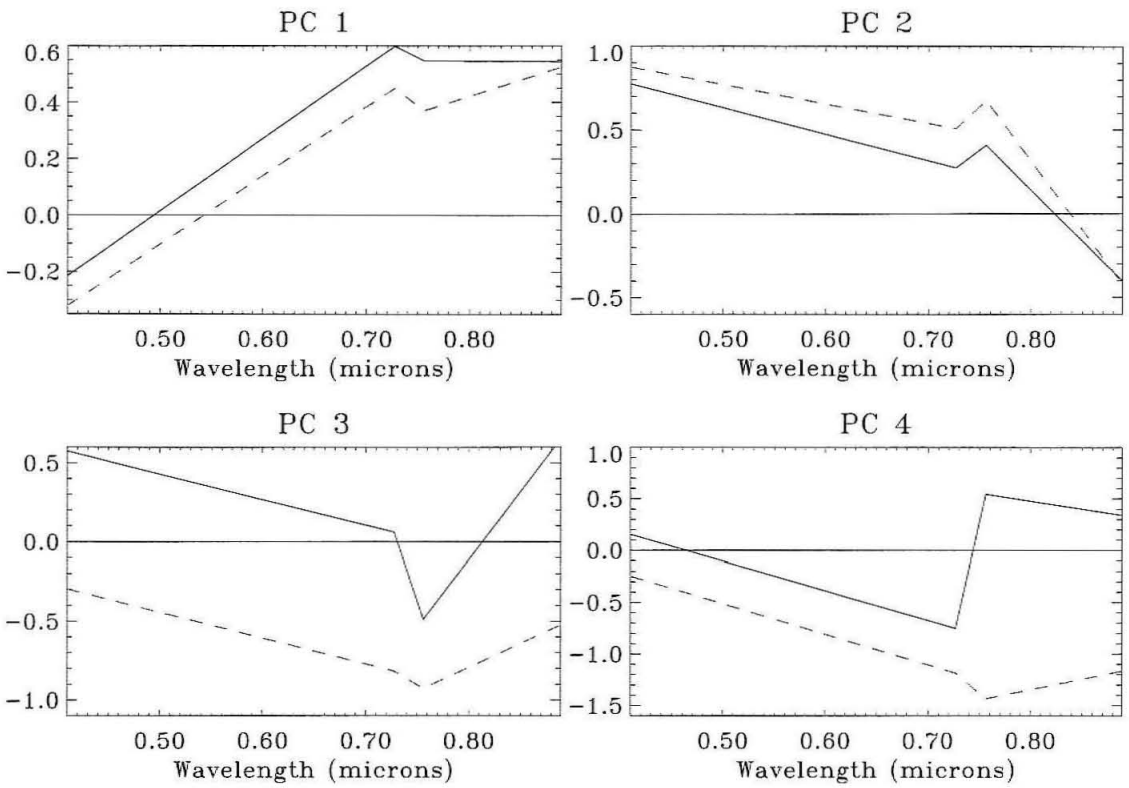

Figure 2.9: Comparison of the PC_i^{SSI} (solid line) with the fragments of PC_i at SSI wavelengths (dashed line). The amplitude of correlation (plotted on the ordinate) for the fragments of PC_i was normalized such that the fragments have unit absolute value in four SSI wavelengths: $\sum(u_l^i)^2 = 1$ where $l \in SSI$.

wavelengths. The results of the reconstruction for all NIMS–SSI wavelengths and the corresponding data images can be seen in Fig. 2.10. The reconstructed images (left images in the pair) and the data images (right images in the pair) are scaled by the brightness range for the best contrast. That allows one to see the similarity in the geometric patterns, but not the reconstructed amplitude. The geometric patterns of the NIMS images are reconstructed well even for the 5-μm images. To quantitatively estimate the reconstruction quality in terms of amplitude, we subtracted our reconstruction from the data, obtaining residual images $\bar{R}_l^p = \delta X_l^p - (\bar{A}_1^p u_l^1 + \bar{A}_2^p u_l^2)$. Then for every wavelength we calculated the variance in the residual images as a fraction of the data variance. The rest of the variance V_l is explained by the reconstruction

$$V_l = 1 - \frac{\sum_p (\bar{R}_l^p)^2}{\sum_p (\delta X_l^p)^2} \quad .$$

The values of the fractional explained variance V_l for different wavelengths are shown in Fig. 2.10. This reconstruction using the first two PCs and 4 out of the 26 images explains V= 62% (V is a V_l averaged over wavelengths) of the total variance in the data set (recall that the first two PCs explain 86% of the variance when the amplitudes are computed from the 26 wavelengths).

2.5 Error Analysis

2.5.1 Spatial Resolution Effects

The data set for the PCA should be homogeneous — or for our case images in all wavelengths should have the same spatial resolution. However, the SSI resolution is roughly 10 times better than that of NIMS. To get the same resolution for the images

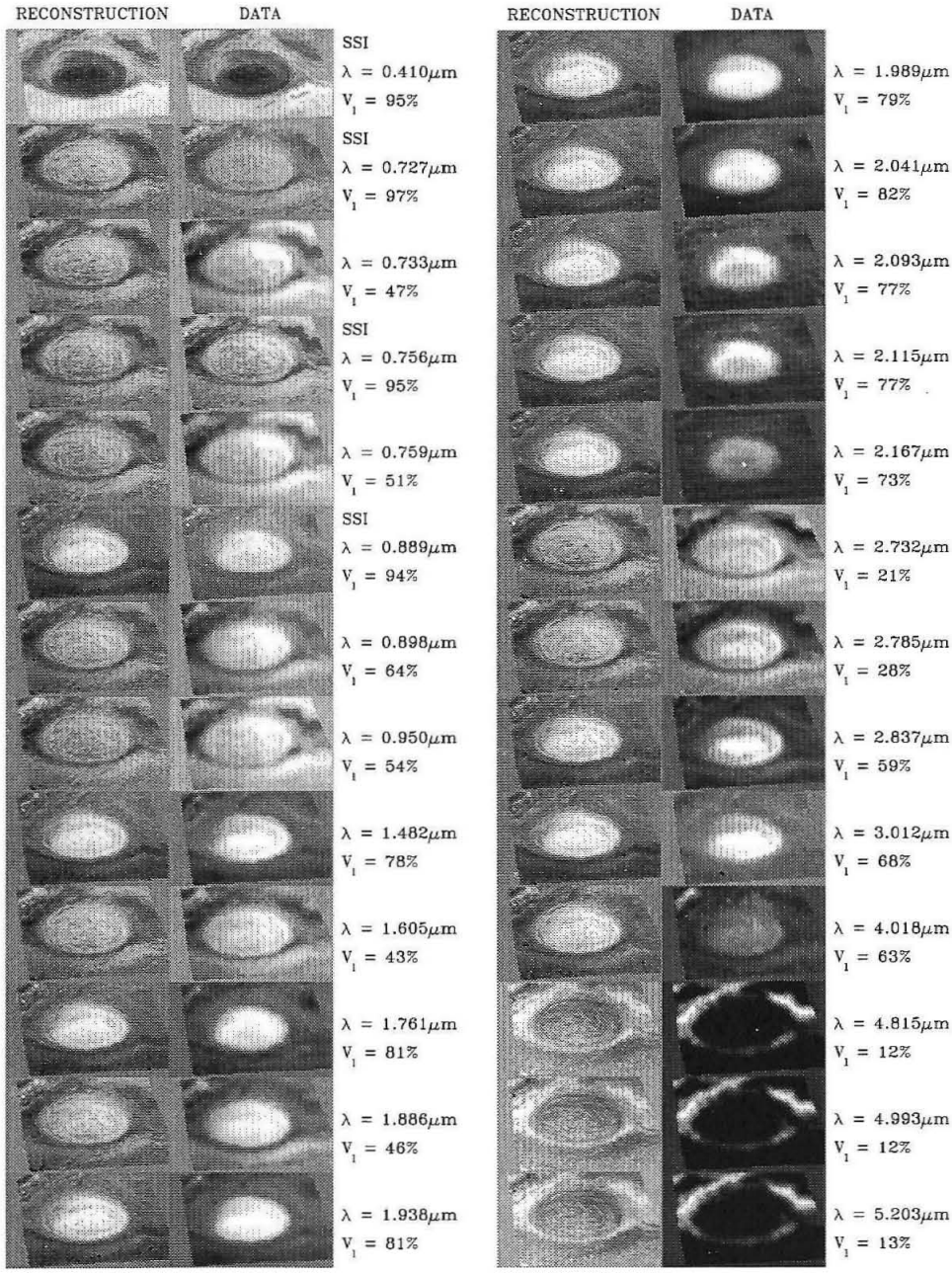

Figure 2.10: Images of the GRS in SSI and NIMS wavelengths reconstructed using PC_1, PC_2, and four SSI images (images at the left) compared to the data (images at the right). The corresponding wavelengths and percentages of the explained variance V_l are shown to the right of the two images.

in all wavelength we tried two methods:

1. interpolating the NIMS images at the SSI geometrical points, i.e., getting "high-resolution" NIMS images to put together with SSI and

2. averaging SSI pixels in a 10 X 10 area corresponding to the NIMS pixel to get low-resolution images for SSI wavelengths.

We compared the PCA results for both methods for the GRS and also tried the case when the resolution was 10 times less than that of NIMS to see the spatial-resolution effect. The first few principal components were almost exactly the same for cases 1 and 2 above. Namely, the difference of the principal components is less than 0.1%, 0.15%, 0.5%, and 2% for first, second, third and fourth PCs respectively (the difference is evaluated at the wavelength where it is greatest and is normalized by the peak to trough amplitude of the PC). For a very coarse resolution (10 times NIMS) first principal components are still very similar to the ones for SSI resolution (with differences of less than 2%, 2%, 15%, 20%). The similarity in principal components for different spatial resolutions suggests that the PCs display large-scale features rather than small-scale cloud variations.

2.5.2 Observational Noise Effect

The brightnesses in different wavelengths are subject to observational noise (thermal, instrumental, cosmic-ray-induced, etc.). It is different for different wavelengths. In SSI images it is roughly the digitization level (the noise is on the order of 1 data number (DN), while the signal approaches 256 DN). For NIMS the gain for the detectors is the same for all wavelengths (see Carlson *et al.* 1992). The detector noise is a few percent of 256 DN, which is a maximum signal level. The actual signal level changes from wavelength to wavelength giving different signal-to-noise ratios (see Fig. 2.11).

To study the sensitivity of PCA to observational noise, we tested the response to

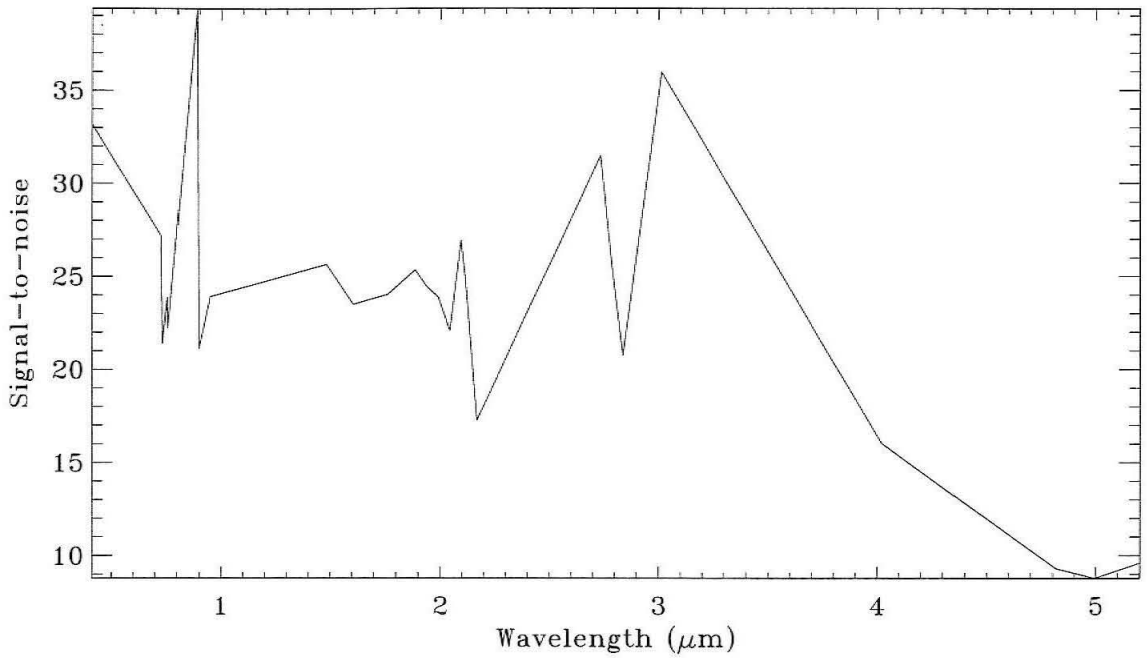

Figure 2.11: Signal-to-noise ratio for the GRS at different wavelengths used for the noise-based normalization. The detector noise is assumed to be 5 DN.

random noise added to the GRS data. Emulation of realistic detector noise (which has a standard deviation of 5 DN in each detector) gave an agreement of PC_1 within 3% at $\lambda < 4$ μm and within 16% at 4–5 μm; PC_2 gave agreement within 3% everywhere; both PC_3 and PC_4 gave agreement within 25%. PC_5 and higher order PCs varied substantially at different realizations of random noise. Therefore only the first four PCs are robust in representing the atmospheric properties at the GRS.

2.5.3 Noise-Based Normalization

To check the stability of our results, instead of normalizing each wavelength by its standard deviation (see Section 2.3.1), we normalized by the observational noise (Fig. 2.11). As a result, the amplitudes of the data images differ by an order of magnitude at different wavelengths. The resulting PCs are similar to the ones obtained in PCA with the standard normalization (see the case of the GRS in Fig. 2.12).

	PC_1 (%)	PC_2 (%)	PC_3 (%)	
GRS	63.2	23.3	4.8	Standard normalization
	66.9	21.0	5.0	Noise-based normalization
Hot Spot	44.6	17.3	6.1	Standard normalization
	41.9	16.7	9.4	Noise-based normalization
White Oval	61.1	11.9	5.0	Standard normalization
	59.6	12.0	6.1	Noise-based normalization

Table 2.2: Percentages of variance associated with the principal components in the case of standard and noise-based normalization

Percentages of the explained variance for the noise-based normalization are similar to ones for the standard normalization. The comparison is given in Table 2.2.

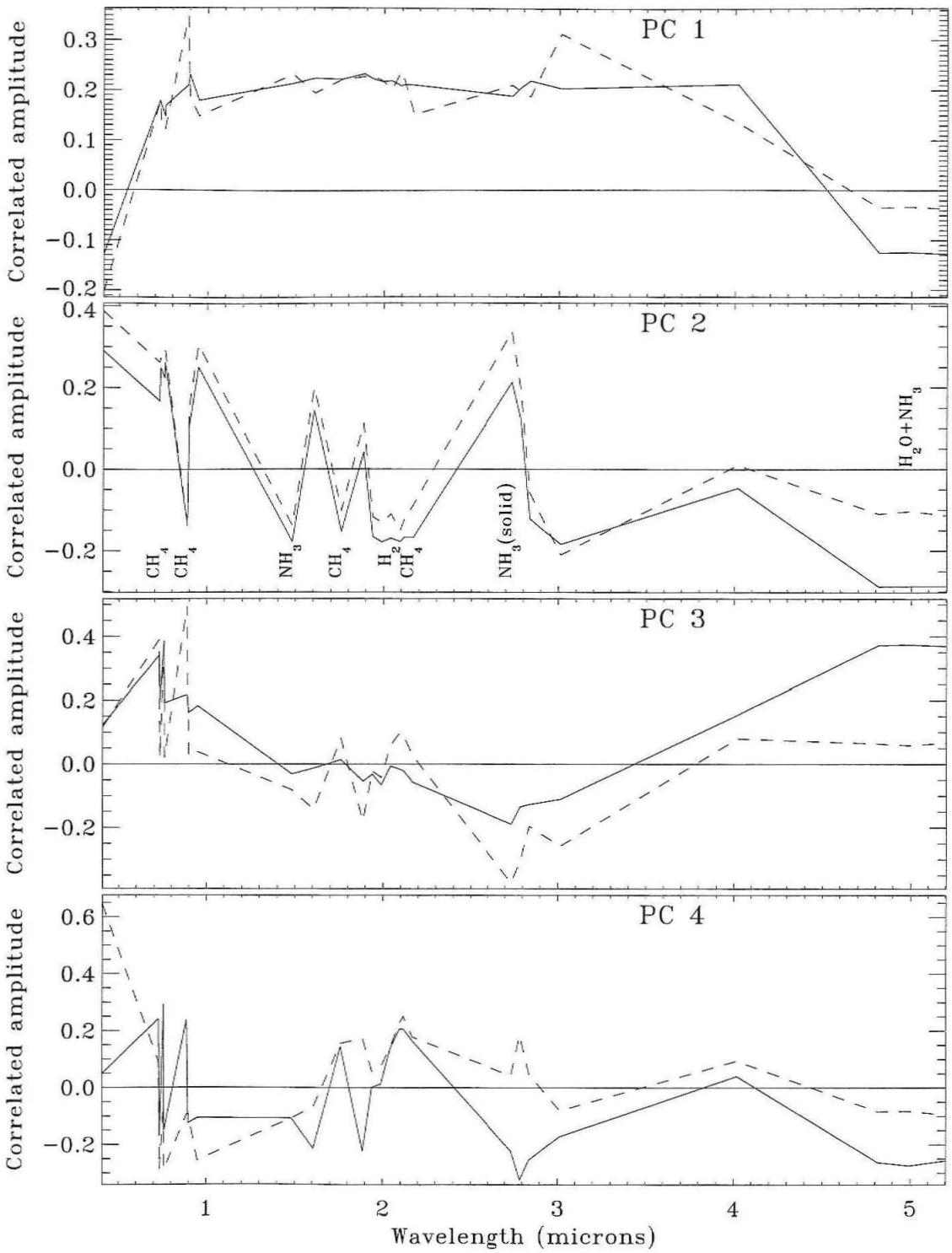

Figure 2.12: First four principal components for the GRS calculated using standard normalization (solid lines) and noise-based normalization (dashed lines).

2.5.4 Wavelength Uncertainty

The wavelength calibration of NIMS images (see Carlson *et al.* 1992) changes during the mission. The wavelength shift is estimated to be on the order of 50 Å(0.005 μm), which is tens of percents of detector bandwidth. The PCA results do not include wavelength calibration and do not depend on the exact wavelength value. The wavelength shift also is too small to be important when we have to decide if the wavelength belongs to the absorption band.

2.6 Discussion

The PC_1 map (Fig. 2.7) shows increased optical thickness and increased elevation of the cloud inside the GRS and White Oval (see Section 2.4.1). This result is consistent with other studies performed on the parts of the same data set. It agrees with the cloud structure derived for the GRS by Weir et al. (1997) using a point-by-point fit to the NIMS maps in four near infrared wavelengths. In their results the middle of the GRS is elevated and cloudy above 0.6 bars, which is about the NH_3 condensation level assuming solar NH_3 mixing ratio.

Banfield *et al.*'s (1998) conclusions are based on fits to the SSI images in three wavelengths with varying observational geometry. These results show the same increases in optical depth and cloud elevation over the GRS and decrease in the collar around it. The small clouds to the northwest of the GRS (our area d in Fig. 2.5) were interpreted by Banfield *et al.* (1998) to be extremely optically thick and high (optical depth > 20 at 400 mbar). Our results agree with that and in addition suggest the presence of large particles (see Section 2.4.1), implying unusually strong precipitation. Comparison with Banfield *et al.*'s (1998) model is especially important as we used the same data but combined them with NIMS images.

According to West *et al.* (1986), an optically thick cloud near the NH_3 condensation level should contain large NH_3-ice particles ($3 - 100$ μm) snowing down to the equilibrium condensation level where they sublimate. NH_3 gas is highly depleted in the cloud by precipitation. To support optical thickness of the cloud, there should be a source of fresh NH_3 at the cloud level. There are two mechanisms to bring NH_3 to the cloud from the lower levels: a large-scale updraft and turbulence. It is likely that both mechanisms work together. Both the updraft and increased turbulence would elevate the upper boundary of the cloud by bringing NH_3 to higher altitudes. We interpret PC_1 as a measure of cloud optical thickness correlated with the cloud elevation (see Section 2.4.1). Therefore, the positive values on the PC_1 map can be interpreted as an updraft and/or an increase in turbulence at least as high as the NH_3 condensation level.

The PC_2 map in Fig. 2.8 shows an anticorrelation between the high tropospheric haze and the low 5-μm absorbing cloud. This anticorrelation dominates where the PC_1 amplitude is small and the PC_2 amplitude is large. It cannot be explained by the updraft or downdraft continuing through troposphere to stratosphere. According to West *et al.* (1986) the haze is likely to be composed of 1-μm-size particles. The lifetime of these particles against precipitation is of the order of years (Rossow (1978)), and a high optical depth can be supported by rather gentle mixing in the atmosphere. A possible explanation for an anticorrelation between stratospheric haze and the cloud in the lower levels is that the air descends at high altitude and ascends at low altitude, and vice versa. Inferences based on lightning observations (Ingersoll *et al.* 2000) seem to bear this out.

Chapter 3 Monte Carlo Radiative Transfer Modeling of Lightning Observed in Galileo Images of Jupiter

We study lightning on Jupiter and the clouds illuminated by the lightning using images taken by the Galileo orbiter. The Galileo images have a resolution of 25 km/pixel and are able to resolve the shape of the lightning flashes, which have full widths at half maximum in the range of 90-160 km. (Little et al., 1999). We compare the lightning images with the images produced by our 3D Monte Carlo light-scattering model.

The model calculates Monte Carlo scattering of point-size photons in a 3D opacity distribution. During each scattering event, light is partially absorbed. The new direction of the photon after scattering is chosen according to the Henyey-Greenstein phase function. An image from each direction is produced by accumulating photons emerging from the cloud in a small range of emission angles. Lightning bolts are modeled either as points or vertical lines.

Our results suggest that some of the observed scattering patterns are produced in a 3-D cloud rather than in a plane-parallel cloud layer. Lightning is estimated to be as deep as the bottom of the water cloud. For the six cases studied, we find that the clouds above the lightning are optically thick ($\tau > 5$). Jovian flashes are more regular and circular than the largest terrestrial flashes observed from space; there is nothing equivalent to the 50-km horizontal flashes seen on Earth.

The content of this chapter is submitted to Icarus (Dyudina and Ingersoll, 2001).

3.1 Introduction

Lightning in the atmosphere of Jupiter acts as a natural probe of the cloud structure. The light from lightning penetrates clouds, gets scattered, and brings us information about shape, size, and opacity of the clouds, and about lightning itself. From the optical energy of lightning one can estimate the total energy associated with lightning on Jupiter (Borucki and Williams, 1986; Borucki and Magalhães, 1992; Little et al., 1999). The presence and high energy of the lightning suggests strong moist convection (Gierasch et al., 2000), which can explain the observed large-scale winds and striped appearance of the planet (Ingersoll et al., 2000).

The depth of the lightning below the cloud tops determines the pressure and temperature at which the discharge occurs. The pressure and temperature, in turn, determines if water or other chemicals precipitate to form the storm cloud. Lightning-induced production may be one of the major sources of important trace species such as C_2H_2, HCN, and CO. The production rate of these species is very sensitive to the pressure level, which makes the lightning depth also important for atmospheric chemistry (Bar-Nun and Podolak, 1985).

Lightning has been directly observed by optical imaging on the night side of Jupiter by Voyagers I and II (Smith et al., 1979; Cook et al., 1979; Magalhães and Borucki, 1991), the Galileo orbiter (Little et al., 1999; Gierasch et al., 2000), and the Cassini spacecraft (Porco *et al.*, in preparation). Other direct evidence of lightning are Voyager 1 whistler observations (Scarf et al., 1979) and radio frequency signals detected by the Galileo probe (Rinnert et al., 1998). Reviews of jovian lightning observations can be found in Williams et al. (1983), Uman (1987), and Rakov and Uman (2001).

In this study we use Galileo images showing diffuse spots of lightning seen through optically thick clouds. The spatial resolution is about 25 km/pixel, which is better than the 37, 100 and 60 km/pixel resolution of Voyager 1, Voyager 2, and Cassini respectively. We model the lightning spot size to derive the lightning depth below the cloud tops. Because the lightning spots observed by Galileo are spatially well resolved, we can accurately determine the shape of the brightness falloff in the lightning spots. Unlike similar Monte Carlo models used for terrestrial (Thomason and Krider, 1982; Koshak et al., 1994) and jovian lightning (Borucki and Williams, 1986; Little et al., 1999), our model reproduces images of lightning at different emission angles and is also capable of modeling three-dimensional, non-plane-parallel clouds. This allows us not only to determine the depth of the lightning but also to test different geometries of the clouds and lightning flashes by fitting the brightness distribution in the images.

To compare jovian and terrestrial lightning images, we make a short study of lightning images taken by the Lightning Imaging Sensor (LIS), which monitors lightning in Earth's tropics from space.

The structure of the paper is as follows. In Section 3.2 we describe the lightning images. Section 3.3 describes our Monte Carlo radiative transfer model. Section 3.4 contains the results of the modeling. Section 3.5 is devoted to comparison of jovian and terrestrial lightning. Section 3.6 contains the discussion of our results.

3.2 The Data

The lightning flashes were observed by the Galileo spacecraft on the night side of Jupiter in November 1997, Galileo orbit E11 (Little et al., 1999), and in May 1999, orbit C20 (Gierasch et al., 2000). Six lightning spots are studied. These are the only spots in Galileo data at which the brightness distribution is well resolved, *i. e.*, they satisfy the following criteria:

The brightness in the flash must not be saturated.

The spot should not overlap with other lightning spots.

The spot must be large, at least 5-6 pixels across. Many of the Galileo flashes do not satisfy these criteria and we do not study them here.

Table 3.1 shows the characteristics of the lightning flashes. Note that the largest

Flash	Resolution (km/pix)	Lat. (deg)	Orbit	Exposure time (sec)	Filter	Reference
1	26	47.5	E11	6.4	CLR	Little et al. (1999), storm 26, Fig. 9a)
2	27	56.1	E11	6.4	CLR	Little et al. (1999), storm 22, Fig. 9b)
3	23	48.5	E11	166.9	RED	Little et al. (1999), storm 24, Fig. 9c)
4	26	48.8	E11	6.4	CLR	Little et al. (1999), storm 23, Fig. 5, left
5	25	-14.5	C20	6.4	CLR	Gierasch et al. (2000), Fig. 1, left edge of the right storm
6	25	-15.5	C20	6.4	CLR	Gierasch et al. (2000), Fig. 1, center of the right storm

Table 3.1: Characteristics of the flashes. Clear filter (CLR) spans the wavelengths from 385 to 935 nm, red filter (RED) spans 625 to 705 nm (Little et al., 1999)

flashes are also the best spatially resolved. The images are in the HIS (summation) mode, in which the pixels are two times wider than the point spread function (Klaasen et al., 1997). Accordingly, we consider the effects of the point spread function negligible (see also Little et al. (1999)).

The exposure times in Table 3.1 are much larger than 0.5 seconds — the usual duration of terrestrial intracloud or cloud-to-ground multiple-stroke flashes (Williams et al., 1983). Therefore, it is likely that the full duration of the flash is recorded in

each image. The average flash rate in one storm can be approximated from three "scanned" frames, which were recorded when the Galileo camera footprint was moved while the shutter was open (Little et al., 1999). The exposure time of each "scanned" frame is 59.8 seconds. With an average of 12 large flashes per storm, we estimate approximately 5 seconds between the large flashes. Because this time is similar to the exposure time of Flashes 1, 2, 4, 5, and 6 (6.4 seconds), each of these images shows either one or very few flashes. The single maximum and smooth brightness falloffs in the data suggest that even if we see multiple flashes, they probably happened approximately in the same location.

Fig. 3.1 shows Flash 1 data. The raw image of the same flash is shown in Fig. 9a in Little et al. (1999). In Fig. 3.1 the background is subtracted. The background in the raw image increases from the lower left to the upper right corner. To remove this effect, we subtracted the linear background $b = C_0 + C_x X + C_y Y$, where X and Y are the column and the row of the pixel respectively, and C_0, C_x and C_y are the best fit coefficients to the background. The background was sampled in the 2-pixel-wide frame around the image (not shown in Fig. 3.1). For Flashes 2 through 6 we cannot calculate the linear background function either because there were adjacent flashes or because the variation of the background across the flash was small. In these cases, we subtract a single background number, C_0, for the whole image.

The azimuthal distribution of brightness in Flash 1 is unusual. The image is taken at an emission angle of 55.7°. If the lightning spot were azimuthally symmetric in the horizontal plane, the isophotes would look elliptical in the image plane because of foreshortening. The black ellipses in Fig. 3.1 show how the horizontal circles centered at the flash would look from the spacecraft. As was noted in Little et al. (1999), the observed isophotes (grey ellipses in Fig. 3.1) do not correspond to the horizontal circles. Instead, the brightness distribution is bulged along the short axis of the ellipses. The short axis lies along the projection of the line of sight of the

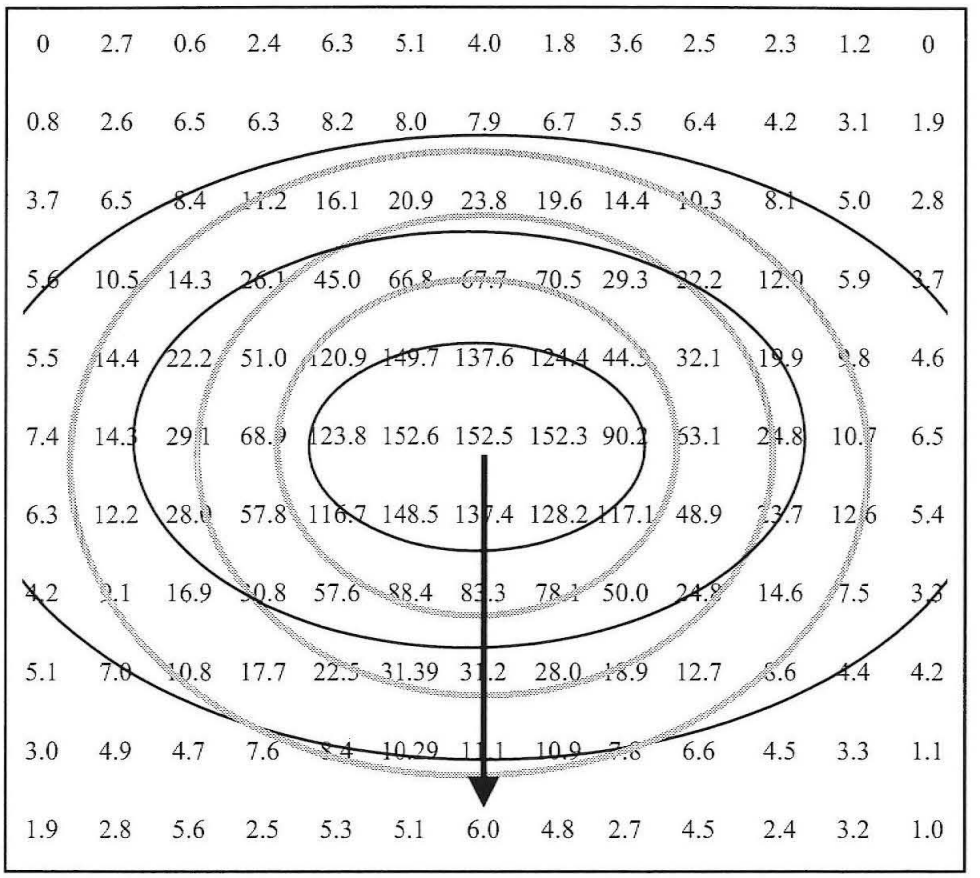

Figure 3.1: Flash 1 unprojected data numbers (DN) for the image pixels. The figure is an analog of Fig. 9 from Little et al. (1999), but in our case the background is subtracted. The projected circles on Jupiter's surface are shown by black ellipses exactly as in Fig. 9 of Little et al. (1999). The grey ellipses approximately show the isophotes at DN = 65, DN = 25, and DN = 10.

spacecraft (black arrow in Fig.3.1) which is also the projection of the local vertical. This effect is observed in five out of the six flashes. Little et al. (1999) discuss several possible explanations: vertical orientation of the flash, the way in which the photons are scattered in the clouds, and effects of the spacecraft's oblique line of sight. We test these possibilities in our model and find that a 3D geometry of the clouds is a better explanation as will be discussed in Section 3.4.1.

We use brightness falloff plots to compare the model and the data. The advantage of using these plots is twofold. First, the shape of the brightness falloff can be fit. Second, the azimuthal asymmetry can be shown by greyscale coding. The brightness falloff plot for Flash 1 is shown in Fig. 3.2. The brightness is normalized by the brightest pixel, and each filled circle corresponds to one pixel. The greyscale represents the azimuthal angle when the image is projected onto the horizontal plane. The light grey pixels along the line of sight of the spacecraft are brighter than the averaged curve with open circles. The black pixels in the perpendicular direction are fainter. This demonstrates the azimuthal asymmetry discussed above.

The images and brightness falloff plots for Flashes 2 to 6 are shown in Fig. 3.3. The spread of the data points is large in all these flashes (except Flash 5). Because of that, the brightness falloff shape is uncertain and we do not model the shape. However, the half width at half maximum (HWHM) in these flashes can be determined fairly well, and we do use it for the lightning depth calculations. All of the flashes except Flash 5 show azimuthal asymmetry similar to that in Flash 1. Flash 5 has a well-determined brightness falloff shape, which we model, and no azimuthal asymmetry.

The images of the 6 flashes do not show a single bright pixel or a row of bright pixels. Therefore the lightning bolts are not observed directly. Instead, we most likely see the diffuse spots of light scattered within the optically thick clouds. However, our choice of flashes may be biased toward these types of spots. This is because a directly observed lightning bolt would produce a bright pixel or a line of pixels on top of a

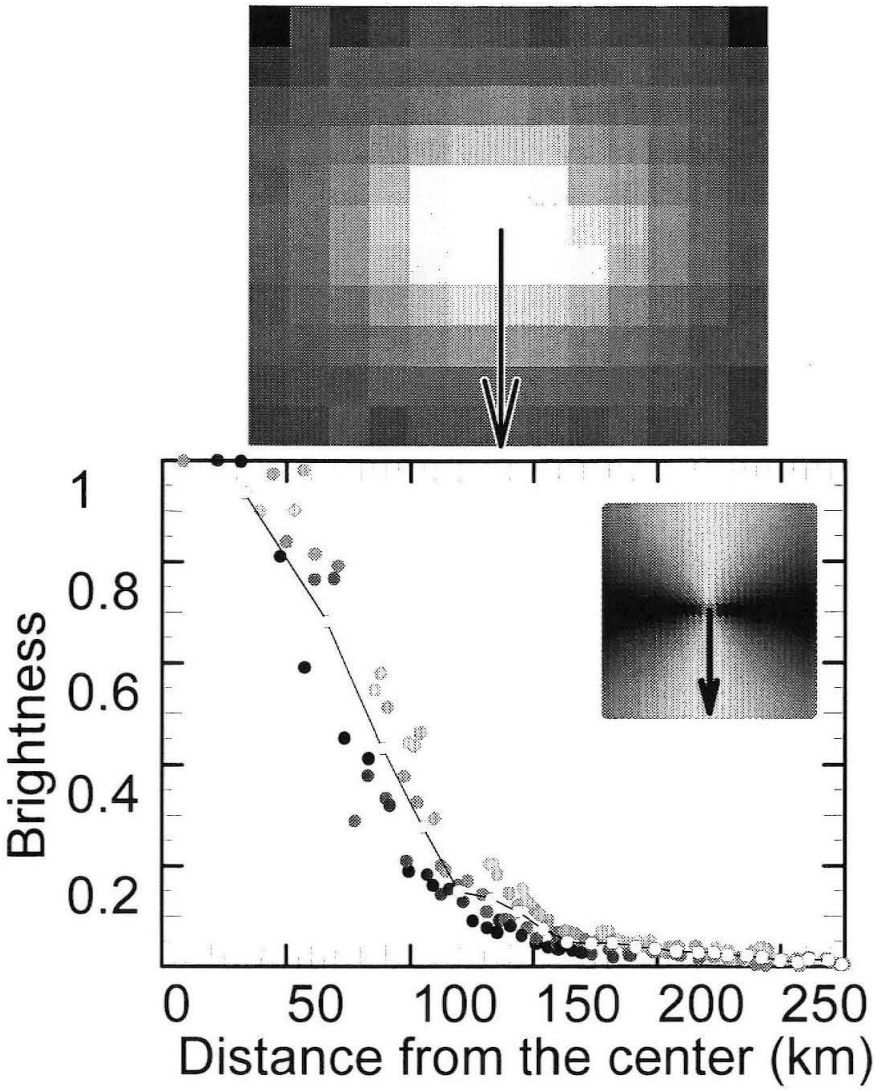

Figure 3.2: Top: the image of Flash 1. The black arrow points from the brightness-weighted center of the flash toward the spacecraft and shows the direction of the line of sight. Bottom: brightness falloff plot for Flash 1. Filled circles show the brightness of each pixel. The greyscale shows the azimuthal angle relative to the line of sight as shown in the greyscale chart in the top right corner of the bottom plot. The chart corresponds to the image above, and is centered at the center of the flash. The arrow on the chart points toward the spacecraft. The curve with open circles is the average of the greyscale circles taken in small intervals of distance from the brightness center.

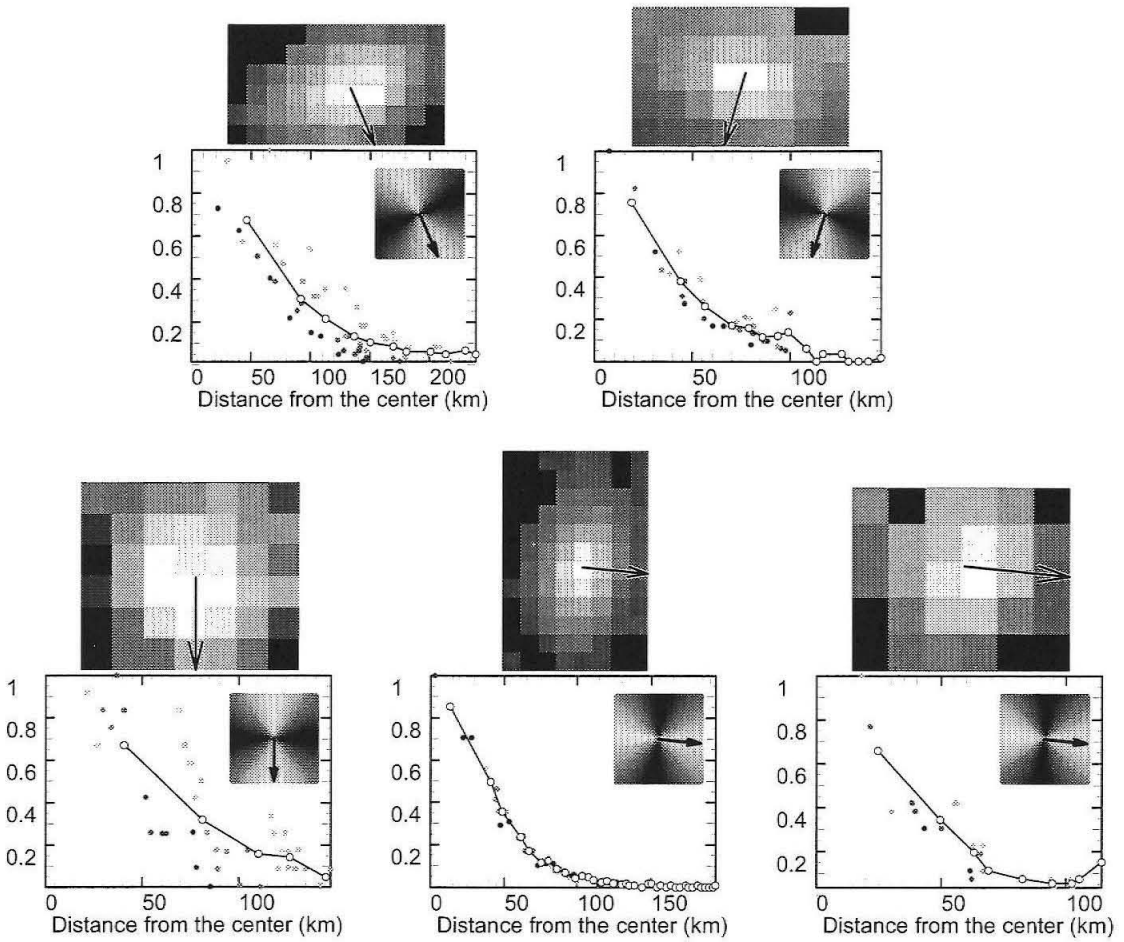

Figure 3.3: The images and brightness falloff plots for flashes 2 (top left), 3 (top right), 4 (bottom left), 5 (bottom middle), and 6 (bottom right) shown the same way as Flash 1 in Fig. 3.2. Note that the brightness-weighted center of the flash is not necessarily inside the brightest pixel.

relatively faint diffuse spot of illuminated clouds. In this case the resulting image in the Galileo camera would either be saturated at the bright pixels or would show only a few bright pixels with no low-signal scattered light. Some of the Galileo flashes are saturated such that the maximum in the brightness distribution is cut off and we cannot study them. Some of the Galileo flashes appear as a few bright pixels, but in this case they are indistinguishable from cosmic rays hitting the detector and cannot be clearly identified as lightning.

3.3 Model

Our model simulates the scattering of point-sized lightning-produced photons in a 3D cloud. The lightning is modeled as a point or a vertical line, but not as a horizontal line because of the following reasons. The brightness falloff in the data images is smooth and the brightest pixels do not follow lines or curves. The exception is the azimuthal asymmetry along the line of sight visible in several images. It is unlikely that this is the result of the horizontal elongation of the lightning because it would stretch the flashes in a random direction. Although the sample size is small, the observed asymmetry shows up in one preferred direction — the line of sight. The azimuthal asymmetry may be due to the vertical elongation of lightning. This can possibly make the lightning spot stretch along the line of sight regardless of the observational azimuth. Accordingly, only vertical and not horizontal linear lightning was modeled. Photons are created with constant probability along this line and the directions of the new photons are random.

After a photon is created at the lightning it flies some distance within the clouds with some probability of scattering. The clouds are defined by an opacity distribution which prescribes the scattering probability per unit length. The clouds are confined within a cylindrical volume. To model plane-parallel clouds we choose the horizontal

size of the cylinder to be large, such that the edge effects are small. Different plane-parallel opacity distributions as well as several simple 3D opacity distributions were tested and will be discussed in Section 3.4.

The trajectory of the photon is defined as a sequence of linear steps between scatterings. During each step the path that the photon travels is defined in the following way. First, we randomly choose the optical depth ($-ln(R)$, where R is a random number between 0 and 1) to which the photon is going to penetrate. Then, the path length is calculated from the optical depth by the integration of the opacity distribution along the photon's direction. Lower opacities give larger pathlengths and visa versa.

At each scattering, the new location and direction of the photon is calculated. The direction is chosen randomly with a probability defined by the scattering phase function, which gives the differential scattering probability as a function of scattering angle. In practice it is necessary to invert this relation, which we did numerically. We used the two-term Henyey-Greenstein scattering phase function derived by Tomasko et al. (1978) from the Pioneer 10 images, as will be discussed in Section 3.4.2.

To account for absorption, each photon is assigned an intensity. New photons have unit intensity. During each scattering the intensity is multiplied by the single scattering albedo. The single scattering albedo is set to be 0.996, which is the average of the blue (0.44 μm) and red (0.64 μm) albedos from Tomasko et al. (1978).

Images at different azimuths and emission angles are obtained by collecting photons emerging from the cloud in $10^\circ \times 10^\circ$ bins. Every photon in the right emission angle bin contributes its intensity to the brightness of one of the image pixels. The location of the pixel is calculated using the point of the photon's last scattering. This point is projected to the image plane, which is perpendicular to the cloud – observer direction. Because only the azimuthally symmetric clouds are studied, the images at different azimuthal angles are added together to construct an average image at each

emission angle.

The resolution of the images produced in the model is 100×100 pixels — 3 or more times finer than the resolution in the Galileo data. To reproduce the resolution of the data, the modeled screens are resampled. The coarse grid corresponding to the data is obtained by averaging several pixels of the model using an ensemble of positions for the coarse grid. In the modeled images the columns of pixels are aligned with the line of sight. For most of the data images (Flashes 2, 3, 5, and 6) the columns are not aligned with the line of sight. Accordingly, the coarse grid is rotated relative to the fine grid of the modeled images.

The depth of the lightning below the cloud tops in units of fine grid pixels is prescribed by the model. The pixel size of the coarse grid is chosen to match the HWHM of each flash in the data. Accordingly, the lightning depth is known in terms of the coarse grid pixels, and therefore in kilometers.

3.4 Results

3.4.1 3D Clouds

Our first hypothesis was that the clouds are plane-parallel. However, the brightness falloff in Flash 1 cannot be reproduced by the plane-parallel cloud model. The azimuthal asymmetry, which is present in most of the flashes, is also not reproduced by the plane-parallel cloud model. Figure 3.4 shows typical brightness falloff for the plane-parallel cloud model (filled circles) compared to the Flash 1 averaged data (open circles). The shape of the modeled falloff does not follow the data. The azimuthal asymmetry is not reproduced — the grey pixels along the line of sight are not brighter than the black pixels in the horizontal direction. Instead, the spread of the brightness

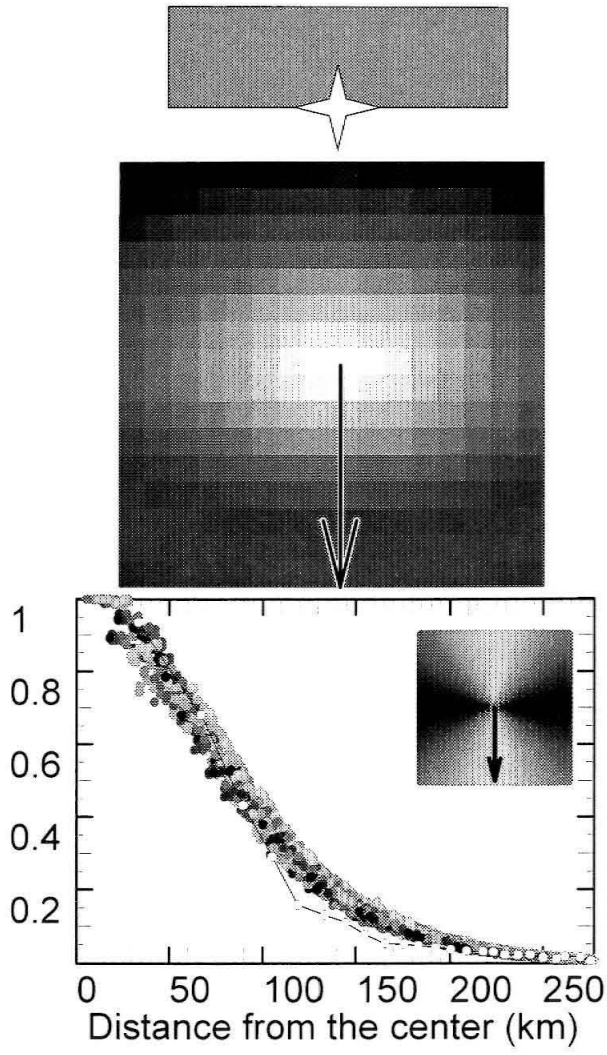

Figure 3.4: Model results for the plane-parallel cloud compared to Flash 1 data. Top: Cross section of the cloud. The opacity is distributed homogeneously in the cloud layer. The optical depth of the cloud along the vertical is 10. The point lightning at the bottom of the cloud is marked by the star symbol. Middle: The modeled image in the coarse grid corresponding to Flash 1. Bottom: The brightness falloff in the modeled image (greyscale circles) compared with the averaged data from Flash 1 (the curve with the open circles shown in Fig. 3.2). The brightness distributions are scaled by the brightest pixel. The horizontal scale in the model is chosen to match the HWHM of the Flash 1 data.

is random with respect to the azimuth.

We studied different plane-parallel clouds to see if we could reproduce the brightness distribution and azimuthal asymmetry of Flash 1. We considered different vertical opacity profiles: increasing opacity with height, decreasing opacity with height, linear and exponential rates of decrease (increase), and multiple layers of clouds. The range of single scattering albedos and the scattering phase functions was studied. The effect of Rayleigh scattering atmosphere beneath the clouds was tested. We also tested different lightning geometries. The point-like or linear lightning was placed in the middle, at the bottom, and below the cloud. Different lengths of vertical lightning were tested. For this wide range of variations the shape of the brightness distribution remained similar to the one shown in Fig 3.4 (greyscale points on the plot). The vertical lightning could not reproduce the effect of azimuthal asymmetry. In the modeled images it either is seen directly as a line of bright pixels or produced an azimuthally symmetric spot.

By contrast, a simple 3D cloud model can reproduce both the brightness falloff shape and the azimuthal asymmetry seen in Flash 1. Fig. 3.5 shows the brightness falloff for a hemispheric cloud model (filled circles) compared with the averaged Flash 1 data (open circles). Fig. 3.5 shows an example of the 3D models that fit the data. The haze opacity is restricted to be about 1-2 to fit the outer skirt of light at a brightness of less than 0.3 of the maximum. Variations of the opacity distribution within the hemisphere produce fits that are as good as that in Fig. 3.5. For example, increasing the opacity of the hemisphere gives the same brightness falloff shape. However, other shapes of the cloud, such as a cylinder or anvil shape (common for Earth thunderstorms) do not fit the data as well.

Of course this does not mean that the cloud has to be a perfect hemisphere. Uncertainties, even in the well resolved Flash 1 image, do not allow us to make a firm conclusion about the exact shape. However, our results do suggest a 3D rather than

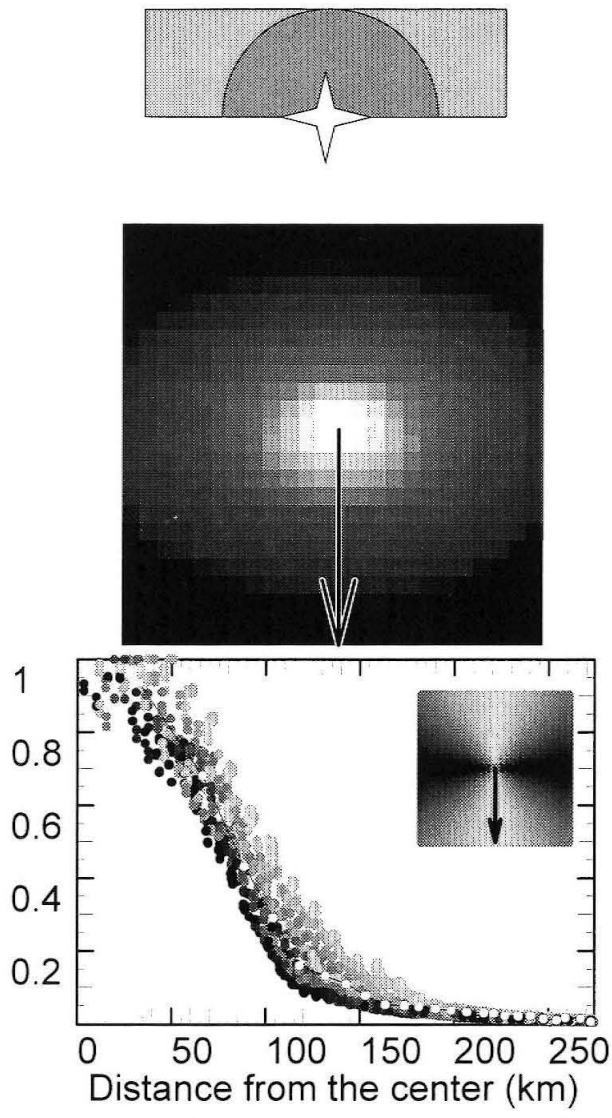

Figure 3.5: Model results for the hemispheric cloud within an optically thin haze compared to Flash 1 data. Top: Cross section of the cloud. The opacity is distributed homogeneously in a hemisphere of optical depth 10 along the vertical. The hemisphere is surrounded by a homogeneous plane-parallel haze of optical depth 1. The point lightning is at the bottom of the cloud, in the center of the hemisphere. Middle: The modeled image. Bottom: The brightness falloff plot in the modeled image (greyscale circles) compared with the averaged data from Flash 1 (the curve with the open circles shown in Fig. 3.2).

plane-parallel cloud geometry.

Another well-resolved brightness distribution is seen in Flash 5. Unlike all other flashes it shows no azimuthal asymmetry. The shape of the falloff is best fit by the plane-parallel cloud model (see Fig. 3.6).

The brightness falloff shapes in flashes 2, 3, 4, and 6 (Fig. 3.3) are too uncertain to determine if they are produced in 3D or plane-parallel clouds. However these flashes show the same azimuthal asymmetry as in Flash 1, suggesting a 3D cloud geometry.

3.4.2 Lightning Depth

We find the depth of the lightning below the cloud tops by scaling the model geometry to match the HWHM of the data images.

Figure 3.7 shows how the HWHM's of the modeled images vary depending on the phase function, single scattering albedo, cloud geometry, and presence of Rayleigh-scattering atmosphere below the cloud. The ordinate shows the ratio of the model-derived lightning depth to HWHM. The hemispheric + haze geometry (open diamonds) provides a good fit for Flash 1. The plane-parallel geometry (all other curves) provides a good fit for Flash 5. Both geometries give acceptable fits for Flashes 2, 3, 4, and 6.

In our calculations we assume strong forward scattering, which is typical for upper tropospheric clouds. This is described by the two-term Henyey-Greenstein function.

$$P(g_1, g_2, f, \theta) = f P_{HG}(g_1, \theta) + (1 - f) P_{HG}(g_2, \theta)$$

The two terms are the two single-term Henyey-Greenstein functions representing for-

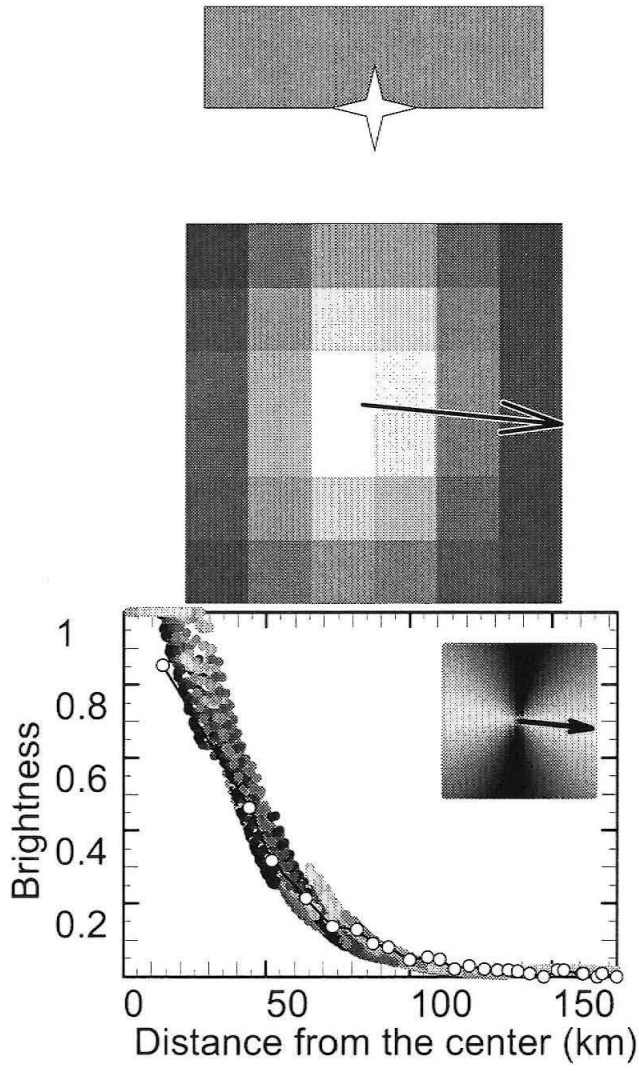

Figure 3.6: Model results for the plane-parallel cloud compared to Flash 5 data (see caption for Fig. 3.4).

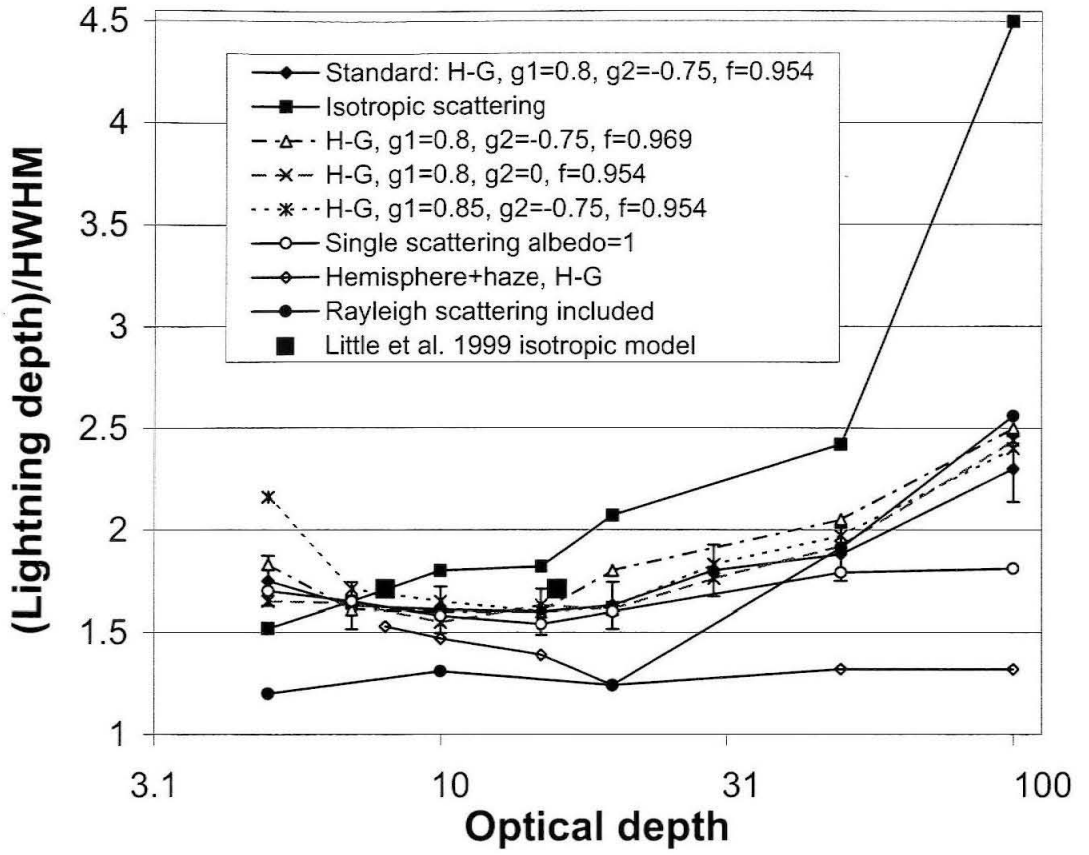

Figure 3.7: Ratio of cloud layer depth to HWHM of the spot at emission angle 55.7°for different phase functions for the plane-parallel cloud (upper five curves), plane-parallel cloud with the standard phase function and single scattering albedo one, hemispheric cloud within haze with the point-like lightning at the cloud base, and standard plane-parallel cloud with a Rayleigh-scattering atmosphere beneath. The two large filled squares show the model results of Little et al. (1999). The error bars shown for the standard model are similar for all curves and are due to the pixel sampling uncertainty.

ward and backward scattering lobes.

$$P_{HG}(g,\theta) = \frac{(1-g^2)}{(1+g^2-2g\cdot cos\theta)^{3/2}}$$

θ is the scattering angle, f is the fraction of the forward versus backward scattering, g_1 is positive and shows the sharpness of the forward scattering lobe, g_2 is negative and shows the sharpness of the backscattering lobe. The parameters g_1, g_2 and f are derived by Tomasko et al. (1978) from the Pioneer 10 images. We use g_1=0.8, g_2=-0.75, f=0.954, which are the average for the blue (0.44 μm) and red (0.64 μm) filter values for the tropospheric clouds in South Tropical Zone and call that a standard phase function. Figure 3.8 shows the shapes of the Henyey-Greenstein function for the standard case (solid line) and for variations in the Henyey-Greenstein parameters g_1, g_2 and f. The value f=0.969 (dot-dashed curve) is the highest in the range determined by Tomasko et al. (1978). We only show the extreme case of g_2=0 (dashed curve) because realistic variations in the backscattering parameter g_2 have a very small effect. The forward scattering parameter g_1 has a strong effect, but unfortunately values larger than 0.75 cannot be distinguished in the Pioneer data (Tomasko et al., 1978) and we choose g_1=0.85 (dotted curve) arbitrarily to demonstrate the effect of forward scattering. Analysis of new Cassini observations may help. Also one must be cautious about the applicability of the Pioneer scattering function because the Pioneer spacecrafts sampled only the upper clouds. Accordingly, only single scattering was considered by Tomasko et al. (1978) to determine the scattering properties. Our data sample much deeper clouds where the scattering properties are not as well known and may be quite different.

As can be seen in Fig. 3.7, the modeled spot size decreases at large optical depths resulting in large calculated lightning depths (large depth/HWHM ratio). The exception is the hemispheric + haze cloud (solid curve with open diamonds), where

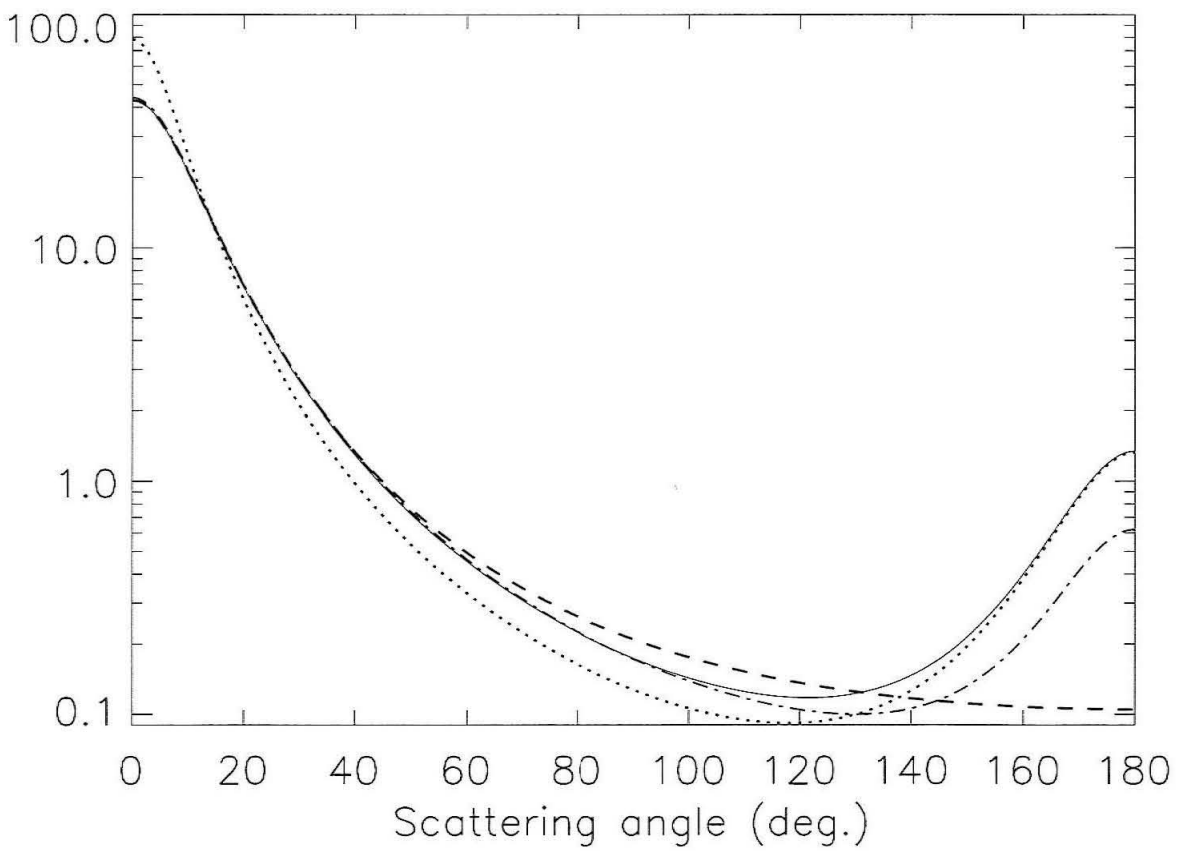

Figure 3.8: Henyey-Greenstein functions used in calculations for Fig. 3.7. The linestyles correspond to the linestyles in Fig. 3.7.

the spot size approaches the cloud diameter as the optical depth increases. The hemispheric + haze geometry results in larger spots and therefore shallower lightning depths than for the plane-parallel case. Higher single scattering albedo decreases the derived lightning depths (solid curve with open circles).

Another curve (with closed circles) demonstrates the Rayleigh scattering test. Rayleigh scattering from the atmosphere below the clouds (5–20 bars) may be important if the atmospheric absorption is small, which is not well known. Laboratory experiments by Borucki et al. (1996) suggest that most of the lightning energy within the span of the Galileo clear filter is expected to be emitted around H_α (650–680 nm) and H_β (480–500 nm) bands. Optical depth one for Rayleigh scattering is reached at about 20 bars at H_α wavelengths and at about 7 bars at H_β wavelengths. The main atmospheric absorber in these wavelengths is methane (Karkoschka, 1994). In the upper troposphere the methane absorption is small when integrated over the wavelength. At 5–20 bars, pressure and temperature may enhance the absorption such that the atmosphere beneath the clouds would be effectively black as it was assumed in our standard model. However, the absorption may be small. For example, Banfield et al. (1998) estimate a lower limit for atmospheric absorption at continuum wavelength (756 nm) and obtain optical depth of 0.01 bar^{-1}. For a two-way path down to 20 bars it will give the optical depth of 0.4, and a substantial fraction of light may return from the Rayleigh scattering layers. To test the H_α and H_β cases we put a non-absorbing Rayleigh scattering atmosphere below the standard cloud (which has a base at 7 bars) such that the Rayleigh-scattering opacity is proportional to the air density and reaches optical depth one at 20 and 7 bars for H_α and H_β wavelengths respectively. As expected, Rayleigh scattering produced larger effect at shorter wavelengths around H_β band, and the curve in Fig. 3.7 corresponds to this case. Note that the abscissa for this curve shows the optical depth of the cloud but not the atmosphere. The resulting lightning depths are quite shallow for low cloud

optical depths.

The depth/HWHM derived in a preliminary Monte Carlo model by Little et al. (1999) is shown as two large filled squares. This preliminary model counted photons emerging from the cloud in all directions. Our model counts photons at a particular emission angle (55.7 °), which is probably the reason for the small discrepancy between the results of Little et al. (1999) and our analogous results for isotropic scattering in the plane-parallel layer (solid curve with filled squares). Note that the values of the ratio of lightning depth to HWHM in Little et al. (1999) were calculated assuming the level of optical depth one as the effective cloud tops. In Fig. 3.7 we use the distance to the top of the homogeneous cloud layer. We convert the results of Little et al. (1999) to the Fig. 3.7 scale, which gives the depth to HWHM ratio of 1.7 instead of 1.5 at optical depth 8 and 1.7 instead of 1.6 at optical depth 16.

Fig. 3.9 shows the pixel size effect. This test was done by resampling 100×100 pixel screens (assumed to have "actual HWHM") with coarser grids. Rotation of the resampling grid gives a very similar distribution and thus we do not show it here. It can be seen that the spots with HWHM $>$ 3-4 pixels (15-20 pixels across the entire distribution) are not strongly distorted by resampling. For the smaller spots the HWHM should be corrected. We consider the 100×100 grid undistorted because the corresponding HWHM's obtained in the model are much larger than 4 pixels. We resample modeled images by the coarse grid corresponding to every data image to correct for the pixel size effects.

Another source of uncertainty is the location of the coarse grid relative to the lightning spot. We estimate the error by sampling 100×100 pixel modeled images by a grid 4 times coarser, which is typical for our data. The uncertainty of about ± 5-10% of the HWHM is produced by shifting the coarse resolution grid relative to the fine grid.

As seen from the analysis above, there is a range of models that provide acceptable

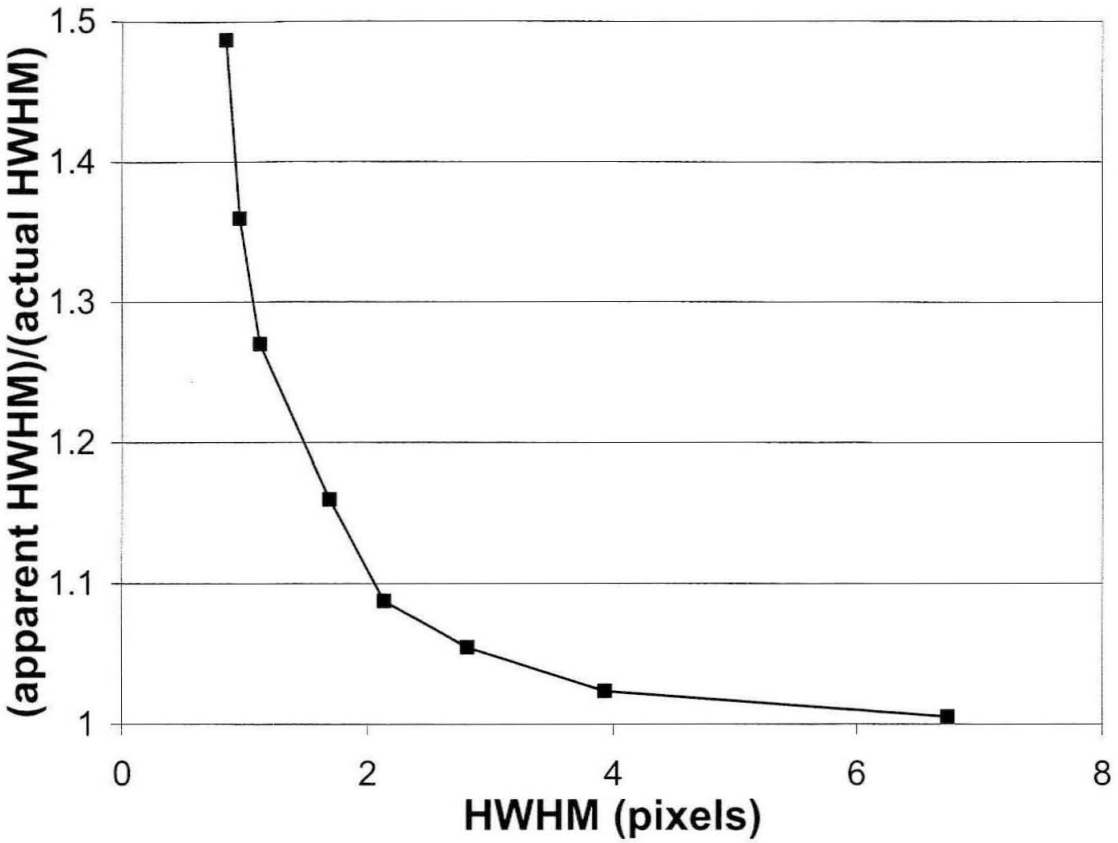

Figure 3.9: Increase in the apparent HWHM of the lightning spot due to pixel size.

fits to the shape of the brightness falloffs. The depths derived from these models differ (see Table 3.2), resulting in the depth uncertainty of more than ± 20-30%.

Flash	HWHM (km)	Emission angle	Lightning depth (km)	Depth /HWHM	Acceptable models
1	87	55.7°	95-140	1.1-1.6	3D clouds
2	69	69.1°	68-158	1-2.3	Plane-parallel or 3D clouds
3	37	56.6°	35-79	0.9-2.1	Plane-parallel or 3D clouds
4	72	57.0°	74-171	1-2.4	Plane-parallel or 3D clouds
5	42	50.6°	47-90	1.1-2.1	Plane-parallel clouds
6	50	50.6°	52-110	1-2.2	Plane-parallel or 3D clouds

Table 3.2: The depth of the lightning below the cloud tops for different flashes

It is important to note that lightning having horizontal extent up to one pixel (25 km) is unresolved and therefore is treated as a point source. However, the lightning spot would be larger (the HWHM would be 12–15 km. larger), and the lightning would appear deeper than in the case of point lightning. Accordingly, the smallest values of lightning depths in the Table 3.2 may be overestimated by about 12–15 km.

To estimate the pressure corresponding to the lightning at these depths, we need to estimate the location of the cloud tops. To do that we summarize results of other researchers, which are sometimes controversial as discussed by West et al. (1986) and Sromovsky and Fry (2001). The cloud tops are assumed to be below or near the tropopause, which prevents the upward spread of the convective clouds. The Galileo probe found the tropopause at 0.26 bars (Seiff et al., 1998). Another upper limit for the cloud tops is found by radiative transfer modeling (Banfield et al., 1998), according to which a cloud optical depth of 1 is reached at a physical depth below 0.2 bars. The lower limit for the cloud tops is probably the main NH_3 cloud deck, which is located at about 0.6–0.8 bars (West et al., 1986; Banfield et al., 1998). Accordingly, we assume that the cloud tops may be located between 0.2 and 0.6 bars.

Fig. 3.10 shows the altitude-pressure dependence measured by the Galileo probe (Seiff et al., 1998). The locations of the cloud bases correspond to the equilibrium condensation model by Weidenschilling and Lewis (1973), and depend on the abundance of the corresponding species. The location of the cloud tops is very uncertain and varies with local meteorology. The presence and location of NH_4SH cloud is questionable because of the uncertainties in H_2S abundance (West et al., 1986). The two water cloud base levels in Fig. 3.10 are calculated by Niemann et al. (1998) for the Galileo probe pressures and temperatures assuming solar and 2 times solar O/H mixing ratios. The probe detected a much smaller O/H mixing ratio, 0.033 ± 0.015 solar at 8.7-11.7 bars (Niemann et al., 1998). However, the probe entered Jupiter's "desert," a Hot Spot region known for its extreme dryness. Galileo NIMS imaging at around 5 μm suggests moist regions of 2 times solar O/H in close proximity to the very dry Hot Spot (Roos-Serote et al., 2000). Therefore, the location of the water cloud base in Fig. 3.10 is realistic.

From Fig. 3.10 and Table 3.2 one can see that Flash 1 is unusually deep, probably below the expected water cloud base. The other flashes may also be deep, or, if the shallowest possible depth is considered, they may be as high as 2 bars, which is approximately the location of the NH_4SH cloud or, if the convection brings water to these heights, the water cloud.

The large depths in Table 3.2 also suggest that the cloud tops above large lightning must be high. This is an evidence for deep convection, penetrating all the way from the water cloud base to the tropopause.

3.4.3 Optical Depth of the Clouds

As we mentioned in Section 3.2, instead of direct light from lightning, the data show diffuse scattered light. Therefore, clouds above the lightning must be opaque enough

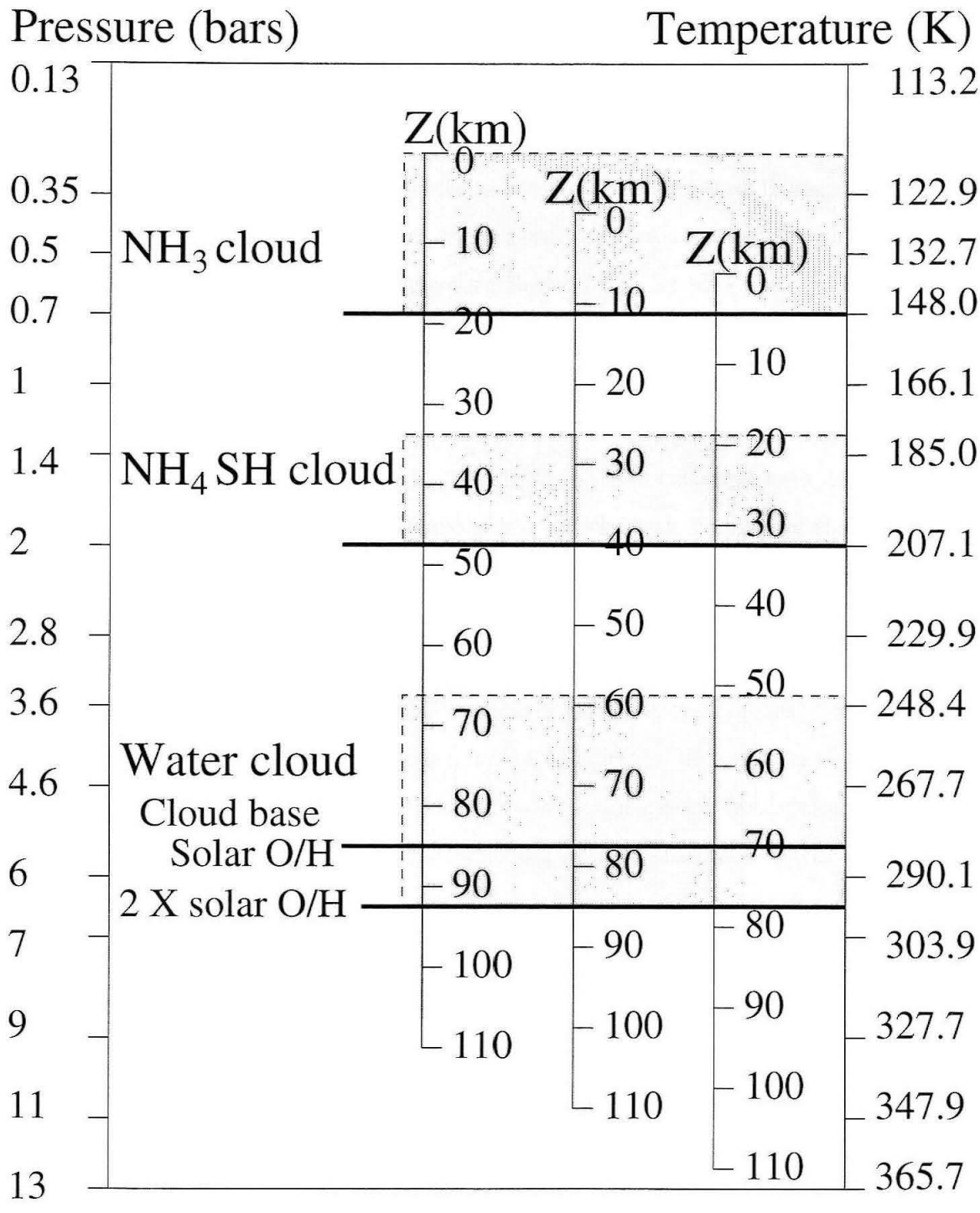

Figure 3.10: Pressures corresponding to the depth Z below the cloud tops. The three Z scale bars show the dependence for the cloud tops located at 0.2, 0.4, and 0.6 bars.

to block the direct light. Our model results show that only the clouds with optical depth more than 5 can block the direct light and produce smooth brightness distribution. Less opaque clouds produce a single bright pixel with a surrounding very faint light skirt for point-like lightning, or for linear lightning, a line of bright pixels. Our choice of lightning spots might be biased toward cloud-covered lightning. Directly observed lightning may be confused with cosmic ray hits, or may be saturated and therefore not studied here as discussed in Section 3.2. It also may be too small to resolve the brightness falloff. However if directly observed lightning were common for Jupiter, we would probably find at least a few spots that had one bright pixel surrounded by a faint skirt of scattered light. No spots of this kind were found. This allows us to conclude that at least for the lightning spots studied here, and probably for typical jovian lightning, the opacity of the clouds must be greater than 5.

3.4.4 Energy of the Lightning

To estimate the total energy associated with lightning it is important to know what fraction of the emitted light is observed above the clouds. Our results show that this number is highly dependent on the poorly known atmospheric absorption at 5-20 bar level. Optically thick clouds above the lightning would reflect most of the energy back down. If the atmospheric absorption is strong, the atmosphere below the clouds can be considered black. If the absorption is weak, the Rayleigh scattering atmosphere will reflect most of the energy back up. Note that the Rayleigh scattering atmosphere is more effective in reflecting light compared to the clouds because of the symmetric Rayleigh phase function compared to the strong forward scattering phase function in the clouds. Knowing the optical depth of the cloud we estimate what fraction of the light is coming toward the spacecraft, *i. e.*, estimate the cloud transmission. Fig. 3.11 shows the cloud transmission at different optical depths for the plane-

parallel and hemispheric + haze cloud with point-size lightning at the cloud base for different scattering parameters and the black atmosphere beneath. The case of Rayleigh scattering non-absorbing atmosphere is shown by the solid curve with closed circles. The left side of each curve shows the minimum optical depth required to block the direct light from the lightning bolt.

For the case of the black atmosphere the transmissions are less than 0.5, showing that the cloud attenuation is at least a factor of two. Forward scattering results in small attenuation. The attenuation is much stronger in the case of isotropic scattering (solid curve with filled squares). If the atmospheric absorption at 5–20 bars is low (the curve for Rayleigh scattering in Fig. 3.11), the effective transmission at low optical depths is close to one, *i. e.*, the amount of light emitted at the cloud tops is nearly the same is if there were no clouds.

We estimate the attenuation by the clouds but not by the atmosphere (except for the assumption of black atmosphere below the clouds). Gaseous absorption enhances attenuation of the light and therefore reduces the amount of transmitted light. If the absorption does not increase strongly at the pressures where the clouds are located (up to 7-8 bars), the actual combined cloud and gas transmission is close to the upper limit, which we calculate here.

As can be seen in Fig. 3.11, realistic clouds may have a wide range of transmissions. In particular, the extreme case of unit transmission (no effective attenuation) is possible. This is important because the cloud transmission is crucial for the estimate of the lightning (and total thunderstorm) energy, and the unit transmission was assumed in the estimates of the Voyager 1 and 2 and Galileo lightning energies (Borucki et al., 1982; Borucki and Magalhães, 1992; Little et al., 1999).

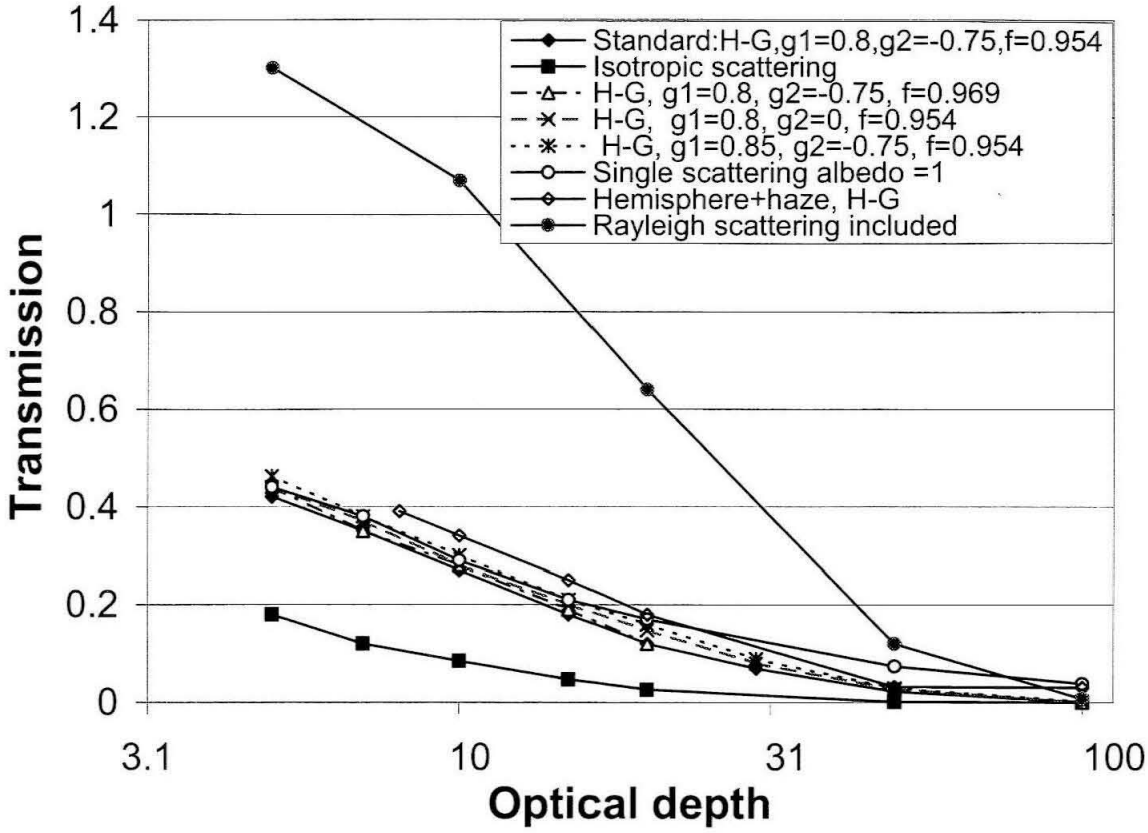

Figure 3.11: Cloud transmission at emission angle 55.7° for the hemispheric cloud within a haze layer of optical depth unity (curve with open diamonds), plane-parallel cloud layer with various scattering properties, and a standard cloud with Rayleigh scattering atmosphere beneath (curve with closed circles). The optical depth (abscissa) is calculated along the vertical directly above the lightning. The point lightning is at the base of the cloud. The light is normalized by the light that would come from the source without clouds, i. e., power of the source divided by 4π multiplied by the solid angle that collects photons.

3.5 Comparison with Terrestrial Lightning

At the same time Galileo was observing jovian lightning, the first systematic study of spatially-resolved terrestrial lightning flashes from space started with the launch in 1997 of the Lightning Imaging Sensor (LIS) (Christian et al., 2000). We believe that comparison of the two observations is essential for understanding lightning on both planets and devote this section to the short comparison of the LIS and Galileo results. This short study covers only a few days out of the four-year span of the LIS observations and does not attempt to do accurate statistics as done by the LIS team (Boccippio et al., 2000). However, these few days represent hundreds of individual flashes and give us a reasonably good estimate of what the typical terrestrial lightning flash looks like from space.

Fig. 3.12 shows an example of the flashes recorded above South Africa. The size and shape of these flashes are typical for other locations within LIS field of view (from equator to ±35 degrees latitude). The flash image in each box is produced by accumulating intensity of the 2 ms LIS frames during about 0.5-second-long single flash (Dennis Boccippio, private communications). This simulates the jovian lightning images, which had 6.4 second exposures and probably captured single flashes. Only large LIS flashes were considered because the small ones would not be spatially resolved with the 3–6 km/pixel LIS resolution.

The first obvious lesson from the LIS images is that for the largest flashes the shape of the lightning spot is defined by the shape of the lightning bolts extending tens of kilometers horizontally. The shapes are irregular and randomly oriented relative to the line of sight (shown by the arrows in Fig. 3.12). If large horizontal flashes occurred on Jupiter, Galileo would resolve the irregular shapes of these single-maximum flashes. However, all single-maximum flashes seen by Galileo have nearly elliptical shapes and are not randomly oriented. Instead they are either stretched along the line of sight

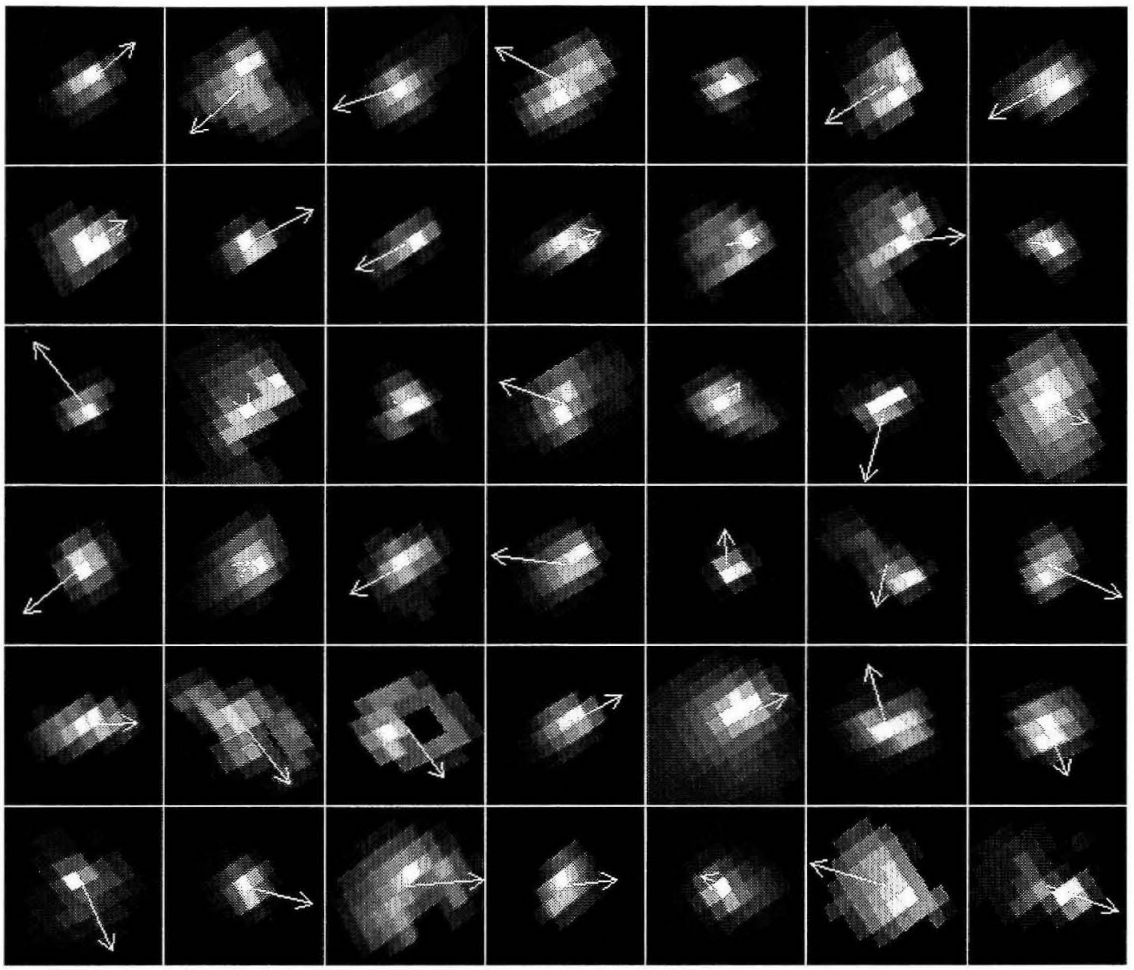

Figure 3.12: Individual terrestrial flashes observed by LIS over South Africa (orbit TRMM_LIS_SC.04.0_1998.062.01512). Flash in each box is map-projected to the latitudinal-longitudinal grid. The size of each box is 50×50 km. The arrows point toward the spacecraft. The length of the arrows shows the emission angle, i.e., long arrows indicate large emission angles up to 53°, short arrows indicate that the flash is observed directly behind the spacecraft (emission angle 0°).

or circular (Flash 5). Therefore lightning spots observed by Galileo are not similar to the largest terrestrial flashes. However, because horizontal lightning is so common for Earth, it is expected that lightning on Jupiter may have at least some horizontal extent, which is unresolved by the 25-km-wide Galileo pixels. The horizontal extent of lightning would make the spot appear larger and the derived lightning deeper, as discussed in Section 3.4.2.

The second lesson from the LIS images is that there are also small diffuse lightning spots, which are the result of small lightning bolts. The appearance of these spots is largely due to light scattering within the clouds. These diffuse spots are poorly resolved — only few LIS pixels across. The typical HWHM's are 5–8 km (which should be treated with caution at 3–6 km/pixel resolution). These are reasonable values in terms of our scattering model because of the following: The elevation of the cloud tops is about 12–16 km above sea level. The upper end of lightning bolts in the tropics is usually located at a height where the temperature is about -5 – -40°C (Uman, 1987), or about 4–10 km above sea level. Thus, assuming lower cloud tops when the lightning is lower, lightning is approximately 5–10 km below the cloud tops. Our model predicts that the ratio of the lightning depth below the cloud tops to the HWHM is 1–1.6. The 5–10 km of cloud above lightning then would result in a spot with HWHM of 5–16 km, consistent with 5–8 km observed by LIS.

3.6 Discussion

It is not surprising to see 3D clouds around lightning. Lightning on Jupiter is known to be correlated with small-scale bright clouds, which we will call storm clouds. This correlation is seen in the images from Voyager 2 (Borucki and Magalhães, 1992), Galileo (Little et al., 1999; Gierasch et al., 2000), and Cassini (Porco *et al.*, in preparation). The storm clouds have roots at the depth of a few bars (Banfield et al.,

1998). They are associated with local enhancements in water abundance as seen in Galileo near IR spectra (Roos-Serote et al., 2000), which suggests that their origin is within the water cloud. We find that the cloud tops are unusually high above some of the lightning flashes. This suggests strong convection capable of bringing water ice particles to the uppermost cloud where they are observable. Indeed, the water ice signature in the small regions covering about 1% of Jupiter is seen in Voyager IRIS 44 μm spectra (Simon-Miller et al., 2000). Convective clouds can carry large amounts of water upward, which would produce large water ice particles. Galileo near IR imaging suggests that the cloud particles near storm clouds may be unusually large (Dyudina et al., 2001). Radiative transfer modeling of detailed Galileo NIMS spectra (Irwin and Dyudina, 2001) predicts larger particles near the storm clouds suggesting that the convection there is strong and local.

The typical size of the storm clouds is approximately 500–2000 km, which is large compared to the ~100-km-size hemispheric clouds found in this study. The storm clouds look patchy (Banfield et al., 1998) suggesting that convection is probably producing the 100-km-scale clouds as well. Small-scale (approximately 60 km. in horizontal) clouds are also predicted from the 3D dynamical model of convective cloud (Hueso and Sánches-Lavega, 2001). Our results suggest that the vertical size of these smaller clouds is similar to their horizontal size and therefore the plane - parallel approach is no longer valid for modeling the storm clouds.

The evidence of a plane-parallel cloud above Flash 5 is especially interesting because the lightning flash is located in the belt region, where one would expect to see 3D clouds. The belts are the regions of very low cloud opacity on average. The only optically thick clouds that may exist at high elevations are small convective clouds produced by storms. As the corresponding dayside image shows (Fig. 1 of Gierasch et al. (2000)), Flash 5 is located at the edge of a big storm. A possible explanation of why Flash 5 looks plane-parallel is that in such a location the upper cloud may be

the edge of a storm cloud anvil. The tops of the lightning-producing cloud itself may not reach a high elevation. As a result, the appearance of the flash would be defined by the high plane-parallel anvil edge but not the convective cloud itself.

A similar Monte Carlo modeling of Voyager 1 lightning images is done by Borucki and Williams (1986). Although the lower resolution of Voyager 1 data did not allow the study of brightness distribution in detail, the lightning depth was estimated from the spot size. Borucki and Williams (1986) conclude that lightning occurs in the water cloud at depths of about 5 bars. We find that the lightning may be deeper, maybe below the expected water cloud base. This result agrees with preliminary estimates from Galileo images given by Little et al. (1999), who run a simpler Monte Carlo model for few plane-parallel cases and derive lightning depths up to 120 km. We can make that conclusion mainly because Galileo observed larger lightning spots (the HWHM's are up to 87 km compared to the 57$\pm$ 7 km in Voyager 1 images). Such large lightning depth may suggest that the cloud itself exists at unexpected depths, implying a deep water abundance on Jupiter larger than 2 times solar and therefore a lower cloud base. Alternatively, very heavy rain may carry the charge below the cloud base, producing lightning in the clear air below the cloud. Another possibility is that the rain enhances the local water abundance below the storm cloud, lowering the cloud base. This effect would be more prominent where convection is more energetic. Energy flux from the jovian interior to the upper atmosphere increases toward higher latitudes, suggesting stronger convection (Ingersoll, 1976). It is interesting to note that our largest (and deepest) flashes (1, 2 and 3) are located at high latitudes (47.5, 48.5 and 56.1 °N respectively) which may be the result of larger energy fluxes and more energetic convection there. Two of these latitudes are close to 49 °N, where an unusually high frequency of lightning flashes was observed (Borucki and Magalhães, 1992; Little et al., 1999).

Deep lightning derived here has an important implication for the lightning-produced

trace species such as CO, HCN, and C_2H_2 (Bar-Nun and Podolak, 1985). The deep lightning at the water cloud base would likely give chemical production rates that are quite different from the ones for the lightning at the top or above the water cloud considered by Bar-Nun and Podolak (1985).

Appendix A Appendix: Monte Carlo Light Scattering Model

Two important remarks on notation must be made before the model description.

The overbar over a variable notifies the vector, e.g., $\bar{r}$ means that the variable r is a vector which would be written as (r_x, r_y, r_z) in Cartesian notation.

The inner product of two vectors is noted "$(\cdot)$", e.g., the inner product of vectors $\bar{a}$ and $\bar{b}$ will be written as "$(\bar{a} \cdot \bar{b})$". The dot "$\cdot$" is also used for multiplication by a scalar.

The model mostly follows the Monte Carlo scheme described in Hansen and Travis (1974) except for the image construction, for which we collect emerging photons in the beams of emission and azimuthal angles instead of integrating a photon distribution in the outer layer of the cloud.

A.1 Scattering

Light Source

The photons are created in the light source. The location $\bar{r}_p$ for the new point-size photon is chosen randomly according to the pre-defined spatial probability distribution. For jovian lightning, only the simple cases of the vertical line and point sources are considered. In the case of the linear source, the photons are created with homogeneous probability distribution along the line.

Although not used in this work, the model allows anisotropic sources, *i. e.*, the

direction of the new photon may be chosen according to the pre-defined phase function.

Cloud

The cloud is a cylindrical volume where the opacity is prescribed analytically by the function $\rho(\bar{r})$. Fig. A.1 shows the geometry of the photon in the cloud in the context of the global coordinate system $(\bar{e}_x, \bar{e}_y, \bar{e}_z)$. The probability of scattering for

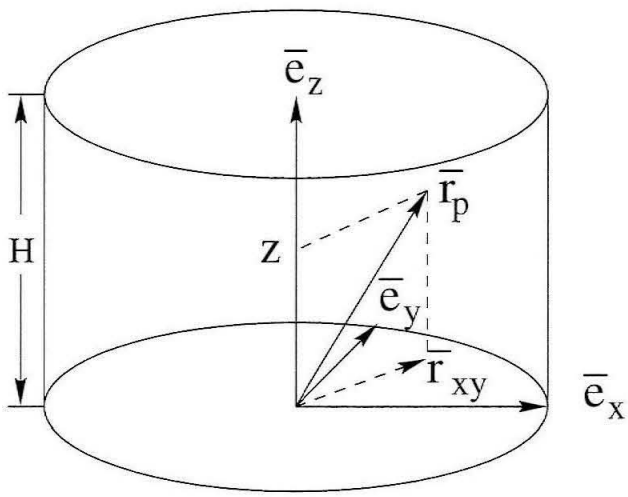

Figure A.1: Geometry of the cloud.

the photon moving from point $\bar{r}_1$ to $\bar{r}_2$ is determined by the optical depth τ, calculated from the opacity distribution ρ along the line $\bar{r}_1\bar{r}_2$.

$$\tau(\bar{r}_1, \bar{r}_2) = \int_{\bar{r}_1}^{\bar{r}_2} \rho \cdot dr$$

Some parts of the cloud volume may be clear (zero opacity), which allows to model, for example, a hemispheric cloud with clear atmosphere around or clear gaps between the cloud layers.

Photon Trajectory Calculation

The trajectory of the photon is a sequence of the linear steps between scatterings. At each step the current location $\bar{r}_p$ and speed direction (ϕ_p, θ_p) of the photon is calculated (see Fig. A.2). Scattering happens according to the scattering phase function $p(\theta)$, where θ is an angle between the old and new photon's direction and p is the probability to be scattered at the angle θ. The particular value $\theta' \in [-\pi/2, \pi/2]$ for each scattering event is calculated by numerical inversion of the integrated probability distribution.

$$P(\theta') = \int_{-\pi/2}^{\theta'} p(\theta) d\theta$$

For each scattering θ' is chosen such that the integral above is equal to the homogeneously distributed randomly generated value between 0 and 1. The approximate equality is reached by taking small steps $\delta\theta$ and approximating the integral by rectangles.

$$P(\theta') = \int_{-\pi/2}^{\theta'} p(\theta) d\theta \approx \sum_{i=0}^{n(\theta')} \frac{p(\theta_i) + p(\theta_{i+1})}{2} \delta\theta, \qquad \theta_{i+1} = \theta_i + \delta\theta$$

After θ' is chosen, the homogeneously distributed random azimuthal angle $\phi' \in [-\pi, \pi]$ is assigned to the scattered photon. Then (ϕ', θ') define a new photon's direction relative to the old photon direction (ϕ_p, θ_p) according to the scheme in Fig. A.2. The zero azimuthal direction in the local coordinate system ($\bar{e}_r$ and the perpendicular plane) is chosen such that $\phi' = 0$ assumes that for the new photon direction $\phi_p = 0$. The new photon's direction is then expressed in the global coordinate system $(\bar{e}_x, \bar{e}_y, \bar{e}_z)$.

During each step the photon travels some path $\bar{l}$ in the cloud. The path is determined by choosing the optical depth $\Delta\tau$ that the photon is going to penetrate. $\Delta\tau$ is defined randomly with the exponential probability distribution $p(\Delta\tau) = e^{-\Delta\tau}$, *i. e.*, $\Delta\tau = -ln(R)$, where R is a random number between 0 and 1. After $\Delta\tau$ is chosen,

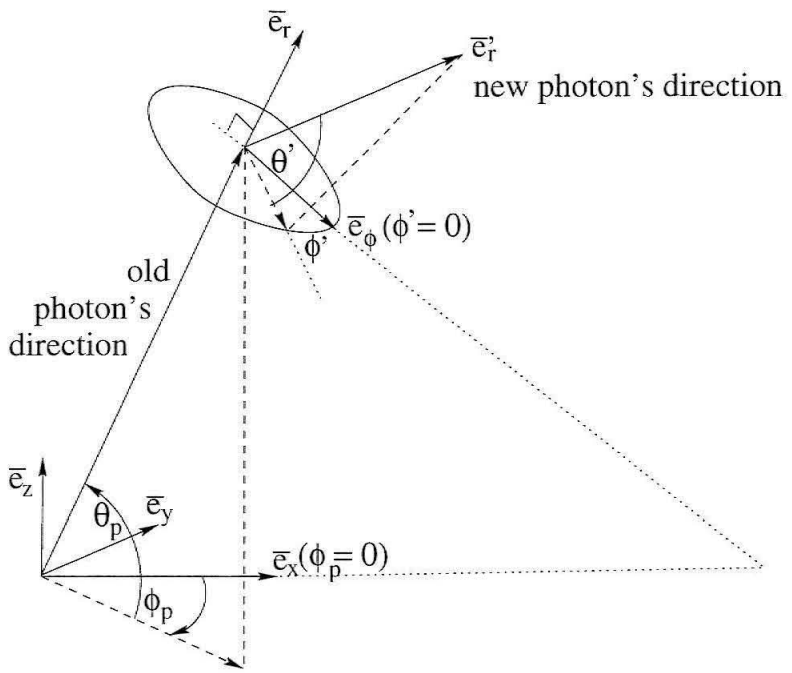

Figure A.2: Directions of the scattered photon before ($\bar{e}_r$) and after scattering ($\bar{e}'_r$). ϕ_p and θ_p are the spherical coordinates of the old photon's direction $\bar{e}_r$. ϕ' and θ' are the spherical coordinates of the new photon's direction in the local coordinate system of the photon. Direction $\bar{e}_\phi$ of zero azimuth is chosen to be in the plane of $\bar{e}_x$ and $\bar{e}_r$ (dotted continuations of $\bar{e}_x$ and $\bar{e}_\phi$ have a crossing point in the 3D space). The ellipse indicates the plane perpendicular to $\bar{e}_r$.

the $\bar{l}(\Delta\tau)$ is calculated for the current photon's position and direction.

Given $\Delta\tau$, $\bar{r}_p$ and $\bar{e}_r$, the path $\bar{l}$ is calculated by numerical integration the optical depth integral $\Delta\tau(\bar{l})$ with small variable steps δl.

$$\Delta\tau(\bar{l}) = \int_{\bar{r}_p}^{\bar{r}_p+\bar{l}} \rho(\bar{r}) \cdot d\bar{r}$$

The temporary value of the new photon location on n-th integration step is $(\bar{r}_p)^n = \bar{r}_p + \bar{l}_n$, where $\bar{l}_n = \bar{e}_r \cdot \sum_{i=0}^{n} \delta l_i$, and $\bar{e}_r$ is a unit vector along the photon's direction.

The opacity between $(\bar{r}_p)^i$ and $(\bar{r}_p)^{i+1}$ is small because of the choice of the integration step $\delta l_i = 0.01 \cdot (\rho((\bar{r}_p)^i))^{-1}$. This assumption may give an error at the edge of the cloud (sharp zero-nonzero opacity boundary). To avoid that error we define a maximum δl_i (1% of the cloud height H) that is taken instead of δl_i when δl_i defined above is too large. The integrated opacity increases every step until such n that the integral reaches $\Delta\tau$.

$$\Delta\tau_n = \sum_{i=0}^{n} \rho(\bar{r}_p^i) \cdot \delta l_i \approx \Delta\tau$$

The corresponding $\bar{l}_n$ value is taken as $\bar{l}$. If the opacity along the integration path exceeds a large pre-defined threshold value, the photon is killed, which simulates absorption by the infinitely opaque media.

If the photon remains inside the cloud after flying forward by $\bar{l}$, it is assigned by the new coordinates $\bar{r}_p + \bar{l}$ and gets scattered.

To account for absorption each photon is assigned by the intensity I_p. The new photons created in the source have a unit intensity ($I_p = 1$). During each scattering the intensity of the photon decreases by single scattering albedo $\varpi_0 \in [0, 1]$,

$$I_p(new) = \varpi_0 \cdot I_p(old).$$

In some cases of very large optical depths the very faint photons (defined by an intensity threshold) are removed from the model to reduce computations.

After leaving the cloud the photon contributes to one of the images.

A.2 Image Construction

Images are obtained by accumulating photons emerging from the cloud in different directions. The goal is to obtain the image at the particular direction. We achieve that averaging the photons flying at some range of directions. The cloud is surrounded by the simulated cameras which we call screens. Screens collect all the emerging photons in non-overlapping beams covering all possible angles. The beams are spaced at the 10° steps in ϕ and θ angles (See Fig. A.3). Accordingly, the photon's direction defines

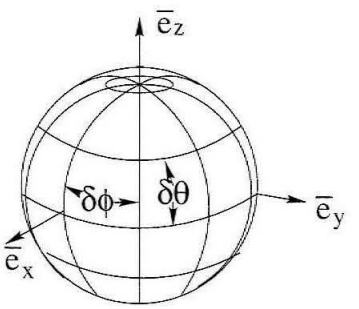

Figure A.3: Solid angle beams for different screens. Each segment collects photons for one screen. Every screen has a range of angles $\delta\phi$=10°, $\delta\theta$=10°(shown schematically with 30°-size beams).

one screen to which it contributes to.

The photon's location in the cloud defines how it is projected to the image. To track where the photon came from, every photon "remembers" the point of its last interaction with the cloud $\bar{r}_p^0$. The construction of the image of the point $\bar{r}_p^0$ for one point-size observer is illustrated in Fig. A.4. As an image plane we choose the plane

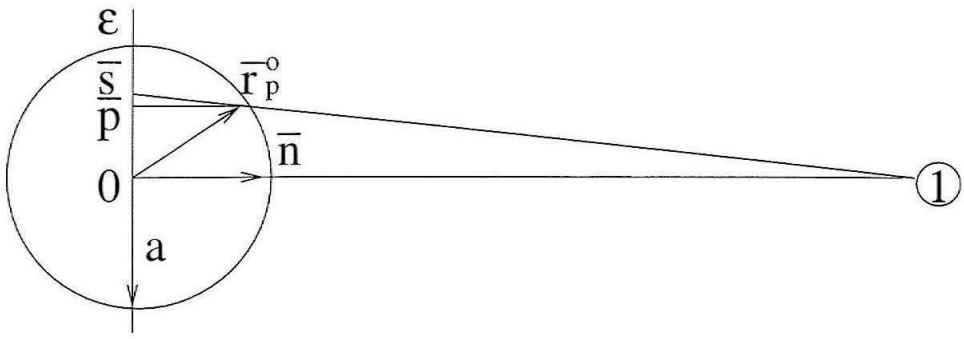

Figure A.4: Projections of point $\bar{r}_p^0$ onto the screen plane ε. The large circle indicates the cloud. The small circle on the right labeled **1** indicates an observer, **a** is a characteristic cloud size. Ray tracing image $\bar{s}$ is approximated by the perpendicular projection $\bar{p}$.

ε, which is perpendicular to the origin–observer direction. The line of sight to the point $\bar{r}_p^0$ crosses plane ε at point $\bar{s}$ which is a ray tracing image of $\bar{r}_p^0$. Point $\bar{p}$ is a perpendicular projection of $\bar{r}_p^0$ to the plane ε:

$$\bar{p} = \bar{r}_p^0 - (\bar{r}_p^0 \cdot \bar{n}) \cdot \bar{n},$$

where $\bar{n}$ is a unit vector normal to the plane ε. Instead of $\bar{s}$ we use point $\bar{p}$ as an image of $\bar{r}_p^0$. That simulates an infinitely remote observer which is a good approximation for the Galileo observations.

Each screen collects photons in the small solid angle $\delta\Omega = (\delta\phi, \delta\theta)$, where $\delta\phi = \delta\theta$=10°. All photons emerging in this range of angles are projected onto the same plane ε – the plane perpendicular to the direction origin – center of the solid angle $\delta\Omega$. Figure A.5 demonstrates an error in the projection's location when the photon emerges from the cloud at the edge of the beam. The corresponding observer is separated from the beam's center by the angle $\delta\theta/2$ (or $\delta\phi/2$). The locations of the images $\bar{p}$ are subject to the fractional error relative to cloud size a, which is smaller

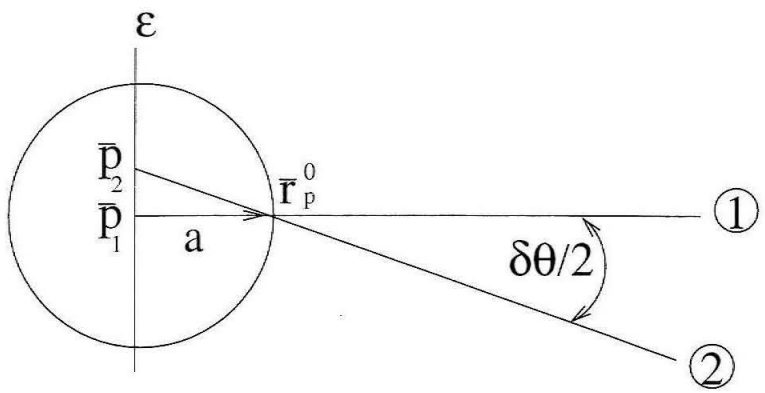

Figure A.5: Demonstration of the error due to the finite beam size. Observer 1 (circle labeled **1**) is located at the center of the screen's beam. Observer 2 (circle labeled **2**) is located at the edge of the beam and is separated from observer 1 by the angle $\delta\theta/2$. For observer 2 the image of point $\bar{r}_p^0$ appears displaced by a distance $\mid \bar{p}_1 - \bar{p}_2 \mid$.

than the following estimate.

$$\mid \bar{p}_1 - \bar{p}_2 \mid /a \approx max(tg(\delta\phi/2), tg(\delta\theta/2)) \approx 0.1$$

For each screen we choose a two-dimensional Cartesian coordinate system $((\bar{e}_x)^\varepsilon, (\bar{e}_y)^\varepsilon)$ in the screen plane ε which corresponds to the rows and columns of the screen's pixels. $(\bar{e}_x)^\varepsilon$ is usually parallel to the horizontal in the global coordinate system. The coordinates of $\bar{p}$ on the image plane ε are

$$x_\varepsilon = (\bar{p} \cdot (\bar{e_x})^\varepsilon) \quad \text{and} \quad y_\varepsilon = (\bar{p} \cdot (\bar{e_y})^\varepsilon).$$

Then $\bar{p}$ can be expressed in this system.

$$\bar{p} = x_\varepsilon \cdot (\bar{e}_x)^\varepsilon + y_\varepsilon \cdot (\bar{e}_y)^\varepsilon$$

The pixel grid is equally spaced in x_ε and y_ε.

Each photon contributes to the intensity $I_s(i,j)$ of one pixel on one screen – a square $Q(i,j)$ on the screen corresponding to the photon's direction (see Fig. A.6a). The intensity of each pixel is an accumulated intensity of the photons.

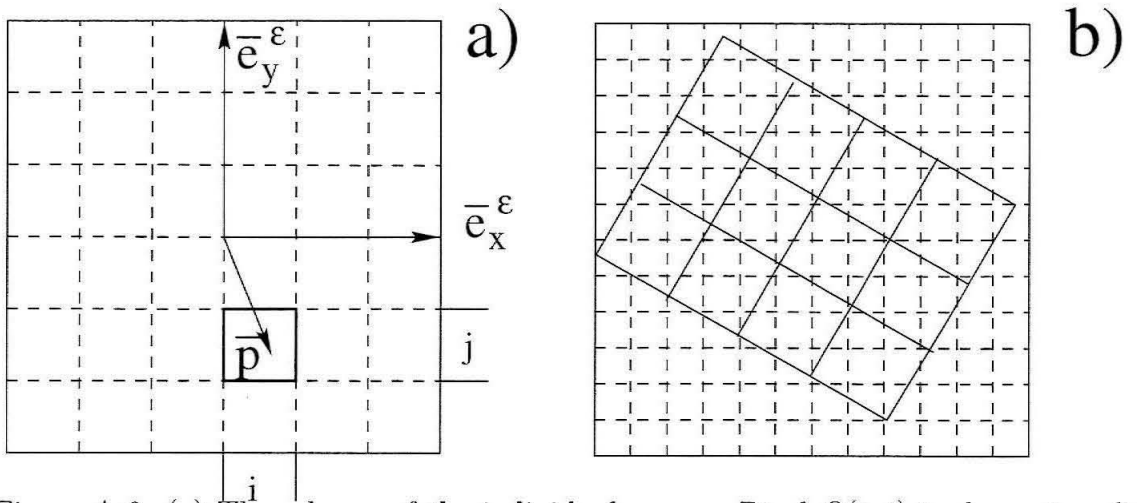

Figure A.6: (a) The scheme of the individual screen. Pixel $Q(i,j)$ is shown in solid line. (b) Scheme of resampling the modeled image (dashed lines) by the coarse grid of the data image (solid lines).

The resolution of the screens produced in the model is 100×100 pixels – 3 or more times finer than the resolution in the data. To reproduce the resolution and orientation of the data, the modeled screens are resampled. The coarse grid corresponding to the data is put on top of the fine grid as in an example shown in Fig. A.6 b. The value of each pixel of the coarse grid is the sum of intensities of the fine grid pixels within it.

Different locations of the coarse grid are tested. The brightness falloff plots for jovian lightning show all the points from the brightness falloffs for the ensemble of the coarse grid locations. The ensemble corresponds to the grid of shifts by 0.2, 0.4., 0.6, and 0.8 of the coarse pixel in both column and line directions.

A.3 Computer Implementation

A.3.1 Algorithm

The code is written in C++ and is object-oriented. Figure A.7 shows the scheme of the objects.

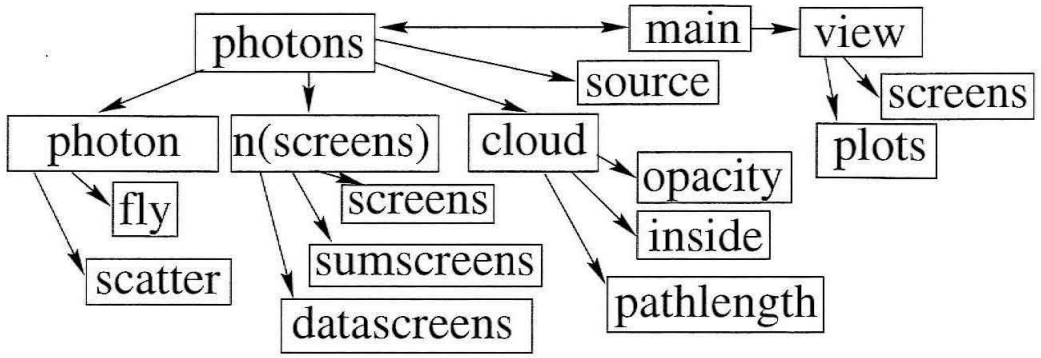

Figure A.7: Scheme of the program.

The main class called "photons" contains the current photon, a vector of "screens" objects, "cloud" class and "source" class. The main program starts scattering calculations and the user interface (class "view"). Scattering calculations and the user interface are organized as separate threads and run parallel. The updated images can be output while the scattering code is running.

The "photon" object has methods "fly" and "scatter" called sequentially until the photon leaves the cloud or is killed due to some of the thresholds. There are 3 types of screen containers. **Screens** – container of the screens counting photons which are described in Section A.2. **Sumscreens** – container of longitudinally averaged screens (one per each emission angle). Sumscreens are updated by the user interface request. **Datascreens** – container of screens read from the data files.

"Cloud" object is responsible for calculations of $\bar{l}$ ("pathlength" method), which

is called from the "Photon::fly" method. Method "inside" indicates when the photon leaves the cloud.

The current state of the calculations can be written to a file and restored later to continue the run.

A.3.2 Performance

The model was running on a PC with a Pentium II 450 MHz processor. Because the computational cost depends very strongly on the opacity distribution in the cloud and (to a lesser extent) on the desired output image quality, the examples below intend to give a very approximate estimate of the computational performance of the model.

The modeled images were initially collected on 100×100 pixel grid. The image size relative to the flash size is approximately the same as in the jovian lightning images (Figs. 3.2 and 3.3). The beam size collecting photons for each image is 10°. All images at different azimuths (36 angles) are averaged to produce an image at each of the 18 emission angles (9 angles out of Jupiter and 9 angles into Jupiter). An example of a 100×100 image is shown in Fig. A.8. Because the brightness in the image is stretched to bring up faint pixels, we also show the actual pixel values $I_s(i,j)$ for the middle row of pixels in Fig. A.9. The quality of the image is considered acceptable when the noise/(maximum brightness) is about 0.2-0.5 in the 100×100 image and the resulting coarser resolution image look smooth. In the coarse grid images the pixel values are usually averaged in 3×3 or larger boxes, which increases precision. Because of the large optical depth of 50, most of the photons are scattered many times, which decreases the photon's intensity at each scattering. As a consequence, each photon contributing to the pixels in Fig.A.9 is substantially fainter than unity (which is its initial intensity). That can be seen at the tails of the distribution in Fig.A.9, where pixels likely collected only one photon and the corresponding pixel value represents

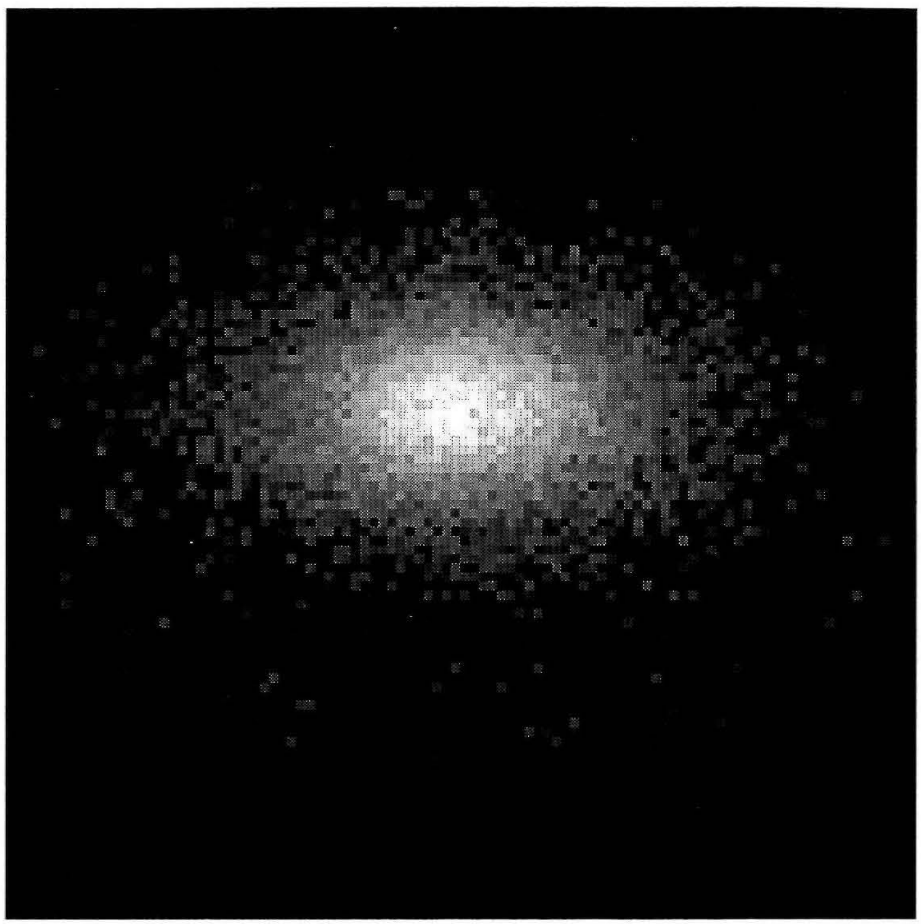

Figure A.8: Sample 100×100 image. The longitudinally-averaged image obtained at emission angle 55°for the plane-parallel cloud of τ=50 with the standard Henyey-Greenstein phase function (g_1=0.8, g_2=-0.75, f=0.954) and single scattering albedo of 0.996. The point lightning is at the bottom of the cloud. The total number of photons in this run is 2.6×10^6. The brightness is stretched logarithmically to bring up faint pixels.

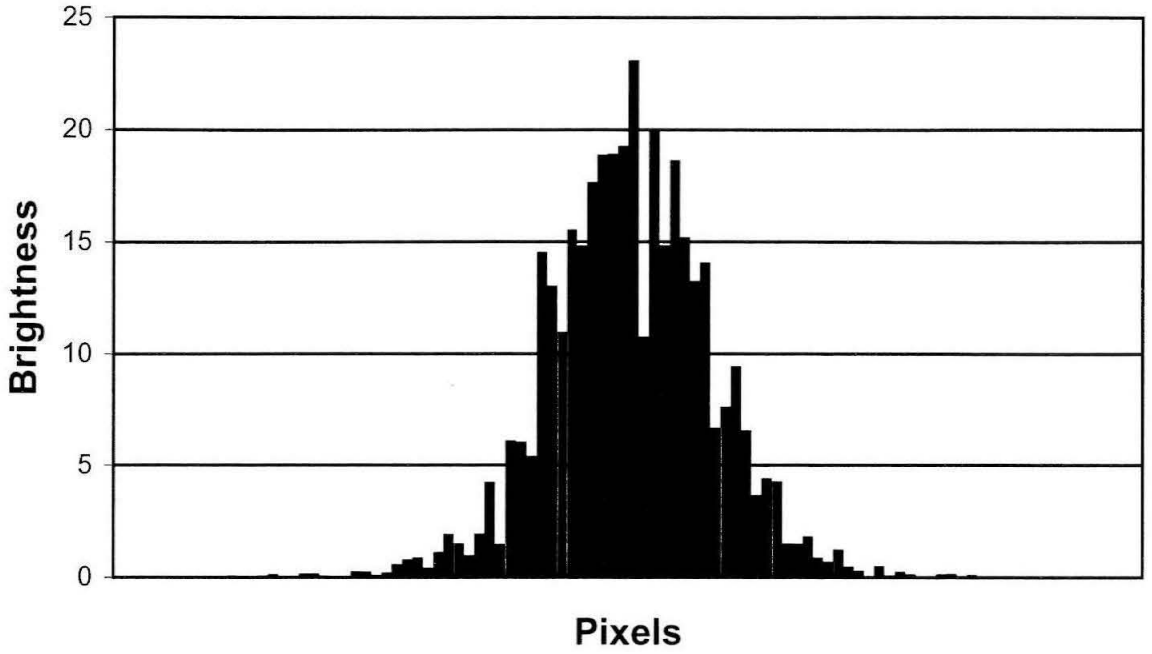

Figure A.9: Pixel values for the row of pixels across the brightest part of the image in Fig. A.8.

the intensity of a single photon. Note that at single scattering albedo 0.996 many scatterings are needed to decrease the photon intensity, *e. g.*, to decrease the intensity by 10%, the photon must scatter 25 times.

The computational time needed to produce such images varies from few minutes and $10^5 - 10^6$ photons for the clouds of optical depths of 5–10 to tens of hours and $10^6 - 10^8$ photons for the clouds of optical depths 100. Note that at large optical depths each photon requires much more computations because of a large number of scatterings.

The most time consuming calculation is to compute the photon's path length at each step. This pays for the flexible and rather accurate description of the variable 3D opacity.

A.4 Advantages and Disadvantages of Monte Carlo Approach

Advantages

Another approach to 3D light scattering is a direct calculation of light distribution in the cloud and a construction of ray tracing images. Light distribution for the arbitrary cloud can only be calculated numerically using a 3D finite grid. Monte Carlo model does not need a grid and does not have related errors.

Also Monte Carlo model requires less memory because calculations of a light distribution for multiple scattering require multiple integration over a large 3D grid and each order of integration needs a cross-referencing between the grid cells as secondary light sources.

The accuracy of the Monte Carlo images increases with time due to photon accu-

mulation. It is good for both preliminary and long accurate calculations.

Disadvantages

One of the disadvantages of the Monte Carlo method is a limited accuracy in direction. The solid angle $\delta\Omega$ should be relatively large to collect enough photons. That generates the errors described in Section A.2.

Although Monte Carlo is the most effective method for the arbitrary 3D cloud, there are methods which are faster for restricted problems, *i. e.*, 2D or plane-parallel cases, or the case of single scattering.

A.5 Tests

The model was tested against analytically derived results of Chandrasekhar (1960), results of Van De Hulst (1980), and the results of a simpler Monte Carlo model which was written independently for the preliminary study of the Galileo flashes (Little et al., 1999). Figure A.10 shows the comparison for the law of diffuse reflection and transmission by plane-parallel atmospheres of finite optical thickness and under conditions of isotropic scattering with an albedo ϖ=0.9 (Fig. 22 of Chandrasekhar (1960)). According to the notation of Chandrasekhar (1960), μ_0 is a cosine of the incidence angle, F is the flux per unit area that would be reflected by a Lambertian surface, optical thickness τ_1 is equivalent to τ in our notation, and X- and Y-functions are constructions used to obtain analytical solution for the radiative transfer equation. The error bars in our results and results of the preliminary Monte Carlo model are about the symbol size except for larger errors in our model at emission angles near 0°and 90°. The errors at 0° are due to the worse photons' statistics in the smaller bin. The errors at 90° are due to the effects of finite cloud size. The results are in good agreement with the curves except near 0° and 90°. Note that the preliminary Monte Carlo model is written independently, assumes infinite plane-parallel cloud instead of

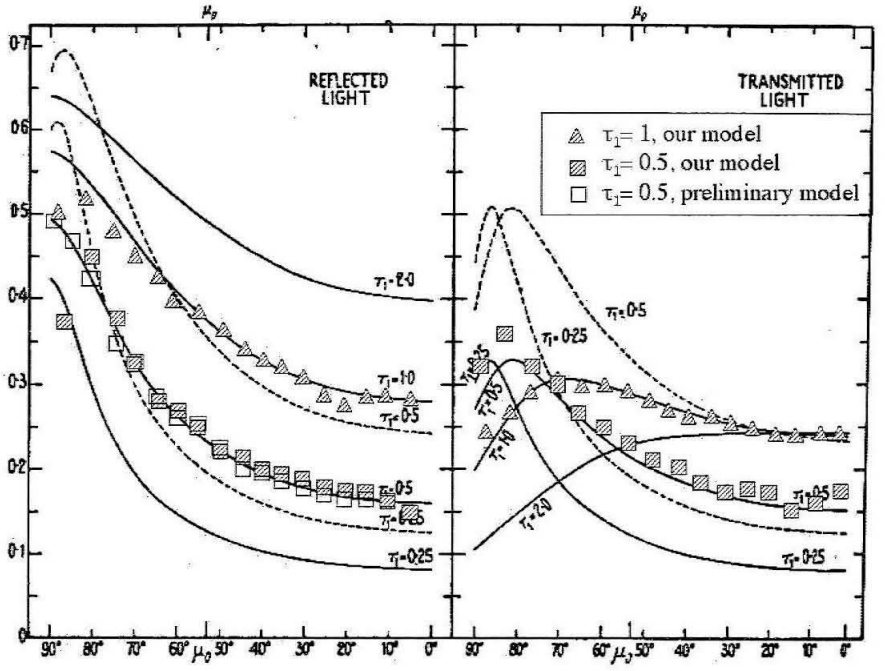

Figure A.10: Comparison of our results with Fig. 22 of Chandrasekhar (1960). The hatched symbols show our results, the open symbols show the results of the preliminary model used in (Little et al., 1999).
Chandrasekhar (1960) describes the curves as follows:
The law of diffuse reflection and transmission by plane-parallel atmospheres of finite optical thicknesses and under conditions of isotropic scattering with albedo ϖ=0.9.
The ordinates represent the intensity in the unit $\mu_0 F$ and the abscissae the angle in degrees (0°means straight up, 90°means parallel to the cloud).
An angle of incidence corresponding to μ_0=0.6 is considered and the angular distribution of the reflected light (the curves on the left side of the diagram) and the transmitted light (the curves on the right side of the diagram) are illustrated for various values of the optical thickness τ_1.
The full-line curves have been derived from the rational approximations of the X- and Y-functions; and the dashed curves have been obtained from the solution developed for small values of τ_1.

a finite-sized cylinder used in our model and collects photons directly in the emission angle bins instead of producing images.

To validate the non-isotropic scattering according to the Henyey-Greenstein phase function, we compared the diffuse reflection curves with the results of the preliminary Monte Carlo model. Several combinations of Henyey-Greenstein parameters and several optical depths were tested and gave an agreement within the error bars.

To validate the azimuthal resolution, we simulated the law of diffuse scattering by a semi-infinite atmosphere on Rayleigh scattering in directions along and perpendicular to the line of sight (Fig. 24 of Chandrasekhar (1960)). The semi-infinite atmosphere was approximated by the cloud of optical depth 100. The intensity versus emission angle dependences agree within 5-10%.

Bibliography

Bagenal, F., editor (2001). *Jupiter - The Planet, Satellites and Magnetosphere.* Oxford University Press.

Baines, K. H., Carlson, R. W., Camp, L. W., and Team, G. (1999). Jupiter's major anti-cyclonic systems: a Galileo/NIMS perspective. *Bull.–Am. Astron. Soc.*, 31(4):1174. [Abstract].

Banfield, D., Gierasch, P. J., Bell, M., Ustinov, E., Ingersoll, A. P., Vasavada, A. R., West, R. A., and Belton, M. J. S. (1998). Jupiter's cloud structure from Galileo imaging data. *Icarus*, 135:230–250.

Bar-Nun, A. and Podolak, M. (1985). The contribution by thunderstorms to the abundance of CO, C_2H_2, and HCN on Jupiter. *Icarus*, 64:112–124.

Beebe, R. (1997). *Jupiter, the Giant Planet.* Smithsonian Institution Press, Washington, London.

Belton, M. J. S., Head, J. W., Ingersoll, A. P., Greeley, R., McEwen, A. S., Klaasen, K. P., Senske, D., Pappalardo, R., Collins, G., Vasavada, A. R., Sullivan, R., Simonelli, D., Geissler, P., Carr, M. H., Davies, M. E., Veverka, J., Gierasch, P. J., Banfield, D., Bell, M., Chapman, C. R., Anger, C., Greenberg, R., Neukum, G., Pilcher, C. B., Beebe, R. F., Burns, J. A., Fanale, F., Ip, W., Johnson, T. V., Morrison, D., Moore, J., Orton, G. S., Thomas, P., and West, R. A. (1996). Galileo's first images of Jupiter and the Galilean satellites. *Science*, 274:377–384.

Boccippio, D. J., Goodman, S. J., and Heckman, S. (2000). Regional differences in tropical lightning distribution. *J. Appl. Meteorol.*, 39:2231–2248.

Borucki, W. J., Bar-Nun, A., Scarf, F. L., Cook, A. F., and Hunt, G. E. (1982). Lightning activity on Jupiter. *Icarus*, 52:492–502.

Borucki, W. J. and Magalhães, J. A. (1992). Analysis of Voyager 2 images of jovian lightning. *Icarus*, 96:1–14.

Borucki, W. J., McKay, C. P., Jebens, D., Lakkapaju, H. S., and Vanajakshi, C. T. (1996). Spectral irradiance measurements of simulated lightning in planetary atmospheres. *Icarus*, 123:336–344.

Borucki, W. J. and Williams, M. A. (1986). Lightning in the jovian water cloud. *J. Jeophys. Res.*, 91:9893–9903.

Carlson, B. E., Lacis, A. A., and Rossow, W. B. (1994). Belt-zone variations in the Jovian cloud structure. *J. Geophys. Res.*, 99(E7):14623–14658.

Carlson, R., Smythe, W., Baines, K., Barbinis, E., Becker, K., Burns, R., Calcutt, S., Calvin, W., Clark, R., Danielson, G., Davies, A., Drossart, P., Encrenaz, T., Fanale, F., Granahan, J., Hansen, G., Herrera, P., Hibbitts, C., Hui, J., Irwin, P., Johnson, T., Kamp, L., Kieffer, H., Leader, F., Lellouch, E., LopesGautier, R., Matson, D., McCord, T., Mehlman, R., Ocampo, A., Orton, G., Roos-Serote, M., Segura, M., Shirley, J., Soderblom, L., Stevenson, A., Taylor, F., Torson, J., Weir, A., and Weissman, P. (1996). Near-infrared spectroscopy and spectral mapping of Jupiter and Galilean Satellites: Results from Galileo's initial orbit. *Science*, 274:385–388.

Chandrasekhar, S. (1960). *Radiative Transfer*. Dover Publications, Inc.

Christian, H. G. K., Blakeslee, R. J., Goodman, S. J., and Mach, D. M. (2000). *Algorithm Theoretical Basis Documant (ATBD) for the Lightning Imaging Sensor (LIS)*. NASA. Available online at http://eospso.gsfc.nasa.gov/atbd/listables.html.

Cook, A. F., Duxbury, T. C., and Hunt, G. E. (1979). First results on jovian lightning. *Nature*, 280:794.

Del Genio, A. D. and McGrattan, K. B. (1990). Moist convection and the vertical structure and water abundance of Jupiter's atmosphere. *Icarus*, 84:29–53.

Dyudina, U. A. and Ingersoll, A. P. (2001). Monte Carlo radiative transfer modeling of lightning observed in Galileo images of Jupiter. Submitted to *Icarus*.

Dyudina, U. A., Ingersoll, A. P., Danielson, G. E., Baines, K. H., Carlson, R. W., and the Galileo NIMS and SSI teams (2001). Interpretation of NIMS and SSI images on the jovian cloud structure. *Icarus*, 150:219–233.

Gierasch, P. J., Ingersoll, A. P., Banfield, D., Ewald, S. P., Helfenstein, P., Simon-Miller, A., Vasavada, A., Breneman, H. H., Senske, D. A., and the Galileo Imaging Team (2000). Observation of moist convection in Jupiter's atmosphere. *Nature*, 403:628–630.

Goody, R. M. and Yung, Y. L. (1989). *Atmospheric Radiation*. Oxford University Press, New York, Oxford.

Hansen, J. E. and Travis, L. D. (1974). Light scattering in planetary atmospheres. *Space Sci.Rev.*, 16:527–610.

Hueso, R. and Sánches-Lavega, A. (2001). A three-dimensional model of moist convection for the giant planets: the Jupiter case. *Icarus.*, 151:257–274.

Ingersoll, A. P. (1976). The atmosphere of Jupiter. *Space Sci. Rev.*, 18:603–639.

Ingersoll, A. P., Gierasch, P. J., Banfield, D., Vasavada, A. R., and the Galileo Imaging Team (2000). Moist convection as an energy source for the large-scale motions in Jupiter's atmosphere. *Nature*, 403:630–632.

Ingersoll, A. P., Münch, G., Neubauer, G., and Orton, G. S. (1976). Results of the infrared radiometer experiment on Pioneer 10 and 11. In Gehrels, T., editor, *Jupiter*, pages 197–205. Univ. of Arizona Press, Tucson.

Irwin, P. G. J. and Dyudina, U. A. (2001). The retrieval of cloud structure maps in the Equatorial region on Jupiter using a Principal Component Analysis of Galileo/NIMS data. *Icarus*, in press.

Irwin, P. G. J., Weir, A. L., Smith, S. E., Taylor, F. W., Lambert, A. L., Calcutt, S. B., Cameron-Smith, P. J., Carlson, R. W., Baines, K., Orton, G. S., Drossart, P., Encrenaz, T., and Roos-Serote, M. (1998). Cloud structure and atmospheric composition of Jupiter retrieved from Galileo near-infrared mapping spectrometer real-time spectra. *J. Geophys. Res.*, 103:23001–23021.

Irwin, P. G. J., Weir, A. L., Taylor, F. W., Calcutt, S. B., and Carlson, R. W. (2001). The origin of belt/zone contrasts in the atmosphere of Jupiter and their correlation with 5-micron opacity. *Icarus.*, 149:397–415.

Karkoschka, E. (1994). Spectroscopy of the jovian planets and Titan at 300- to 1000-nm wavelength: The methane spectrum. *Icarus*, 111:174–192.

Klaasen, K. P., Belton, M. J. S., Breneman, H. H., McEven, A. S., Davies, M. E., Sullivan, R. J., Chapman, C. R., Neukum, G., Heffernan, C. M., Harch, A. P., Kaufman, J. M., Merline, W. J., Gaddis, L. R., Cunningham, W. F., Helfenstein, P., and Colvin, T. R. (1997). Inflight performance characteristics, calibration, and utilization of the Galileo solid-state imaging camera. *Opt. Eng.*, 36:3001–3027.

Koshak, W. J., Solakewicz, R. J., Phanord, D. D., and Blakeslee, R. J. (1994). Diffusion model for lightning radiative transfer. *J. Geophys. Res.*, 99:14361–14371.

Lewis, J. S. (1969a). The clouds on Jupter and the NH_3-H_2O and NH_3-H_2S systems. *Icarus*, 10:365–378.

Lewis, J. S. (1969b). Observability of spectroscopically active compounds in the atmosphere of Jupiter. *Icarus*, 10:393–409.

Little, B., Anger, C. D., Ingersoll, A., Vasavada, A. R., Senske, D. A., Breneman, H. H., Borucki, W. J., and the Galileo SSI Team (1999). Galileo images of lightning on Jupiter. *Icarus*, 142:306–323.

Magalhães, J. A. and Borucki, W. J. (1991). Spatial distribution of visible lightning on Jupiter. *Nature*, 349:311–313.

Murtagh, F. and Heck, A. (1987). *Multivariate Data Analysis*. D. Reidel Publishing Company, Dordrecht/ Boston/ Lancaster/ Tokyo.

Niemann, H. B., Atreya, S. K., Cargnan, G. R., Donahue, T. M., Haberman, J. A., Harpold, D. N., Hartle, R. E., Hunten, D. M., Kasprzak, W. T., Mahaffy, P. R., Owen, T. C., Spencer, N. M., and Way, S. H. (1996). The Galileo probe mass spectrometer: Composition of Jupiter's atmosphere. *Science*, 272:846–849.

Niemann, H. B., Atreya, S. K., Cargnan, G. R., Donahue, T. M., Haberman, J. A., Harpold, D. N., Hartle, R. E., Hunten, D. M., Kasprzak, W. T., Mahaffy, P. R., Owen, T. C., Spencer, N. M., and Way, S. H. (1998). The composition of the Jovian atmosphere as determined by the Galileo probe mass spectrometer. *J. Geophys. Res.*, 103(E10):22831–22845.

Orton, G. S., Fisher, B. M., Baines, K. H., Stewart, S. T., Friedson, A. J., Ortiz, J. L., Marinova, M., Ressler, M., Dayal, A., Hoffmann, W., Hora, J., Hinkley,

S., Krishnan, V., Masanovic, M., Tesic, J., Tziolas, A., and Parija, K. C. (1998). Characteristics of the Galileo probe entry site from Earth-based remote sensing observations. *J. Geophys. Res.*, 103:22791–22814.

Porco, C. and the Cassini ISS team (2001). Results of Cassini ISS camera observations. In preparation (see also the Cassini movies at http://ciclops.lpl.arizona.edu/ciclops/images_jupiter.html).

Ragent, B., Colburn, D. S., Rages, K. A., Knight, T. C. D., Avrin, P., Orton, G., Yanamandra-Fisher, P. A., and Grams, G. W. (1998). The clouds on Jupiter: results of the Galileo Jupiter mission probe nephelometer experiment. *J. Geophys. Res.*, 103:22891–22909.

Rakov, V. A. and Uman, M. A. (2001). *Lightning: Physics and Effects (Encyclopedia of Lightning)*. Cambridge University Press. In preparation.

Rinnert, K., Lanzerotti, L. J., Uman, M. A., Dehmel, G., Gliem, F. O., Krider, E. P., and Bach, J. (1998). Measurements of radio frequency signals from lightning in Jupiter's atmosphere. *J. Geophys. Res.*, 103:22979–22992.

Roos-Serote, M., Drossart, P., Encrenaz, T., Lellouch, E., Carlson, R. W., Baines, K. H., Camp, L., Mehlman, R., Orton, G. S., Calcutt, S. B., Irwin, P., Taylor, F. W., and Weir, A. L. (1998). Analysis of Jupiter North Equatorial belt hot spots in the 4-5 μm range from Galileo/near-infrared mapping spectrometer observations: Measurements of cloud opacity, water, and ammonia. *J. Geophys. Res.*, 103:23023–23041.

Roos-Serote, M., Vasavada, A. R., Camp, L., Drossart, P., Irwin, P., Nixon, C., and Carlson, R. W. (2000). Proximate humid and dry regions in Jupiter's atmosphere indicate complex local meteorology. *Nature*, 405:158–160.

Rossow, W. B. (1978). Cloud microphysics: Analysis of the clouds on Earth, Venus, Mars, and Jupiter. *Icarus*, 36:1–50.

Sada, V. S., Beebe, R. F., and Conrath, B. J. (1996). Comparison of the structure and dynamics of Jupiter's Great Red Spot between the Voyager 1 and 2 encounters. *Icarus*, 119:311–335.

Satoh, T. and Kawabata, K. (1994). A change of upper cloud structure in Jupiter's south equatorial belt during the 1989-1990 event. *J. Geophys. Res.*, 99:8425–8440.

Scarf, F. L., Gurnett, D. A., and Kurt, W. S. (1979). Jupiter plasma wave observations: Voyager 1 overview. *Science*, 204:991–995.

Seiff, A., Kirk, D. B., Knight, T. C. D., Young, R. E., Mihalov, J. D., Young, L. A., Milos, F. S., Shubert, G., Blanchard, R. C., and Atkinson, D. (1998). Thermal structure of Jupiter's atmosphere near the edge of a 5μm hot spot in the north equatorial belt. *J. Geophys. Res.*, 103:22857–22889.

Simon-Miller, A. A., Conrath, B. J., Gierasch, P. J., and Beebe, R. F. (2000). A detection of water ice on Jupiter with Voyager IRIS. *Icarus*, 145:454–461.

Smith, B. A., Soderblom, L. A., Johnson, T. V., Ingersoll, A. P., Collins, S. A., Shoemaker, E. M., Hunt, G. E., Masursky, H., Carr, M. C., Davies, M. E., Cook, A. F., Boyce, J., Danielson, G. E., Owen, T., Sagan, C., Beebe, R. F., Veverka, J., Storm, R. G., McCauley, J. F., Morrison, D., Briggs, G. A., and Suomi, V. E. (1979). The Jupiter system through the eyes of Voyager 1. *Science*, 204:951–972.

Sromovsky, L. A. and Fry, P. M. (2001). Jupiter's cloud structure as constrained by Galileo probe and HST observations. Submitted to Icarus.

Thomason, L. W. and Krider, E. P. (1982). The effects of clouds on the light produced by lightning. *J. Atmos. Sci.*, 39:2051–2065.

Tomasko, M. G., West, R. A., and Castillo, N. D. (1978). Photometry and polarimetry of Jupiter at large phase angles. I. Analysis of imaging data of a prominent belt and a zone from Pioneer 10. *Icarus*, 33:558–592.

Uman, M. A. (1987). *The Lightning Discharge.* Academic Press, New York.

Van De Hulst, H. C. (1980). *Multiple Light Scattering. Tables, Formulas, and Applications.* Academic Press, New York/ London/ Toronto/ Sydney/ San Francisco.

Vasavada, A. R., Ingersoll, A. P., Banfield, D., Bell, M., Gierasch, P. J., Belton, M. J. S., Orton, G. S., Klaasen, K. P., DeJong, E., Breneman, H. H., Jones, T. J., Kaufman, J. M., Magee, K. P., and Senske, D. A. (1998). Galileo imaging of Jupiter's atmosphere: the Great Red Spot, equatorial region, and White Ovals. *Icarus*, 135:265–275.

Weidenschilling, S. J. and Lewis, J. S. (1973). Atmospheric and cloud structures of the jovian planets. *Icarus*, 20:465–476.

Weir, A. L., Irwin, P. G. J., Smith, S., Taylor, F. W., Lambert, A., Smith, P. J., Carlson, R., Baines, K., Encrenaz, T., Drossart, P., and Ross-Serote, M. (1997). Jovian atmospheric structure as revealed by Galileo/NIMS. *Bull.–Am. Astron. Soc.*, 29(3):1005. [Abstract].

West, R. A., Strobel, D. F., and Tomasko, M. G. (1986). Clouds, aerosols, and photochemistry of jovian atmosphere. *Icarus*, 65:161–217.

Williams, M. A., Krider, E. P., and Hunten, D. M. (1983). Planetary lightning: Earth, Jupiter, and Venus. *Rev. Geoph. and Space Phys.*, 21(4):892–902.